

On the Modelling of Hyperspectral Light and Skin Interactions and the Simulation of Skin Appearance Changes Due to Tanning

by

Tenn Francis Chen

A thesis
presented to the University of Waterloo
in fulfillment of the
thesis requirement for the degree of
Doctor of Philosophy
in
Computer Science

Waterloo, Ontario, Canada, 2015

© Tenn Francis Chen 2015

Author's Declaration

I hereby declare that I am the sole author of this thesis. This is a true copy of the thesis, including any required final revisions, as accepted by my examiners.

I understand that my thesis may be made electronically available to the public.

Abstract

The distinctive visual attributes of human skin are largely determined by its interactions with light across different spectral domains. Accordingly, the modelling of these interactions has been the object of extensive investigations in numerous fields for a diverse range of applications. However, only a relatively small portion of these research efforts has been directed toward the comprehensive simulation of hyperspectral light and skin interactions, as well as the associated temporal changes in skin appearance, which can be caused by a myriad of time-dependent photobiological phenomena.

In this thesis, we explore this area of research. Initially, we present the first hyperspectral model designed for the predictive rendering of skin appearance attributes in the ultraviolet, visible and infrared domains. We then describe a novel physiologically-based framework for the simulation and visualization of skin tanning dynamics, arguably the most prominent and persistent of such relevant time-dependent phenomena.

The proposed model incorporates the intrinsic bio-optical properties of human skin affecting hyperspectral light transport, including the particle nature and distribution patterns of the main light attenuation agents found within the cutaneous tissues. Accordingly, it accounts for phenomena that significantly affect skin spectral signatures within and outside the visible domain, such as detour and sieve effects, which are overlooked by existing skin appearance models. Using a first principles approach, this model computes the surface and subsurface scattering components of skin reflectance taking into account not only the wavelength and the illumination geometry, but also the positional dependence of the reflected light. Hence, the spectral and spatial distributions of light interacting with human skin can be comprehensively represented in terms of hyperspectral reflectance and scattering distribution functions respectively.

The proposed tanning simulation framework incorporates algorithms that explicitly account for the connections between spectrally-dependent light stimuli and time-dependent physiological changes occurring within the cutaneous tissues. For example, it utilizes the above hyperspectral model as a modular component to evaluate the wavelength-dependence of the tanning phenomenon. This enables the effective simulation of the skin's main adaptive mechanisms to ultraviolet radiation as well as its responses to distinct light exposure regimes. We demonstrate the predictive capabilities of this framework through quantitative and qualitative comparisons of simulated data with measurements and experimental observations reported in the scientific literature. We also provide image sequences depicting skin appearance changes elicited by time-dependent variations in skin biophysical parameters.

The work presented in this thesis is expected to contribute to advances in realistic image synthesis by increasing the spectral and temporal domains of material appearance modelling,

and to provide a testbed for interdisciplinary investigations involving the visualization of skin responses to photoinduced processes.

Acknowledgements

First and foremost, I have to thank my parents for their unsung sacrifices, unconditional support and boundless love. You have continuously provided me with a constructive environment for me to develop my character over the years. You are the best parents in the world.

I would like to sincerely thank my supervisor, Professor Gladimir V. G. Baranoski, for imparting his precious time, expertise and wisdom. You have given me opportunities, confidence and encouragement to knock down brick walls. Many thanks as well to my peers from the Natural Phenomena Simulation Group for assisting with the technical infrastructure and knowledge to build battering rams.

I would also like to thank the members of my PhD committee, Professors Pierre Poulin, Ricardo Fukasawa, Jeff Orchard, and Chrysanne DiMarco, for their valuable time despite their full schedules. Your fresh perspectives and discerning insights helped me improve the quality of my doctoral work.

I thank my fellow graduate students for partaking in this arduous journey with me. Sharing the joys and sufferings with you renews the spirit and allows me to march on. I hope I have afforded you the same courtesy.

I would like to thank my church family and the numerous fellowships for sharing, caring and learning together.

To all my friends, I thank you for being the spice of life.

Dedication

To God, who provides solid rock to build upon, and makes everything possible.

Table of Contents

Author's Declaration	ii
Abstract	iii
Acknowledgements	v
Dedication	vi
List of Figures	xi
List of Tables	xxiv
List of Acronyms	xxvi
List of Symbols	xxviii
1 Introduction	1
1.1 Research Motivation	2
1.2 Summary of Original Contributions	4
1.3 Document Organization	6
2 Related Work	10
2.1 Measurement of Appearance Concepts	10

2.1.1	Spectral Distribution	11
2.1.2	Spatial Distribution	12
2.2	Modelling of Skin Appearance	13
2.3	Modelling of Material Appearance Changes	14
3	Skin Biophysical Background	16
3.1	Light Absorbing Materials	17
3.2	Light Scattering Materials	17
3.3	Detour and Sieve Effects	18
3.4	Skin Photobiological Phenomena	19
4	HyLIoS Model Description	22
4.1	Absorbers	25
4.2	Attenuators	26
4.2.1	Melanosomes and Melanosome Complexes	26
4.2.2	Connective Fibres	29
4.3	Large Scale Cellular Structures	30
5	Tanning Simulation Framework Description	31
5.1	Melanin Dynamics	31
5.1.1	UVR Dose Evaluation	33
5.1.2	Melanin Production and Removal	35
5.2	Thickness Dynamics	37
5.2.1	UVR Dose Evaluation	37
5.2.2	Thickness Regulation	38
5.3	Framework Output	40

6	Evaluation Methodology	42
6.1	Evaluating the HyLloS Model	42
6.1.1	Skin Characterization Data	42
6.1.2	Quantitative and Qualitative Comparisons	45
6.1.3	Input Sensitivity Analysis	52
6.1.4	Usability and Performance Issues	59
6.2	Evaluating the Tanning Simulation Framework	59
6.2.1	Tanning Dynamics Specification Data	59
6.2.2	Quantitative and Qualitative Comparisons	60
6.2.3	Usability and Performance Issues	66
7	Conclusion	68
7.1	Contributions to Computer Graphics Research	69
7.2	Contributions to Interdisciplinary Research	70
7.3	Future Research	71
	References	73
	APPENDICES	92
A	Supplementary Biophysical Data	93
B	Deriving Tanning Specification Data	96
C	Melanosome Distribution Patterns Affecting Skin Reflectance	98
C.1	Methods and Data	99
C.2	Findings and Discussion	100
C.3	Concluding Remarks	103

D	Effective Compression and Reconstruction of Human Skin Hyperspectral Reflectance Databases	104
D.1	Methods and Data	105
D.2	Findings and Discussion	107
D.3	Concluding Remarks	111
E	Hyperspectral Photography	112
E.1	Hardware Description	112
E.2	Practical Considerations	113
E.3	Images	114
E.4	Concluding Remarks	122
	Index	123

List of Figures

1.1	Photographs of a women taken in the different spectral domains. From left to right: UV, visible and IR. Note the intensification of pigmentation irregularities (employed in appearance-based cancer prevention initiatives [63, 115]) and more specular appearance in the UV range, as well as the more diffuse, “ethereal” skin appearance that can be obtained in the IR domain (employed in artistic applications [167]). The UV and IR photos are depicted using pseudo colour. Technical details regarding how these photographs were acquired are presented in Appendix E.	3
2.1	Diagram illustrating spectral (left) and spatial (right) distributions of propagated light. On the left, the light represented by the solid red, dashed green and dotted blue lines are reflected, absorbed and transmitted, respectively. On the right, the spatial distribution for the reflected light is more directionally oriented (specular) and more diffusely oriented for the transmitted light.	11
2.2	Diagram illustrating the difference between a BSSRDF (left) and the corresponding BRDF (right).	12
2.3	Photograph series showing changes in pigmentation over time as a result of a controlled tanning experiment using distinct UVR exposure doses [122]. Left: initial state. Centre: emerging responses. Right: peak responses. The three patches of darkened skin correspond to different exposure doses, and the fourth patch (on the lower right of centre and right images) represents the unexposed control area. Note that areas on the left side of the back (leftmost photo) show results from previous experiments on skin sensitivity to UVR exposure. Courtesy of S. Miller [122]. Original image copyright by John Wiley & Sons, Inc.	15

3.1	Sketches depicting the distribution of melanosomes within the epidermal layers of skin specimens with different levels of melanin pigmentation. Left: melanosome complexes found in lightly pigmented specimens. Centre: more compact complexes found in moderately pigmented specimens. Right: individually dispersed melanosomes found in darkly pigmented specimens.	18
3.2	Diagram illustrating detour (left) and sieve (right) effects that may take place when light traverses an epidermal layer containing melanosome complexes. The same phenomena may take place in a layer occupied by individually dispersed melanosomes.	19
3.3	Sketches illustrating the distribution of melanin originally produced in the innermost epidermal layers. Left: initially the melanin encapsulated in the melanosomes is predominantly located within these layers. Right: as the epidermal cells migrate upwards, melanin is distributed throughout the epidermis.	20
3.4	Action spectra of melanogenesis [141] (left) and erythema [118] (right).	21
4.1	Sketch illustrating the different light and skin interaction processes simulated by the proposed hyperspectral model (HyLloS). From left to right: surface reflection, absorption, transmission and subsurface reflection. Note that the distances that may separate light incidence (x_{i_1} to x_{i_4}) and outgoing (x_{o_3} and x_{o_4}) points are computed taking into account the physical distances that light travels within the cutaneous tissues.	22
4.2	Diagram showing the skin layers considered by the HyLloS model. The main light-absorbing spectral domains associated with each layer are identified as UV (ultraviolet), Vis (visible) and IR (infrared).	23
4.3	Flowchart depicting the general structure of the iterative random walk algorithm employed by HyLloS. The distances to the next attenuation events are computed using Equation 4.1.	24

4.4	Diagram illustrating a possible path (from left to right) that can be followed by a ray traversing an epidermal layer occupied by individual melanosomes (represented by prolate spheroids). The distance to the next melanosome is probabilistically computed according to a pathlength distribution. The orientation of the melanosome and the hitting point on its surface are also probabilistically generated. The light interaction with the melanosome is simulated, and the ray is either terminated inside the melanosome or scattered. In the latter case, the melanosome is discarded and a new one is generated. This process is repeated until the ray is either absorbed or scattered outside of the layer. The same stochastic procedure is employed for melanosome complexes.	26
5.1	Diagram depicting the main modules of the proposed framework for the simulation and visualization of skin tanning dynamics. Note that it employs a light interaction model, HyLloS (Chapter 4), to evaluate whether the dose of UVR impinging on a skin specimen is sufficient to trigger the stimulation of melanin production and skin thickening. This model is also used to translate the results from the tanning dynamics simulations to skin appearance attributes.	32
5.2	Diagram illustrating the melanin production and removal phenomena considered in our melanin dynamics simulations. The spheres represent melanosomes. The smaller spheres in the upper layers represent smaller melanosomes found in the upper layers of skin. The lighter spheres represent melanosomes encapsulating degraded melanin.	35
5.3	Effect of different melanin distributions on visible reflectance of a darkly pigmented specimen. Left: bar chart presenting the different distributions of melanin in colloidal and melanosome forms. The epidermal layers, namely stratum granulosum, stratum spinosum and stratum basale are denoted by sg, ss and sb, respectively. Top three bars are for the basal case and the bottom three bars are for the dispersed case. Right: visible reflectance between the two cases are significantly different even when the melanin content is the same.	40
6.1	Website for running the HyLloS model online [126].	46
6.2	Comparisons of modelled spectral curves obtained using DJ06 [50], BioSpec [18] and HyLloS models with measured NCSU spectral curves 117 (left) and 113 (right) [198]. The HyLloS curves on the left and right were computed using the pigmentation datasets S1 and S2 respectively (Tables 6.1 and 6.2).	47

6.3	Skin swatches generated using modelled spectral curves provided by DJ06 (left) and HyLloS (centre) models along with a reference swatch (right) generated using measured data (NCSU spectral curve 117) provided by Vrhel et al. [198]. The respective spectral curves are depicted in Figure 6.2 (left).	47
6.4	Skin swatches generated using modelled spectral curves provided by BioSpec (left) and HyLloS (centre) models along with a reference swatch (right) generated using measured data (NCSU spectral curve 113) provided by Vrhel et al. [198]. The respective spectral curves are depicted in Figure 6.2 (right).	48
6.5	Comparison of modelled subsurface scattering data obtained using HyLloS with measured subsurface scattering data provided by Bruls and van der Leun [28] for the epidermis of a lightly pigmented skin specimen considering normal incidence of UV light (at 302 nm). The modelled data was computed using the pigmentation dataset S2 (Tables 6.1 and 6.2). The insets depict orthographic projections of the measured and modelled subsurface scattering data presented in the graph.	48
6.6	Comparisons of modelled hyperspectral curves obtained using HyLloS with measured curves for a lightly pigmented specimen (left) provided by Cooksey and Allen [41] and a darkly pigmented specimen (right) provided by Jacquez et al. [93, 94]. The HyLloS curves (from 250 nm to 2500 nm) for the lightly and darkly pigmented specimens were computed using the pigmentation datasets S3 and S4 respectively (Tables 6.1 and 6.2).	49
6.7	Comparison of modelled BRDF curves (H) provided by HyLloS with measured BRDF curves (M) provided by Marschner et al. [116] for a lightly pigmented specimen considering two angles of incidence: 0° (left) and 60° (right). The modelled curves were obtained considering the pigmentation dataset S1 (Tables 6.1 and 6.2).	50
6.8	Scattering plots provided by HyLloS showing surface (R_s), subsurface (R_d), and total (R_t) reflectance distributions in the UV (left) and IR (right) domains. Note the more diffuse total reflectance distribution of IR light (below 1300 nm) as reported in the scientific literature [7, 78]. These plots correspond to normalized bidirectional reflectance values at 365 nm (left) and 1100 nm (right) multiplied by the cosine of the reflection angle. The bidirectional reflectance values were computed considering an angle of incidence of 45° and using the pigmentation dataset S1 (Tables 6.1 and 6.2).	50

6.9	Images showing distinct skin appearance features in the UV (left), visible (centre) and IR (right) spectral domains. These images were rendered using BSS-RDF (top row) and BRDF (bottom row) representations of spatial light distributions provided by the proposed hyperspectral model in these domains. Note that HyLloS can predictively simulate not only the intensification of pigmentation irregularities in the UV range, but also the “soft”, “ethereal” (more diffuse and less affected by the presence of pigmentation irregularities) appearance of human skin in the IR range [167], notably below 1300 <i>nm</i> [7]. The UV and IR responses (at 365 <i>nm</i> and 1100 <i>nm</i> respectively) are depicted using pseudo colour.	51
6.10	Images showing the effects of increased overall melanin pigmentation on skin UV responses as reported in the scientific literature [7,41,63,94,130]. Left: 1.5%. Centre: 7%. Right: 30%. The UV responses (at 365 <i>nm</i>) provided by HyLloS are depicted in pseudo colour. Polygonal mesh courtesy of XYZ RGB Inc.	52
6.11	Images showing the magnifying effects of water loss on skin IR responses as reported in the scientific literature [7, 9]. These effects were simulated by reducing the water content of the cutaneous tissues of a lightly pigmented specimen (1.5% epidermal melanin content) within physiological limits [24]. Left: No reduction. Centre: 20% reduction. Right: 40% reduction. The IR responses (at 1650 <i>nm</i>) provided by HyLloS are depicted in pseudo colour. Polygonal mesh courtesy of XYZ RGB Inc.	53
6.12	Images showing IR responses at 1200 <i>nm</i> (left) and 1400 <i>nm</i> (right) for a lightly pigmented specimen (1.5% epidermal melanin content). Note, as reported in the scientific literature [7,93], the disappearance of pigmentation irregularities that occurs beyond 1100 <i>nm</i> , as well as the more specular and darker appearance resulting from reduced subsurface scattering at a wavelength (1400 <i>nm</i>) characterized by strong water absorption. Both (pseudo colour) images had their brightness increased for visualization purposes.	54
6.13	Comparison of modelled results provided by HyLloS depicting the impact of melanin and blood on skin reflectance, which were obtained considering the complete dataset S3 as the baseline and two modified versions: with no melanin and no blood. Left: reflectance curves in the visible domain. Right: MSI values for each modified reflectance curve with respect to the baseline curve across the UV, visible, IR and the entire hyperspectral region of interest (250 <i>nm</i> to 2500 <i>nm</i>) denoted by “Hyper”.	55

6.14	Skin swatches illustrating the impact of melanin or blood removal on the visible appearance of human skin considering the complete dataset S3 as baseline (left) and two modified versions: with no melanin (centre) and no blood (right). . . .	55
6.15	Comparison of modelled results provided by HyLloS depicting the impact of DNA and keratin on skin reflectance, which were obtained considering the complete dataset S3 as the baseline, and two modified versions: with no DNA and no keratin. Left: reflectance curves in the UV domain. Right: MSI values for each modified reflectance curve with respect to the baseline curve across the UV, visible, IR and the entire hyperspectral region of interest (250 nm to 2500 nm) denoted by “Hyper”.	56
6.16	Skin swatches illustrating the impact of DNA or keratin removal on the UV appearance of human skin considering the complete dataset S3 as baseline (left) and two modified versions: with no DNA (centre) and no keratin (right). The UV responses are depicted in pseudo colour.	56
6.17	Comparison of modelled results provided HyLloS depicting the impact of water and lipids on skin reflectance, which were obtained considering the complete dataset S3 as the baseline and two modified versions: with no water and no lipids. Left: reflectance curves in the IR domain. Right: MSI values for each modified reflectance curve with respect to the baseline curve across the UV, visible, IR and the entire hyperspectral region of interest (250 nm to 2500 nm) denoted by “Hyper”.	57
6.18	Skin swatches illustrating the impact of water or lipids removal on the IR appearance of human skin considering the complete dataset S3 as baseline (left) and two modified versions: with no water (centre) and no lipids (right). The IR responses are depicted in pseudo colour.	57
6.19	Rendered images illustrating changes in the visible appearance of human skin considering an increase in epidermal melanin content from 1.5% (left) to 7% (right). Note that we employed a back/side light source to make the translucency effects prominent. Polygonal mesh courtesy of XYZ RGB Inc.	58

6.20	Images illustrating rendering applications of HyLIoS in the UV (left), visible (centre) and IR (right) spectral domains. The scene depicts an upper back/shoulder (epidermal melanin content equal to 1.5%) with sunscreen and water in an outdoor beech setting. The UV and IR responses (at 365 <i>nm</i> and 1650 <i>nm</i> respectively) are depicted using pseudo colour. The dark appearance of sunscreen and water outside the visible domain are attributed to their strong absorptive behaviour in the UV and IR regions respectively. Note that we have positioned the light source high above the subject in order to mimic a typical outdoor beach setting.	58
6.21	Simulated data illustrating the framework’s capability to account for the photoaddition phenomenon [173]. Left: two different UVR exposure dose schedules. Right: simulated melanin increase results provided by the framework. The simulations were performed considering a specimen with low constitutive pigmentation level (Tables 6.4 to 6.6).	61
6.22	Artistic conception illustrating a standard experimental setup used for tanning experiments. A template is placed on the body (left) to isolate patches of skin in order to administer distinct measured UVR doses (centre). The changes in these patches relating to different exposure doses (right) are then recorded.	62
6.23	Simulated physiological changes resulting from three tanning processes triggered by three distinct UVR exposure dose schedules. First column: exposure dose schedules employed by Miller et al. [121]. Second column: changes in relative melanin content, which is associated with this pigment’s distribution in the different epidermal layers, namely stratum basale (sb), stratum spinosum (ss) and stratum granulosum (sg). Third column: changes in total melanin content. Fourth column: changes in skin thickness. Fifth column: comparisons of simulated results with measured values provided by Miller et al. [121]. These comparisons are presented in terms of the change in the lightness L^* coordinate of the $L^*a^*b^*$ colour space, with the bars depicting the standard deviations from the measured mean values.	63
6.24	Sequence of images portraying the temporal changes in skin appearance as a result of the tanning processes described in Figure 6.23. The marked areas in the leftmost and rightmost images denote the boundaries of the in-between images. The top, middle and bottom tanned patches, in turn, correspond to the distinct exposure dose schedules provided in the top, middle and bottom rows of Figure 6.23, respectively.	63

6.25	Images illustrating the distinct UVR sensitivities of specimens characterized by increasing levels of constitutive pigmentation, from low (left) to high (right). The same exposure dose schedules presented in Figure 6.23 were applied to the three specimens. The tanning responses depicted in the patches correspond to day 20, and they were obtained using the data provided in Tables 6.4 to 6.6. . . .	64
6.26	Images illustrating the different tanning abilities of specimens characterized by increasing levels of constitutive pigmentation, from low (left) to high (right). The same exposure dose schedules presented in Figure 6.23 were applied to three specimens. The tanning responses depicted in the patches correspond to day 20, and they were obtained using the data provided in Tables 6.4 to 6.6. We note that the UVR dose intensities were scaled by factors of 1.4 and 2.4 for the specimens with intermediate and high constitutive pigmentation levels respectively [160,181].	64
6.27	Sequence of images illustrating changes in the appearance of an individual with a high tanning ability. Left: initial appearance just before sunbathing for several hours with an effective sunscreen applied on her back as indicated. Centre: noticeable darkening on the way home inside an airport 4 days after UVR exposure. Right: significant darkening from a well developed tan as seen before taking a shower 15 days after exposure. To facilitate visual comparisons, the same illumination was used in the rendering of all three images. Note that these images were generated using the data provided in Tables 6.4 (dataset \mathcal{L} , with $m_{p,i,f}$ of the stratum basale set to 0.0858), 6.5 and 6.6.	65
6.28	Images illustrating the visible skin appearance (left) and the corresponding UV appearance (right) of an individual with a mild tanning ability. The top row depicts the pre-exposure appearance with an effective sunscreen applied to one side of her face (depicting a glossier appearance). The bottom row depicts the appearance contrast between the untanned and tanned sides of her face 15 days after UVR exposure. Note that these images were generated using the data provided in Tables 6.4 (dataset \mathcal{L}), 6.5 and 6.6, and UV appearance attributes (at 365 nm) are depicted using pseudo colour.	66

6.29	Frames from an animation illustrating nonlinear appearance changes of an individual over a period of 30 days resulting from an initial UVR exposure of several hours on a beach. The first three rows present frames (from left to right, top to bottom) depicting the sequence of daily tanning variations. The bottom row presents selected frames (from left to right) showing the initial pigmentation level at day 1, the peak pigmentation level at day 10 and faded pigmentation levels at days 20 and 30. Note that these frames were generated using the data provided in Tables 6.4 (dataset \mathcal{I}), 6.5 and 6.6.	67
A.1	Absorption spectra of the main absorbers acting within the skin tissues. Top left: absorptance curves for solid keratin over a distance of $4 \mu m$ [22], $50 \mu g/mL$ of DNA, and $15 \mu mole/L$ of urocanic acid over a distance of $1 cm$ [38, 137, 179, 211]. Top centre: extinction coefficient (ϵ) curves for melanin [91]. Top right: molar extinction coefficient (ϵ_m) curves for functional hemoglobins [152]. Bottom left: molar extinction coefficient (ϵ_m) curves for dysfunctional hemoglobins [157, 171, 209]. Bottom centre: molar extinction coefficient (ϵ_m) curves for beta-carotene and bilirubin [153]. Bottom right: specific absorption coefficient (s.a.c.) curves for water [139, 150] and lipids [4, 154, 195].	94
B.1	Data used to guide the selection of parameter values for the melanin dynamics component of the tanning simulation framework. From left to right: data for lightly, moderately and darkly pigmented specimens. Top row: comparisons of measured pigmentation distribution changes with the simulated pigmentation distribution changes. The measured values provided by Tadokoro et al. [181] for the stratum basale, stratum spinosum and stratum granulosum are represented by circles, triangles and squares, respectively. The simulated values for the stratum basale stratum, spinosum and stratum granulosum are represented by the solid, dashed and dash-dotted lines, respectively. Bottom row: corresponding simulated overall pigmentation change. The simulated data was generated using the melanin dynamics component of the framework described in Section 5.1 along with the parameter values presented in Tables 6.4 and 6.5 considering one initial exposure dose of 1 MMD.	97

B.2	Data used to guide the selection of parameter values for the thickness dynamics component of the tanning simulation framework. The measured data was provided by Lopez et al. [112]. The simulated data was generated using the thickness dynamics component of the framework described in Section 5.2 along with the parameter values presented in Table 6.6.	97
C.1	Reflectance curves for a lightly (S3) and a darkly (S4) pigmented specimen considering the baseline and colloidal cases.	100
C.2	RMSE values for the baseline (case) reflectance curves of a lightly (S3) and a darkly (S4) pigmented specimen with respect to their corresponding colloidal (case) reflectance curves. The spectral regions denoted by UV, Visible, NIR and VNIR (Visible–NIR) go from 250 nm to 400 nm, 400 nm to 700 nm, 700 nm to 1400 nm and 400 nm to 1400 nm, respectively.	101
C.3	Reflectance curves for a lightly (S3) and a darkly (S4) pigmented specimen considering the dispersion and colloidal cases.	101
C.4	RMSE values for the dispersion (case) reflectance curves of a lightly (S3) and a darkly (S4) pigmented specimen with respect to their corresponding colloidal (case) reflectance curves. The spectral regions denoted by UV, Visible, NIR and VNIR go from 250 nm to 400 nm, 400 nm to 700 nm, 700 nm to 1400 nm and 400 nm to 1400 nm, respectively.	102
C.5	Variations (bars) in the reflectance values of a darkly pigmented specimen considering melanosomes located in the stratum basale and dispersed throughout the epidermis. The corresponding colloidal (case) reflectance curve is included for comparison.	102
D.1	Plot depicting the skin hyperspectral reflectance database (SHRD) employed in this investigation.	106
D.2	Modelled (HyLIoS) and reconstructed (PCA using two components) curves for specimen N32. Error bars represent differences between the curves, magnified by a factor of 10. Resulting RMSE values for the UV–Visible, IR-A and IR-B regions were 0.0117, 0.0118 and 0.0109, respectively.	108
D.3	Skin swatches in the UV (left), visible (centre) and IR (right) ranges obtained for specimen N32 using PCA with one component (top), two components (middle) and the original modelled curve (bottom) provided by HyLIoS.	109

D.4	Modelled (HyLloS) and reconstructed (PCA using three components) curves for specimen N135. Error bars represent differences between the curves, magnified by a factor of 10. Resulting RMSE values for the UV-Visible, IR-A and IR-B regions were 0.0209, 0.0172 and 0.0140, respectively.	109
D.5	Modelled (HyLloS) and reconstructed (PCA using four components) curves for specimen N127. Error bars represent differences between the curves, magnified by a factor of 10. Resulting RMSE values for the UV-Visible, IR-A and IR-B regions were 0.0127, 0.0105 and 0.0087, respectively.	109
D.6	Modelled (HyLloS) and reconstructed (PPCA using two components) curves for specimen N32. Error bars represent differences between the curves, magnified by a factor of 10. Resulting RMSE values for the UV-Visible, IR-A and IR-B regions are 0.0024, 0.0058 and 0.0024, respectively.	110
D.7	Modelled (HyLloS) and reconstructed (PPCA using three components) curves for specimen N135. Error bars represent differences between the curves, magnified by a factor of 10. Resulting RMSE values for the UV-Visible, IR-A and IR-B regions are 0.0018, 0.0026 and 0.0013, respectively.	110
D.8	Modelled (HyLloS) and reconstructed (PPCA using four components) curves for specimen N127. Error bars represent differences between the curves, magnified by a factor of 10. Resulting RMSE values for the UV-Visible, IR-A and IR-B regions were 0.0038, 0.0031 and 0.0010, respectively.	111
D.9	Skin swatches in the UV (left), visible (centre) and IR (right) ranges obtained for specimen N127 using PCA with four components (top), PPCA with four components (middle) and the original modelled curve (bottom) provided by HyLloS. . .	111
E.1	The equipment used to capture the hyperspectral photographs presented in this thesis. Left: the modified Canon EOS 700D camera. Right: the filters and step rings. The filters, from left to right: Baader U-Filter, Kolari Vision hot mirror and Kolari Vision K720.	113
E.2	Photographs of a pair of polarized sunglasses (Oakley Whisker) taken in different spectral domains. Counterclockwise, from top left: visible, UV, NIR and full-spectral. Note the opacity and reflective quality of the lenses in the visible and UV photographs in comparison to the transparency in the NIR photograph. . . .	115

- E.3 Photographs of sunscreens taken in different spectral domains. Counterclockwise, from top left: visible, UV, NIR and fullspectral. The sunscreens, from left to right within each photograph: Banana Boat Sunscreen Oil Spray SPF 15, Coppertone Sunscreen Lotion SPF 30, Hawaiian Tropic Sheer Touch Oil-free Sunscreen SPF 45, Shiseido Hada Senka Mineral Water UV Gel SPF 50 PA+++ and Garnier Ombrelle Complete Lightweight Lotion SPF 60. In the UV photograph, the sunscreens appear very dark, primarily reflecting specular components. In the NIR photograph, the sunscreens still reflect a substantial amount of light since the water present in their composition is characterized by a strong light absorption behaviour only at longer wavelengths beyond the sensitivity of the camera sensor. The Shiseido sunscreen appears to have higher reflectance than the other sunscreens in the UV. This might be due to the Shiseido sunscreen reflecting UV, besides just absorbing, as its strategy to limit skin exposure to UV light. The “dirtiness” of the bottles in the UV domain, which is imperceptible in the other photographs, may be due to the screens’ residue from previous uses. Another interesting feature is the transparency of the Banana Boat bottle in the NIR domain. 116
- E.4 Photographs of a pair of hands taken in different spectral domains. Counterclockwise, from top left: visible, UV, NIR and fullspectral. A sunscreen (Garnier Ombrelle Complete Lightweight Lotion SPF 60) was applied to the right hand. Note the significant darkening effect of the sunscreen’s absorptive properties in the UV photograph in contrast to its slightly specular appearance in the other photographs. Again, we remark that in the NIR photograph, the sunscreen is almost imperceptible since the water present in its composition is characterized by a strong light absorption behaviour only at longer wavelengths beyond the sensitivity of the camera sensor. 117
- E.5 Photographs of trees taken in different spectral domains. From top to bottom: visible, UV, NIR and fullspectral. While in the visible domain, the plant leaves’ reflectance profile is characterized by higher values in the green region (500 *nm* to 600 *nm*) of the light spectrum, in the NIR domain, particularly in the range sampled by the selected equipment (700 *nm* to 1000 *nm*), their reflectance profile is characterized by consistently high values, leading to a pale appearance illustrated in the NIR photograph. 118

- E.6 Photographs of the sky taken in different spectral domains. From top to bottom: visible, UV, NIR and fullspectral. Note the light grey sky in the UV and dark sky in the NIR photographs. These appearances may respectively be caused by the plentiful and scarce scattering of light by the atmosphere in the corresponding spectral domains. Note that the position of the clouds has changed over time. . . . 119
- E.7 Photographs of a Lego spaceship taken in different spectral domains. Counter-clockwise, from top left: visible, UV, NIR and fullspectral. Note how the yellow-green pieces appear to be opaque in the UV photographs. This may be due to the presence of fluorescent materials in their composition. These materials would absorb UV light to reemit at a different wavelength in the visible domain. The opacity of these pieces in the UV photograph presents a stark contrast to their transparency in the IR photograph. Finally, the presence of dust (*e.g.*, on the model's main canopy) is also more noticeable in the UV photograph. 120
- E.8 Photographs of a Lego airplane taken in different spectral domains. Counter-clockwise, from top left: visible, UV, NIR and fullspectral. Note the high reflectance of the red and some of the blue elements in the NIR domain. This may be caused by the presence of NIR reflecting dyes. Another detail to notice (also depicted in some of the elements in Figure E.7) is the different appearance of the yellow-green pieces (minifigures' visors) in the different spectral domains. . . . 121

List of Tables

6.1	Values for specimen dependent parameters employed by HyLloS. The datasets S1, S2 and S3 correspond to specimens with relative low level of melanin pigmentation [41,198], while dataset S4 corresponds to a specimen with a high level of melanin pigmentation [93, 94]. Accordingly, the simulations consider the melanosomes distributed as complexes (Figure 3.1 (left)) when using datasets S1, S2 and S3, and as individually dispersed particles (Figure 3.1 (right)) when using dataset S4 [136,180]. *Note that in the case of the comparisons involving goniometric data (Figures 6.7 and 6.8), the aspect ratio of the surface folds was set to 0.3 to approximate the description of the lightly pigmented individual whose measured skin goniometric data [116] was employed as a reference in this thesis.	43
6.2	Values for specimen independent parameters employed by HyLloS. The refractive indices for the skin layers were measured at 1300 nm as reported in the listed sources.	44
6.3	MSI values were computed for the spectral domain, denoted by “SD”, in which the removal of each selected material has the highest impact. The MSI values computed considering the entire hyperspectral region of interest (250 nm to 2500 nm), denoted by MSI_H , are also included for reference.	54
6.4	Values for constitutive pigmentation dependent parameters employed in the melanin dynamics component of the framework. The three parameter datasets associated with distinct constitutive pigmentation levels, namely \mathcal{L} (Low), \mathcal{I} (Intermediate) and \mathcal{H} (High), are based on experimental measurements performed by Tadokoro et al. [181].	60
6.5	Values for constitutive pigmentation independent parameters employed in the melanin dynamics component of the framework. These values are based on experimental measurements performed by Tadokoro et al. [181].	60

6.6	Values for constitutive pigmentation independent parameters employed in the thickness dynamics component of the framework. These values are based on experimental measurements performed by Lopez et al. [112].	61
D.1	Maximum RMSE values computed for the PCA reconstructed curves (250 <i>nm</i> to 2500 <i>nm</i>) with respect to the curves for the 96 melanotic, 48 amelanotic and all 144 specimens depicted in the SHRD obtained using the HyLloS model. The values in boldface for the melanotic and amelanotic subsets as well as the entire database correspond to specimens N32, N135 and N127, respectively.	108

List of Acronyms

UVR	<i>ultraviolet radiation</i>	2
UV	<i>ultraviolet</i>	3
IR	<i>infrared</i>	3
CIE	<i>Commission Internationale de l'Éclairage (International Commission on Illumination)</i>	3
HyLIoS	<i>hyperspectral light impingement on skin (light interaction model)</i>	5
PCA	<i>principal component analysis</i>	8
BSSDF	<i>bidirectional scattering-surface distribution function</i>	12
BSSRDF	<i>bidirectional scattering-surface reflectance distribution function</i>	12
BSSTDF	<i>bidirectional scattering-surface transmittance distribution function</i>	12
BSDF	<i>bidirectional scattering distribution function</i>	12
BRDF	<i>bidirectional reflectance distribution function</i>	12
BTDF	<i>bidirectional transmittance distribution function</i>	12
SPT	<i>Fitzpatrick skin phototype</i>	20
MED	<i>minimum erythema dose</i>	20
MMD	<i>minimum melanogenesis dose</i>	20
SED	<i>standard erythema dose</i>	21
MED_{SED}	<i>minimum erythema dose in terms of standard erythema dose</i>	21
MMD_{SED}	<i>minimum melanogenesis dose in terms of standard erythema dose</i>	21
PDF	<i>probability distribution function</i>	27
MMT	<i>minimum melanogenesis threshold</i>	33
MAS	<i>melanogenesis action spectrum</i>	33
EMS	<i>effective melanogenesis signal</i>	34
EAS	<i>erythema action spectrum</i>	37
ETS	<i>effective thickening signal</i>	38
DJ06	<i>skin appearance model proposed by Donner and Jensen in 2006 [50]</i>	45
BioSpec	<i>biophysically-based spectral model of light interaction with human skin [14, 104]</i>	45

NCSU	North Carolina State University	45
MSI	mean sensitivity index	52
RMSE	root mean square error	100
NIR	near-infrared	100
PPCA	piecewise PCA	105
SVD	singular value decomposition	105
SHRD	skin hyperspectral reflectance database	106
SPF	sun protection factor	114

List of Symbols

f	BRDF	12
dL_p	propagated radiance	12
φ_p	direction of propagated radiance	12
L_i	incident radiance	12
φ_i	direction of incident radiance	12
θ_i	polar angle associated with the direction of incident radiance	12
$d\omega_i$	differential solid angle at which L_i arrives	12
λ	wavelength	23
μ	spectral attenuation coefficient	23
D	distance traversed by a ray in a random walk iteration step	23
ξ_i	i^{th} random variable	23
oh	oxyhemoglobin	25
dh	deoxyhemoglobin	25
ch	carboxyhemoglobin	25
mh	methemoglobin	25
sh	sulfhemoglobin	25
bc	beta-carotene	25
bil	bilirubin	25
μ_a^p	volumetric absorption coefficient of the papillary dermis	25
ζ_i	specific absorption coefficient of a given absorber i	25
v_i^p	volume fraction of a given absorber i within the papillary dermis	25
v_i^b	volume fraction of a given absorber i within the whole blood	25
μ_g	geometric attenuation coefficient of a melanosome	27
S	surface area of a melanosome	27
V	volume of a melanosome	27
v	volume fraction occupied by melanosomes	27
a	semi-minor axis of a melanosome	27
b	semi-major axis of a melanosome	27

c	$\sqrt{(1 - a^2/b^2)}$	27
P_m	probability distribution function of orientation of prolate spheroid	27
α	polar angle of incident ray	27
β	azimuthal angle of incident ray	27
χ_1	cross sectional area of spheroid associated with its minor axis	27
χ_2	cross sectional area of spheroid associated with its major axis	27
\vec{r}_p	perturbed ray	28
\vec{n}	inward normal at intersection point	28
r_s	radius of sphere	28
n_m	ratio of the diameter of sphere to minor axis of an encapsulated spheroid	28
θ_m	polar scattering angle from melanosome	28
θ_o	mean polar scattering angle from melanosome	28
μ_s^R	Rayleigh scattering coefficient	29
r	radius of connective fibres	29
v_f	volume fraction occupied by connective fibres	29
η	ratio between the refractive index of scatters to refractive index of surrounding medium	29
θ_R	polar angle of Rayleigh scattering	29
P_s	probability distribution function of polar angle of surface normal	30
θ_s	polar angle of surface normal	30
s	surface roughness parameter	30
Ψ_o	minimum melanogenesis threshold	33
α_m	melanogenesis action spectrum	33
ψ_o	spectral minimum melanogenesis dose	33
A	spectral absorptance of skin	33
Ψ	effective melanogenesis signal	34
ψ	spectral (radiant) exposure dose	34
t	time	34
d	dose (ratio between Ψ and ψ_o)	34
e_o	energy (relative to MMD and MAS) retained within the skin	34
δ_{e_o}	decay of e_o	34
s_o	rate of production of the melanogenesis signal substance	34
e	defined to ensure that a tanning response occurs only when the EMS exceeds the MMT	34
s	amount of signal substance associated with the melanogenesis process	34
$m_{p,i}$	melanin production rate in a given layer i	35
$m_{t,i}$	fraction of melanin transferred from layer i to the layer above	35

$m_{p,i,c}$	constitutive melanin production rate for layer i	35
$m_{t,i,c}$	constitutive melanin transfer rate for layer i	35
$m_{p,i,f}$	facultative melanin production rate for layer i	35
$m_{t,i,f}$	facultative melanin transfer rates for layer i	35
M	factor used to modulate the facultative melanin production and transfer rates	35
κ	Hill cooperativity coefficient employed by M	36
ω	Hill dissociation coefficient employed by M	36
\hat{m}_i	relative melanin content in layer i	36
δ_m	fraction of melanin that remains from melanin degradation	36
$\Delta\hat{m}$	normalized increase in melanin pigmentation	36
\bar{m}_i	original melanin content for layer i	37
τ_i	original thickness of layer i	37
τ_e	original thickness of the epidermis	37
Ψ'_\circ	minimum thickening threshold	37
α_e	erythema action spectrum	37
ψ'_\circ	spectral minimum erythema dose	37
Ψ'	effective thickening signal	38
d'	dose (ratio between Ψ' and Ψ'_\circ)	38
e'_\circ	energy (relative to MED and EAS) retained	38
$\delta_{e'_\circ}$	decay of e'_\circ	38
s'_\circ	rate of production of the hyperplasia signal substance	38
$\delta_{s'_\circ}$	decay of s'_\circ	38
e'	defined to ensure that a skin thickening response occurs only when the ETS exceeds the MTT	38
s'	signal substance associated with the hyperplasia process	38
$\delta_{s'}$	decay of s'	38
τ_p	generation of skin cells	38
$\tau_{p,base}$	baseline skin cell production rate	39
$\tau_{p,tan}$	the increase in skin cell production rate	39
M'	factor that modulates the increase in skin cell production rate	39
κ'	Hill cooperativity coefficient employed by M'	39
ω'	Hill dissociation coefficient employed by M'	39
τ	skin thickness	39
δ_τ	loss in skin cells	39
$\Delta\tau$	normalized skin thickness change	39
ρ_b	reflectance associated with baseline dataset	53
ρ_m	reflectance associated with modified dataset	53

c_c	concentration	94
ε	molar extinction coefficient	94
M_w	molar weight	94
A_b	absorbance	94
ζ	absorption coefficient	95
δ	density	95
ρ_α	reference reflectance used in RMSE computations	100
ρ_β	test reflectance used in RMSE computations	100
N	number of wavelengths	100
s_x	number of specimens in M_x	105
w_x	number of wavelength samples in M_x	105
M_x	matrix representing a hyperspectral reflectance database	105
V_x	basis of principal components	105
C_x	coordinates (coefficients) relative to the basis	105
s'_x	reduced number of components	105
C'_x	compressed version of C_x	105
V'_x	compressed version of V_x	105
ρ_r	reconstructed reflectance	105
$C'_{x,i}$	i^{th} row of matrix C'_x	105

1 Introduction

“ If computer graphics is to have a role in improving the future of our civilization, the real value will be in its applications to science, engineering and design.

”
Donald Greenberg
Steven A. Coons Award Lecture
SIGGRAPH, 1987

The application of computer science expertise to address problems in the physical and life sciences is becoming increasingly relevant. *In silico* laboratories can accelerate research processes by identifying promising hypotheses and focusing resources on worthwhile avenues of investigation. Such *in silico* tools are also assisting in studies where traditional wet laboratory conditions cannot be directly applied. For example, it might be too expensive to acquire or too complex to manufacture certain materials for measurements and manipulation [17]. Maintaining good ethical practices may limit the types of experiments that can be carried out on live subjects [144]. Some problems may be too large or complex to study without computational tools [187]. These obstacles present opportunities for computer science to grow as a discipline by augmenting its range of applications [156]. By directly addressing important social problems in topics such as education, environment and health care, computer science can have an even larger impact in improving the general quality of life around the world [101].

Computer graphics remains one of the most pervasive core areas of computer science. The general population is exposed to it on a daily basis in its various forms ranging from tools for graphic design in print and digital media to simulations for virtual worlds in video games and visualization of special effects in motion pictures. This area of computer science combines a wide variety of expertise from a diverse range of fields spanning the arts, sciences and engineering [71]. Therefore, it is straightforward for computer graphics techniques to reciprocate and have its research be applied beyond purely visual applications [58]. For instance, interactive graphics such as computer-aided drafting can be used to assist in the design and testing of

the structural, electrical and thermal properties of mechanical and electrical components. Simulations and animations are also used for science and engineering to model natural phenomena like fluid flow and physiological systems.

The work presented in this thesis addresses core topics in computer graphics such as realistic image synthesis and material appearance modelling. It also expands the boundaries of computer science by providing computational tools for interdisciplinary* studies in the life and physical sciences, as well as biomedical engineering. We achieve these goals by expanding the scope of light interaction models for skin, one of the most ubiquitous and optically complex materials, by simultaneously extending the spectral (*i.e.*, associated with the wavelength of light) and temporal dimensions beyond those offered by previous related works.

1.1 Research Motivation

A topic of active research in computer graphics is the realistic representations of virtual characters which has created a demand for visualization frameworks that can simulate the appearance of complex organic materials [54]. This has prompted the computer graphics community to study and reproduce the optical properties of human skin, one of the most widespread of these materials. The different research initiatives in this area have focused on a set of non-exclusive technical priorities, ranging from the generation of believable images of human skin (*e.g.*, [23, 50]) to the predictive modelling of its interactions with light (*e.g.*, [14, 104]) and the efficient rendering of its appearance attributes (*e.g.*, [47, 96]). Despite the significant advances achieved by the computer graphics community with respect to the modelling of material appearance, organic materials, including human skin, continue to represent an ongoing challenge in this area due to their inherent optical complexity [12].

One dimension of this complexity is the ability to change over time due to different external factors that can alter their physiological status. Despite this fact, the skin on a digital character is usually considered as an independent component from the rest of the setting. Moreover, the causal relationship between environmental stimuli, such as ultraviolet radiation (UVR), and skin appearance changes is largely overlooked. It has been illustrated [54, 99, 119], however, that material appearance changes associated with environmentally-triggered processes can contribute to a significant sense of realism by incorporating subtle impressions of natural phenomena to usually pristine digital scenes. For example, many skin appearance changes distinctly noticeable in the visible domain, such as tanning [32], freckling [63] and photoaging [169], are caused

*In this thesis, “interdisciplinary” refers to theoretical or applied research that “draws insights from relevant disciplines and integrates those insights into a more comprehensive understanding” as defined by Newell [127].



Figure 1.1: Photographs of a woman taken in the different spectral domains. From left to right: UV, visible and IR. Note the intensification of pigmentation irregularities (employed in appearance-based cancer prevention initiatives [63, 115]) and more specular appearance in the UV range, as well as the more diffuse, “ethereal” skin appearance that can be obtained in the IR domain (employed in artistic applications [167]). The UV and IR photos are depicted using pseudo colour. Technical details regarding how these photographs were acquired are presented in Appendix E.

by natural processes triggered by exposure to ultraviolet (UV) and infrared (IR) light[†]. In order to predictively simulate these processes, it is necessary, in turn, to employ models that can correctly account for light and skin interactions within and outside the visible domain.

However, to date, the bulk of the work on light and skin interactions within the computer graphics field has been aimed at static skin imaging in the visible domain. In fact, only recently, computer graphics researchers have started to look more closely into the hyperspectral domain[‡], spanning from the UV to the IR regions of the light spectrum, in order to broaden the scope of traditional rendering frameworks [98]. Accordingly, existing skin appearance models have been primarily employed in image synthesis applications (*e.g.*, [51, 95]) as well as in biomedical investigations (*e.g.*, [13, 30]) centred on the visible appearance attributes of human skin.

[†]According to the Commission Internationale de l’Éclairage (CIE), the UV, visible and IR spectral domains go from 100 *nm* to ≈ 400 *nm*, ≈ 400 *nm* to ≈ 700 *nm* and ≈ 700 *nm* to 1 *mm*, respectively [40]. For practical reasons (*e.g.*, data scarcity), we consider in this investigation these spectral regions to go from 250 *nm* to 400 *nm*, 400 *nm* to 700 *nm* and 700 *nm* to 2500 *nm*, respectively.

[‡]In the context of the investigations described in this thesis, “hyperspectral” refers to the broad spectral region encompassing the UV, visible and IR domains in conjunction with high-resolution spectral sampling within this region [193].

The rendering and investigation of phenomena affecting skin appearance attributes within broader hyperspectral and temporal domains can also lead to a diverse scope of applications in the life and health sciences. For example, the visibility of pigmentation irregularities, such as freckles, moles and other forms of melanin clumping, is accentuated in the UV domain (Figure 1.1 (left)). Predictive images and animations depicting the presence and development of these features can be employed in scientific investigations for the deeper understanding of related physiological processes including skin cancer. They can also be used in appearance-based interventions aiming at increasing the willingness of individuals to adopt sun protection measures that can reduce photodamage effects and skin cancer risk [115]. In addition, the modelling of skin hyperspectral responses can be utilized in noninvasive procedures of relevance for medicine and industry. For example, UV responses can be used in the assessment of the intrinsic photoprotective properties of a skin specimen [130], while IR responses can be used in the assessment of skin hydration [9], a key factor contributing to skin health, as well as play fundamental roles in remote sensing [11, 27, 132] and biometric technologies [178, 201] by exhibiting distinguishing appearance-based features.

Modelling of skin appearance beyond the visible domain also offers a myriad of creative opportunities for aesthetic applications. For example, in the IR region, notably below 1300 *nm*, one can observe a “soft”, more diffuse skin appearance (Figure 1.1 (right)), which is also less influenced by pigmentation irregularities [7, 59]. These appearance features allow for unique, artistic images of human subjects by eliciting the elegant and “ethereal” appearance of skin under IR light [167].

Overall, light and skin interactions in the hyperspectral and temporal domains are pertinent in a wide variety of fields for a host of different types of applications. However, there have been relatively few works that specifically address the simulation of relevant phenomena. This opportunity has motivated the work presented in this thesis. In the next section, we outline the specific contributions of our research.

1.2 Summary of Original Contributions

Throughout this thesis, we consider the following question:

How can we predictively simulate light interactions with human skin beyond the visible spectral domain as well as associated time-dependent physiological changes that affect its appearance?

We explore this question through the development of a novel light interaction model and tanning simulation framework. The former focuses on the hyperspectral aspect of the question while the latter focuses on the temporal aspect. The main contributions of this work are as follows:

1. **The first hyperspectral skin appearance model capable of predictively simulating both the spectral and spatial distributions of light interacting within this complex biological material in the UV, visible and IR domains, from 250 nm to 2500 nm [34].**

The first principles approach used in the design of this model, henceforth referred to as HyLloS (*Hyperspectral Light Impingement on Skin*), takes into account not only the detailed layered structure of the skin tissues, but also the particle nature of its main light attenuation agents, namely the melanosomes (spheroidal melanin-containing organelles [136]). Instead of relying on Mie theory based approximations in which light attenuation agents are usually represented by uniformly distributed spheres, we probabilistically incorporate the melanosomes' size, shape, orientation and distribution into our light transport simulations. These also account for the hyperspectral absorption and scattering properties of the remaining light attenuation agents found in each layer. As a result, the model can predictively account for phenomena that significantly affect skin spectral responses within and outside the visible domain such as light detour and sieve effects [29, 107], as well as the positional dependence [129] of light interacting with a given skin specimen.

2. **The first framework for the predictive simulation and visualization of time-dependent skin appearance changes resulting from tanning elicited by UVR exposure.**

This complex natural phenomenon is responsible for some of the most common and visually striking appearance variations observed in human skin. It encapsulates the two main adaptive mechanisms developed by this light sensitive organ to guard against the harmful effects of UVR, namely stimulation of melanin synthesis [26] and skin thickening (hyperplasia) [112]. These mechanisms are simulated using a physiologically-based approach that accounts for the distinct degrees of UVR sensitivity of various skin specimens and the effectiveness of different UVR wavelengths at eliciting tanning responses. This framework was designed to have a robust, and yet flexible architecture capable of providing predictive results for different applications. We demonstrate its predictive capabilities by quantitatively and qualitatively comparing simulated data with measurements and visual observations of related physiological changes reported in the scientific literature.

In addition, we provide image sequences illustrating time-dependent variations in skin appearance following tanning processes guided by distinct levels of adaptation to UVR exposure. Note that the execution of essential tasks within the proposed framework requires the use of a light interaction model capable of providing predictive results in the UV region of the light spectrum. To achieve this, such a model, in turn, needs to account for the particle nature of light attenuation agents within the skin tissues in this spectral domain. These requirements represented the central motivations for the development of HyLioS since a model with such characteristics was not available in the public domain when this research was conducted.

The research described in this thesis advances the current state of the art within and outside computer graphics. Besides enabling the generation of appearance attributes of skin beyond the visible spectral domain and animations depicting skin appearance changes triggered by UVR exposure, the proposed model and framework provide a foundation for the predictive simulation and visualization of related natural phenomena in both spectral and temporal domains. From a broader scientific perspective, this interdisciplinary research integrates computer science with applied optics and biology. It accomplishes this by applying computer graphics and numerical techniques to establish an *in silico* platform for the transparent and replicable testing of new hypotheses regarding photobiological processes affecting the appearance and the health status of human skin. It has already made such contributions by addressing topics regarding the interpretation of skin spectral signatures for inversion procedures (Appendix C) [11, 36], practical issues involving large databases of skin reflectance (Appendix D) [35] and methodologies for screening and monitoring of ubiquitous medical conditions (*e.g.*, anemia [15]). We expect it to assist in the investigation of additional important health related questions such as how skin pigmentation can be regulated [207] and how harmful effects of UVR, which can lead to serious medical conditions such as skin cancer, can be mitigated by induced pigmentation [123].

1.3 Document Organization

Some of the contents of this thesis have previously appeared in publications [11, 34, 35, 36]. They have been modified to be incorporated into this unified document. The remainder of this thesis is structured as follows:

- Chapter 2 presents an overview of the concepts regarding the measurement of appearance used in this thesis as well as a survey of related work with a focus on relevant research from computer graphics. Initially, this chapter reviews how light propagated

from a material can be defined in terms of its spectral and spatial distributions as well as the terms used to quantify these distributions such as reflectance and transmittance for spectral distributions and the various distribution functions for spatial distributions. It then discusses the two main classes of algorithms used in the modelling of skin appearance, namely deterministic and nondeterministic, as well as the different techniques used to simulate changes in material appearance over time. Advantages and pitfalls of these various methods are highlighted and open problems that the proposed model and framework address are identified.

- Chapter 3 reviews the optical properties and photobiology of skin. It includes a detailed description of relevant materials and structures that absorb and scatter light. Special attention is given to melanosomes whose particle nature is a key and often overlooked factor in how skin attenuates light. This is primarily due to detour and sieve effects which are also reviewed in this chapter. Since the proposed work involves not only how skin propagates incident radiation, but also how it actively responds to incident radiation, namely UVR, this chapter closes with an overview of concepts and terminology of relevant skin physiological changes.
- Chapter 4 introduces the HyLIoS model. It describes the first principles approach employed by HyLIoS and implemented using stochastic algorithms to model light and skin interactions. Within its algorithmic formulation, light interacting with the skin is simulated using iterative random walks through a layered structure. While most light interactions are accounted for using ray optics, several small-scale phenomena are accounted for using wave optics.
- Chapter 5 introduces the tanning simulation framework. It describes the two main components of this framework that address different changes in physiology related to tanning, namely change in melanin content and distribution, and increase in skin tissue thickness. We note that each of these components can initially employ a light interaction model to evaluate the effectiveness of an incident UVR dose.
- Chapter 6 describes the evaluation procedures used to demonstrate the predictive capabilities of the HyLIoS model (Chapter 4) and the tanning simulation framework (Chapter 5). The evaluation of predictive simulations should involve the comparison of their results with physical measurements whenever such data is available [70]. Accordingly, the proposed model and framework are primarily evaluated through quantitative comparisons with measured data and qualitative comparisons with empirical observations reported in the literature. In addition, this chapter includes images to further illustrate their predictive capabilities with respect to the simulation of characteristic trends in the variation of

skin appearance attributes within and outside the visible domain. The chapter also contains a concise discussion of usability and performance issues regarding both the HyLloS model and tanning simulation framework as well as an input sensitivity analysis specific to HyLloS.

- Chapter 7 closes the main body of this thesis with a summary of the main contributions of this work as well as directions for future research.

This thesis also includes several appendices. These are organized in the following manner:

- Appendix A presents supplementary information regarding the biophysical data (Section 6.1.1) used in the proposed light interaction model (Chapter 4). It includes the plots of the absorption spectra of the main absorbers in the skin tissues, as well as additional formulae and biophysical constants needed to derive relevant spectral absorption coefficients.
- Appendix B describes how the supporting data (Section 6.2.1) for the tanning simulation framework (Chapter 5) was derived. Time-dependent data from the scientific literature regarding changes in melanin content and skin tissue thickness were used to guide the selection of these parameter values.
- Appendix C provides additional results regarding the effects of melanin and melanosome distribution on skin reflectance. These effects are examined by altering the melanin and melanosome distribution patterns of two skin specimens while keeping the overall melanin content constant. This study was conducted using the HyLloS model (Chapter 4) and, besides highlighting the importance of taking into account detour and sieve effects (Chapter 3), it illustrates the type of scientific investigation for which the proposed model is an asset.
- Appendix D explores another application of the HyLloS model (Chapter 4). Here, the proposed model is used to study the effectiveness of principal component analysis (PCA) on the compression of skin reflectance databases. These databases are of value for research initiatives across different fields including the development of future light and skin interaction models. These, in turn, can be employed in the formulation of techniques for screening and assessment of cutaneous tissues' biophysical properties. This appendix also investigates the use of a biophysically-based piecewise application of PCA to achieve results with a higher accuracy to cost ratio in comparison with the standard PCA approach.

- Appendix E discusses practical insights relating to hyperspectral photography that were acquired during the course of this research. This appendix also includes additional photographs that highlight the distinct appearance of various objects in the different spectral domains.

2 Related Work

In this chapter, we briefly review key developments and relevant research efforts on the modelling of skin appearance and material appearance changes, with a focus on work within computer graphics. For the sake of clarity, we begin with an overview of fundamental concepts associated with the study of material appearance.

Although the bulk of this chapter is devoted to related work involving human skin, we remark that a detailed survey on techniques and models for skin rendering is beyond the scope of this thesis. The reader interested in a more thorough examination of this body of work, especially outside the computer graphics domain, is referred to comprehensive texts on this topic [18, 86, 191].

2.1 Measurement of Appearance Concepts

The visual* impression exhibited by a material is referred to as its appearance. The full set of tractable data that defines this characteristic is referred to as its measurement of appearance [85]. These quantities can be divided into two groups, namely those that involve the spectral distribution and those that involve the spatial distribution of the propagated light (Figure 2.1). Variations in the spectral distribution affect properties such as the hue, lightness and saturation of the material. Variations in the spatial distribution affect properties such as glossiness, lustre and translucency. We present a concise description of these concepts in the remainder of this section. These concepts follow those previously provided by Hunter and Harold [85] and Nicodemus et al. [129].

*The information presented in Section 2.1 also extends to the UV and IR portions of the electromagnetic spectrum.

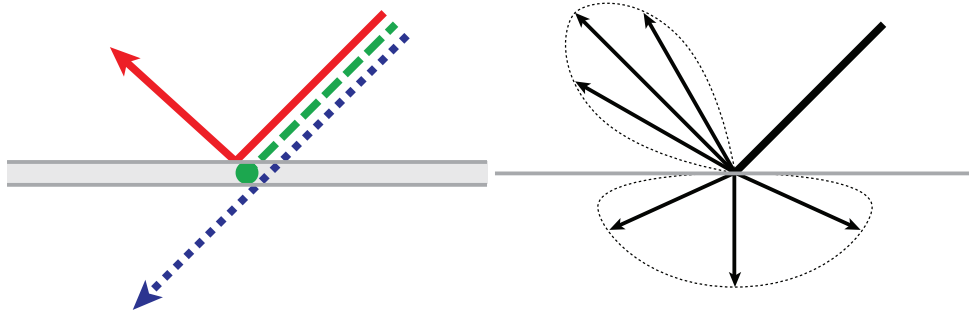


Figure 2.1: Diagram illustrating spectral (left) and spatial (right) distributions of propagated light. On the left, the light represented by the solid red, dashed green and dotted blue lines are reflected, absorbed and transmitted, respectively. On the right, the spatial distribution for the reflected light is more directionally oriented (specular) and more diffusely oriented for the transmitted light.

2.1.1 Spectral Distribution

The spectral distribution of light propagated by a material can be measured in terms of its reflectance and transmittance. Both of these wavelength-dependent quantities have three configurations for the incident and illumination geometries. These configurations are directional, conical and hemispherical. This results in nine permutations (*e.g.*, directional-hemispherical) of how reflectance and transmittance can be represented [129].

Reflectance can be defined as the ratio of the reflected flux to the incident flux for light. Similarly, transmittance can be defined as the ratio of the transmitted flux to the incident flux. Light that is neither reflected nor transmitted is absorbed. The fraction of incident flux that is absorbed is termed absorptance. Due to conservation of energy, the sum of a material's reflectance, transmittance and absorptance at a specific wavelength is equal to one. Note that, depending on the material's biophysical characteristics, measurements of these quantities performed at different wavelengths can vary considerably. For example, the reflectance and transmittance of green plant leaves in the visible spectral domain have their peaks in the 500 *nm* to 600 *nm* region of this domain, more precisely around 550 *nm* [10], which also corresponds to the peak sensitivity of the human visual system and it is directly associated with the human perception of the colour green [58].

2.1.2 Spatial Distribution

The spatial distribution of light propagated by a material can be measured by its bidirectional scattering-surface distribution function (BSSDF). This function can be decomposed into the reflected and transmitted components, namely the bidirectional scattering-surface reflectance distribution function (BSSRDF) and the bidirectional scattering-surface transmittance distribution function (BSSTDF) respectively [129].

The BSSDF is a difficult function to measure and compute due to its dependence on several parameters: the incoming and outgoing directions, the wavelength and the position on the surface. Therefore, a simplifying assumption is often used where the positional dependence is omitted. This results in the bidirectional scattering distribution function (BSDF) which, in turn, can be decomposed into the bidirectional reflectance distribution function (BRDF) and bidirectional transmittance distribution function (BTDF). Figure 2.2 illustrates the difference between a BSSRDF and its simplified BRDF counterpart. The BRDF can be formally defined using the following equation [129]:

$$f(\varphi_i, \varphi_p) = \frac{dL_p(\varphi_p)}{L_i(\varphi_i) d\omega_i \cos \theta_i}, \quad (2.1)$$

where dL_p is the radiance propagated in a direction φ_p , L_i is the radiance incident from a direction φ_i , θ_i is the polar angle (with respect to φ_i) and $d\omega_i$ is the differential solid angle at which L_i arrives. For a more in-depth understanding of these concepts, we refer the interested reader to the comprehensive text by Nicodemus et al. [129]. The BRDF is usually sufficient to describe opaque materials. However, light propagation from materials that are more translucent may have a significant subsurface scattering component. As such, the simulation of their BSSRDF is required to replicate their appearance (Figure 6.9). The spatial distribution may also be spectrally dependent since the materials' optical properties that affect the scattering of light (*e.g.*, refractive index) can vary with wavelength.



Figure 2.2: Diagram illustrating the difference between a BSSRDF (left) and the corresponding BRDF (right).

2.2 Modelling of Skin Appearance

Skin appearance models employed in realistic image synthesis can be broadly categorized into two groups: deterministic and nondeterministic. Deterministic models (*e.g.*, [50, 175, 202]) simulate the light and skin interactions using formulations based on analytical approximations to the radiative transfer equation such as the Kubelka-Munk theory, the diffusion theory and the discrete-ordinate approximation [18, 86]. Nondeterministic models (*e.g.*, [77, 104, 128]) simulate these interactions using stochastic techniques based on Monte Carlo methods [151].

Deterministic models are faster and amenable to analytical manipulation, which favours their use in real-time applications aimed at generating believable images of virtual characters. However, it is important to note that the predictive capabilities of these models are bound by the inherent limitations of the analytical approximations employed in their formulations. For example, it has been empirically demonstrated [33, 83] that the diffusion theory approximation fails to accurately describe light propagation in highly absorbing media. In the case of human skin, strong absorption is verified in the UV, visible (below $\approx 600 \text{ nm}$) and IR (above $\approx 1300 \text{ nm}$) domains [7]. Recently, algorithms have been proposed to relax the limitations of the diffusion theory approximation [46]. The evaluation of these algorithms, however, has been limited to comparisons with results provided by general-purpose Monte Carlo simulations [200] involving the reflectance and transmittance profiles within single and two-layer homogeneous materials.

Nondeterministic models allow for the proper modelling of complex geometries and optical inhomogeneities [83, 151, 200], thus supporting the utilization of first principles simulation approaches. These approaches, in turn, apply fundamental principles of physics to a material’s microscopic structure in order to build up the bulk behaviour of how it interacts with light [54]. Accordingly, depending on the level of abstraction employed in the characterization of the skin specimens, they can lead to high-fidelity results[†]. These models, however, are bound to incur higher processing times due to their use of Monte Carlo methods. For this reason, parallel processing strategies (*e.g.*, [105]) and specialized graphics hardware (*e.g.*, [52]) are often employed to improve their performance.

The existing skin appearance models, either deterministic or nondeterministic, are not designed for providing predictive spectral responses with respect to a broader spectral domain, from UV to IR. For instance, different studies have shown [7, 131] that the effects of melanin on skin colour and UV light attenuation must be related not only to melanin content, but also to where it is found and how it is dispersed within the cutaneous tissues. None of the existing skin appearance models account for the particle nature and distribution of melanosomes within the different epidermal layers, which impairs their predictive capabilities even in the

[†]Fidelity refers to “the accuracy of the representation when compared to the real world” [72].

visible domain as further discussed in Chapter 6. In addition, to the best of our knowledge, the existing models do not account for the presence and distribution of other major contributors to light attenuation outside the visible domain such as keratin, DNA, urocanic acid, water and lipids [208, 211].

It is worth mentioning that there have been relevant computer graphics works involving the measurement of skin spectral responses and the capture of skin appearance data (*e.g.*, [51, 61, 65, 116, 202]). These efforts, however, were likewise aimed at applications in the visible domain. Consequently, they primarily targeted the acquisition of skin appearance data in this region of the light spectrum.

There is also a considerable amount of research on the simulation of light and skin interactions being performed in fields as diverse as colorimetry (*e.g.*, [189]), remote sensing (*e.g.*, [133]) and tissue optics (*e.g.*, [151]). We remark, however, that the models proposed in these fields are not designed for the comprehensive simulation of material appearance within image synthesis frameworks, which involves both the spectral and spatial distributions of light interacting with a given material [85]. Instead, these models are primarily designed for specialized applications such as the detection and analysis of skin spectral signatures within specific regions of the light spectrum (*e.g.*, [130]).

2.3 Modelling of Material Appearance Changes

In order to achieve a high degree of realism in digital scenes, a substantial amount of computer graphics research has been devoted to the modelling of material appearance [54], with a portion of these efforts being directed toward the simulation of material appearance variations caused by environmental factors [119]. For example, Dorsey et al. [53] and Chen et al. [37] simulated the appearance of weathering by modelling surface erosion using small particles. Kimmel et al. [99] developed a framework to simulate appearance changes due to light exposure by incorporating a time component to the Kubelka-Munk theory [106]. These methods, however, are less suitable to living materials that may actively respond to environmental stimuli.

There are works, however, that specifically account for appearance variations in living materials. For example, Pamplona et al. [140] presented a physiologically-based model that simulates changes in the eye's pupil due to ambient lighting conditions. In the case of human skin, there have been relevant investigations depicting short term appearance changes due to factors such as variations in dermal blood parameters (*e.g.*, [51, 95, 104]), as well as long term appearance changes due to aging related processes (*e.g.*, [25, 87]). However, these works do not directly address the connections between the external stimuli and the corresponding

time-dependent physiological reactions. As an example of such a connection with respect to tanning, one can consider the redistribution and degradation of melanin [181]. These physiological reactions may vary according to the duration, intensity and spectral distribution of the light stimuli [66, 123], contributing to skin appearance changes (Figure 2.3) proportional to the specimen's native level of adaptation to UVR exposure [161].



Figure 2.3: Photograph series showing changes in pigmentation over time as a result of a controlled tanning experiment using distinct UVR exposure doses [122]. Left: initial state. Centre: emerging responses. Right: peak responses. The three patches of darkened skin correspond to different exposure doses, and the fourth patch (on the lower right of centre and right images) represents the unexposed control area. Note that areas on the left side of the back (leftmost photo) show results from previous experiments on skin sensitivity to UVR exposure. Courtesy of S. Miller [122]. Original image copyright by John Wiley & Sons, Inc.

Another approach used in this area consists in capturing the appearance attributes of materials as they change over time. Different techniques can then be used to organize, store and apply the acquired information in digital scenes (*e.g.*, [73, 190, 199]). However, besides being bound by logistic conditions and equipment costs, the implementation of this approach is limited to situations where such information is available to be captured.

At the present, to the best of our knowledge, the physiologically-based simulation and visualization of temporal variations in human skin appearance has not been addressed in the computer graphics literature. Although a mathematical formulation for tanning related processes has been proposed in the biomedical field [184, 185], it is worth noting that it focuses on a specific tanning mechanism, notably melanin production. For example, the UV sensitivity of different skin types [141, 149, 161] and the hyperplasia process that may accompany the increase in skin pigmentation [112, 145] are not accounted for in this formulation. Moreover, it is not designed for applications aimed at the visualization of changes in skin appearance attributes.

3 Skin Biophysical Background

In order to predictively model light and skin interactions, it is necessary to account for the intrinsic bio-optical properties of this complex organic material. Although previous works in this area have examined these properties, for completeness, we review them from hyperspectral and photobiological perspectives in this chapter.

Human skin is usually described as being composed of three distinct tissues, namely stratum corneum, epidermis and dermis [208]. The stratum corneum and the epidermal layers (stratum lucidum, stratum granulosum, stratum spinosum and stratum basale, from the outermost to the innermost) are composed of stratified cells with a combined thickness that may reach about 1 *mm* [7, 44]. Note that the stratum lucidum is a clear layer found only in thick skin regions such as palms and soles [44]. For these reasons, it is not further addressed in this work. The dermis can be divided into the outermost papillary dermis and innermost reticular dermis, with a combined thickness that may reach up to 4 *mm* [7]. Compared to the reticular dermis, the papillary dermis is relatively thin and contains smaller-sized structural fibres. The dermis also contains a network of blood vessels, with wider vessels being located in the reticular dermis.

Light impinging on the skin surface can be reflected back to the environment or transmitted into its internal tissues [7], a process that can be described in terms of the Fresnel equations*. Once light is transmitted into the skin tissues, it can be absorbed or scattered by their constituent materials. We outline the most important of these attenuation agents contributing to light absorption (Section 3.1) and scattering (Section 3.2) within the cutaneous tissues in the UV, visible and IR domains. We also discuss the implications of detour and sieve effects (Section 3.3) for the propagation and absorption of light within the cutaneous tissues. Finally, we will examine relevant physiological changes that take place in skin (Section 3.4) when it is exposed to sufficient UVR.

*These equations describe how light behaves when moving between materials with different refractive indices [18].

3.1 Light Absorbing Materials

Relevant light absorbing materials acting in the UV domain are situated within the stratum corneum and epidermis [211]. These include DNA, keratin, urocanic acid and melanin, which may occur in two forms within human skin: the dominant brown-black eumelanin and the yellow-red pheomelanin [32].

Melanin is also a strong absorber in the visible range [7]. It is synthesized by melanocyte cells in the stratum basale, where it is preferentially concentrated [44]. As the epidermal cells move upward, it is distributed throughout the full thickness of the upper layers [103]. Melanin may occur in a colloidal form (also known as “melanin dust”) or clustered within the melanosomes [143], where its content may range from 17.9% to 72.3% [103].

Blood-borne pigments (*e.g.*, oxyhemoglobin, deoxyhemoglobin, carboxyhemoglobin, methemoglobin, sulfhemoglobin, bilirubin and beta-carotene) found in the dermis are also relevant absorbers in the UV and visible domains [94]. It is worth noting that beta-carotene may be also found in the epidermis and stratum corneum [7]. Water and lipids found throughout the skin dominate the absorption of light in the IR domain [41, 93], notably within the thick dermis [208].

3.2 Light Scattering Materials

Light is mostly scattered by heterogeneous structures, such as cells, organelles and fibres, found within the skin tissues [7]. Among these structures, the melanosomes, which predominantly scatter light in the forward direction [32], have a central role in the attenuation of UV and visible light [103]. The quantity of melanosomes produced in human skin is determined by genetic factors and sun exposure. In darkly pigmented specimens, the mean epidermal melanosome content (volume fraction) may be as high as 10%, while in lightly pigmented specimens, it may be as low as 1% [110].

Melanosomes can be described as particles with the shape of a prolate spheroid [136]. In lightly pigmented specimens, they can occur in groups surrounded by a transparent membrane forming melanosome complexes [136, 180], which are characterized to be approximately spherical in shape [103, 180] (Figure 3.1 (left and centre)). In darkly pigmented specimens, however, they occur as denser and individually dispersed particles [136, 180] (Figure 3.1 (right)).

The turbid dermal layers contain dense connective tissue. Light traversing these layers is subject to Rayleigh scattering, which may be caused by the presence of small scale features,

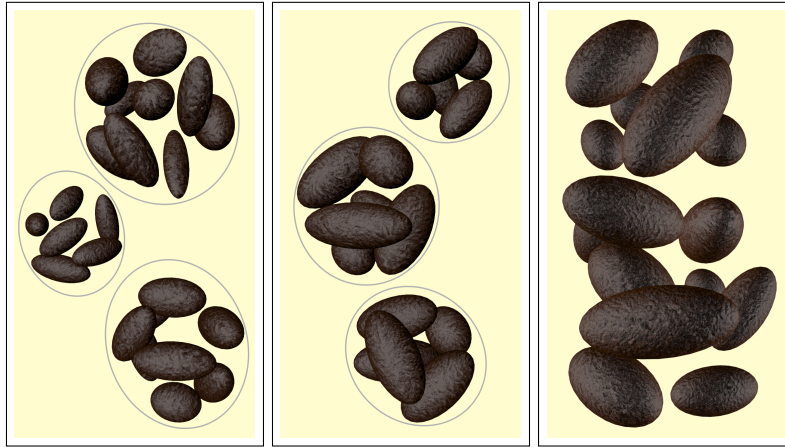


Figure 3.1: Sketches depicting the distribution of melanosomes within the epidermal layers of skin specimens with different levels of melanin pigmentation. Left: melanosome complexes found in lightly pigmented specimens. Centre: more compact complexes found in moderately pigmented specimens. Right: individually dispersed melanosomes found in darkly pigmented specimens.

such as collagen fibres and fibrils, in the papillary dermis [7, 90]. Moreover, as light penetrates deeper into the dermal layers, it becomes progressively more diffuse [92]. Eventually, the light traversing the dermis may reach the hypodermis. Light remission by large cellular structures in this adipose tissue can further contribute to increase the scattering of light within the dermis [208].

3.3 Detour and Sieve Effects

When light traverses a turbid medium, refractive index differences between pigment-containing structures and the surrounding medium may cause multiple interactions that increase the light optical pathlength, a phenomenon known as detour effect [29] (Figure 3.2 (left)). Conversely, the traversing light may undergo a sieve effect, *i.e.*, it may not encounter a pigment-containing structure [107] (Figure 3.2 (right)). While the former increases the probability of light absorption by the pigment of interest, notably in bands of absorption minima, in comparison with a homogeneous solution with equal concentration of this pigment [29], the latter reduces the probability of light absorption, particularly in bands of absorption maxima [107]. The net result of these effects depends on the absorption spectra of the pigments as well as the distribution and volume fraction of the pigment-containing structures (*e.g.*, melanosomes and melanosome complexes) found in a given medium [29, 107].

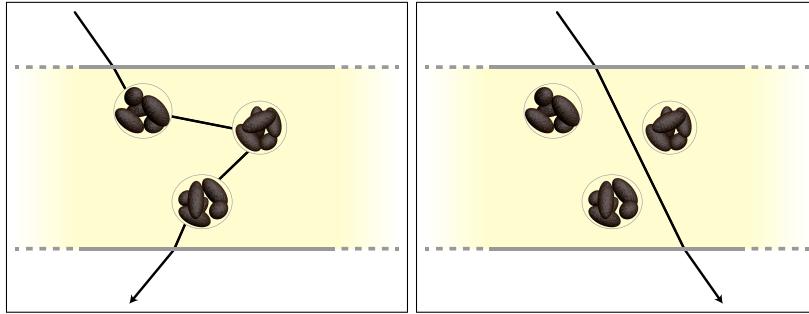


Figure 3.2: Diagram illustrating detour (left) and sieve (right) effects that may take place when light traverses an epidermal layer containing melanosome complexes. The same phenomena may take place in a layer occupied by individually dispersed melanosomes.

3.4 Skin Photobiological Phenomena

The two most visible skin responses to excessive UVR exposure are erythema (commonly known as “sunburn”) and tanning [80]. The former results from a vasodilation of the dermal blood vessels [39], which, in turn, leads to a skin reddening at the stimulus site. It is worth noting that this chromatic variation can also be triggered by mechanical, chemical, electrical and thermal stimuli [1], and it has been reproduced in several computer graphics works (e.g., [51, 95, 104, 190]). Compared to tanning, however, erythema can be considered a fleeting phenomenon [80]. Furthermore, the occurrence of erythema, notably in individuals with low tanning ability [143], is often associated with blistering and peeling. The correct reproduction of such extreme morphological changes would require alterations in the skin structure, which are beyond the scope of this work. For these reasons, erythema is further addressed in this thesis only when referring to specific physical quantities employed in the simulation of tanning dynamics.

The photobiology of the melanin pigmentary system involves several processes [26, 123]. The most relevant of these processes, known as delayed tanning, is responsible for the familiar long-lasting tan induced by UVR exposure [80], the focal point of this work. The effects of this phenomenon, henceforth referred to as the tanning process, are usually visible about 24 hours after sufficient UVR exposure, and they can last anywhere from days to more than a year [80].

The tanning process is characterized by an increase in the pigmentation level, or melanin content, of the skin. Melanin, the main light attenuation substance acting in the UV and visible spectral domains, is typically located within the epidermal layers of the skin in a colloidal form or encapsulated within the melanosomes [80] (Section 3.1). It is important to remark that the perceived level of skin pigmentation of an individual depends not only on the amount

of melanin found in the epidermal tissues, but also on how it is distributed within these tissues [66, 80, 123] (Section 3.3).

Melanin is synthesized, through a phenomenon termed melanogenesis, by cells known as melanocytes, which are mostly concentrated in the innermost epidermal layers (Figure 3.3 (left)) [66]. Melanin is spread throughout the full thickness of the epidermis as the skin cells migrate upwards towards the surface (Figure 3.3 (right)) [103]. During tanning, there is an increase in the number and activity of melanocytes [26]. This increase in melanin content is known as facultative pigmentation, while the original baseline (induced by genetic factors) pigmentation level is known as constitutive pigmentation [80]. This process also shifts the distribution of melanin within the epidermal layers [181]. Additionally, the thickness of the various skin tissues is subject to change [80, 112].

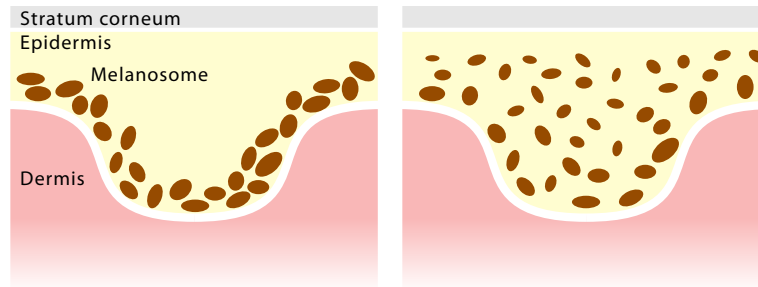


Figure 3.3: Sketches illustrating the distribution of melanin originally produced in the innermost epidermal layers. Left: initially the melanin encapsulated in the melanosomes is predominantly located within these layers. Right: as the epidermal cells migrate upwards, melanin is distributed throughout the epidermis.

The level of adaptation to UVR exposure varies among distinct skin specimens, and it has been used to establish the Fitzpatrick skin phototype (SPT) classification [143]. According to this classification, among specimens with a low constitutive pigmentation level, there are those that cannot tan (SPT I), and those that have this ability in different degrees (SPT II, III and IV). In addition, specimens characterized by an intermediate or high constitutive pigmentation level (SPT V and VI respectively) are all capable of tanning profusely and rarely affected by erythema [143]. Although this classification can be used to qualitatively describe the typical tanning responses of different skin specimens, it has been pointed out that there is no clear quantitative relationship between skin phototype and UV sensitivity [205].

More recently, Ravnbak et al. [161] quantitatively related skin pigmentation to the minimum erythema dose (MED) and minimum melanogenesis dose (MMD)[†]. These two quantities

[†]Although the MED and MMD of a given skin specimen can be estimated using the provided formulae (Equa-

are defined as the minimum amount of radiant energy per unit area necessary to produce a visually perceptible erythema and tanning response respectively [158]. These quantities are measured in terms of J/m^2 , and have been referred to as optical energy density [176], radiant exposure [88] or exposure dose [5, 141]. We employ the last-cited term throughout this document for consistency with related work. The relationships reported by Ravnbak et al. [160] are given below:

$$MED_{SED} = 2.1973 \cdot \exp(7.4043 \cdot p) \quad (3.1)$$

$$MMD_{SED} = 4.3132 \cdot \exp(5.1295 \cdot p), \quad (3.2)$$

where p is the pigmentation level[‡]. We note that these formulae provide MED and MMD values in terms of the standard erythema dose (SED). A unit of SED (employed as a reference in tanning experiments [161]) is defined as $100 J/m^2$ at $298 nm$ [159].

The study and analysis of a given photobiological phenomenon often requires the knowledge about the action spectrum of the physiological processes associated with this phenomenon. This quantity refers to the effectiveness of different wavelengths of light in triggering such processes [141]. In this thesis, we take into account the action spectra of melanogenesis and erythema (Figure 3.4). While the former is employed in computations involving melanin production (Section 5.1.1), the latter is used in computations associated with the regulation of skin thickness (Section 5.2.1).

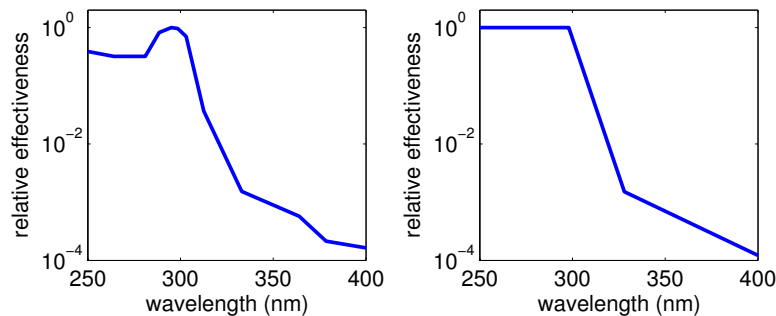


Figure 3.4: Action spectra of melanogenesis [141] (left) and erythema [118] (right).

tions 3.1 and 3.2 respectively) given its pigmentation content, if these quantities are measured through physical experiments, then one can instead use their measured values directly.

[‡]In the original formulations provided by Ravnbak et al. [160], the pigmentation level is given in terms of normalized percentages ranging from 0% to 100%. The values used in this thesis range from 1.3% to 43%, which correspond to the epidermal volume fraction occupied by melanin [90].

4 HyLloS Model Description

The proposed hyperspectral model employs stochastic techniques to simulate the interactions of light with human skin. Using a first principles approach, it accounts for the physical distances traveled by light within the cutaneous tissues. As a result, the radiometric responses derived from the light interaction processes affecting skin appearance can be quantified in terms of BSSRDF since the distances that may separate the light incidence (x_{i_1} to x_{i_4}) and outgoing (x_{o_3} and x_{o_4}) points (Figure 4.1) are provided by the simulations. Alternatively, these radiometric responses can be quantified in terms of BRDF by ignoring this positional parameter (Section 2.1.2).

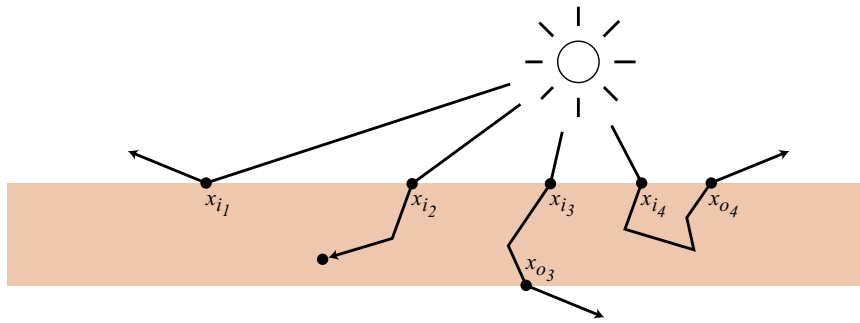


Figure 4.1: Sketch illustrating the different light and skin interaction processes simulated by the proposed hyperspectral model (HyLloS). From left to right: surface reflection, absorption, transmission and subsurface reflection. Note that the distances that may separate light incidence (x_{i_1} to x_{i_4}) and outgoing (x_{o_3} and x_{o_4}) points are computed taking into account the physical distances that light travels within the cutaneous tissues.

Within the model, the main cutaneous tissues, namely stratum corneum, stratum granulosum, stratum spinosum, stratum basale, papillary dermis and reticular dermis, are represented by semi-infinite layers as depicted in Figure 4.2. These layers are characterized by their thickness, refractive index as well as the presence and optical properties of light attenuation materials.

Stratum corneum		UV
Epidermis	Stratum granulosum	UV-Vis
	Stratum spinosum	UV-Vis
	Stratum basale	UV-Vis
Dermis	Papillary dermis	Vis-IR
	Reticular dermis	Vis-IR

Figure 4.2: Diagram showing the skin layers considered by the HyLloS model. The main light-absorbing spectral domains associated with each layer are identified as UV (ultraviolet), Vis (visible) and IR (infrared).

The propagation and attenuation of light within the various skin layers are simulated through an iterative random walk algorithm which is schematically presented in Figure 4.3. Within this formulation, absorbers represent materials that primarily absorb light, while attenuators represent materials that primarily scatter light (*e.g.*, connective fibres) as well as materials that significantly contribute to both absorption and scattering of light (*e.g.*, melanosomes). Light is represented by discrete rays, each one associated with a given wavelength λ , and the attenuation events are probabilistically accounted for using ray optics and, when appropriate, data-driven procedures based on wave optics observations (Sections 4.2 and 4.3).

At the start of each iteration, a Fresnel test* is performed when a ray hits a layer interface. If the ray exits the skin, a reflection or transmission event is recorded, and the iteration is terminated. Otherwise, the distance to the next attenuation event is probabilistically computed as follows. When a ray travels through a layer, it may interact with various absorbers and attenuators. Each of these tissue constituents may be associated with a different spectral attenuation coefficient $\mu(\lambda)$. For each relevant $\mu(\lambda)$, we generate a distance $D(\lambda)$ [151] given by:

$$D(\lambda) = -\frac{1}{\mu(\lambda)} \ln \xi_1, \quad (4.1)$$

where ξ_1 is a random number uniformly generated from $[0, 1)$. The actual distance travelled by the ray to the next attenuation event corresponds to the smallest of these generated distances, *i.e.*, we advance the ray by this distance. If the ray hits a layer interface, the process reiterates

*Each time a ray hits an interface between two materials, a Fresnel coefficient is computed using the Fresnel equations [18]. This coefficient is compared to a random number uniformly sampled on the fly from $[0, 1)$. If the random number is smaller than the coefficient, then a reflected ray is generated. Otherwise, a transmitted ray is generated.

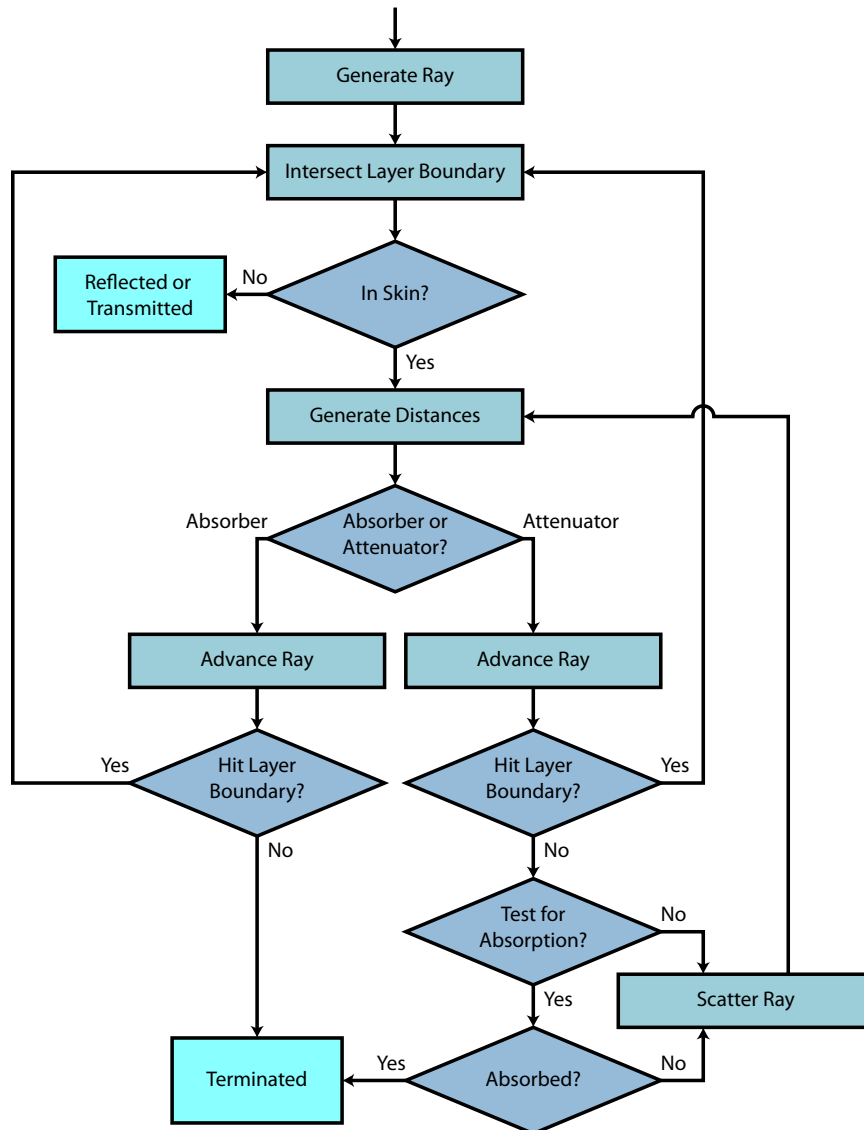


Figure 4.3: Flowchart depicting the general structure of the iterative random walk algorithm employed by HyLloS. The distances to the next attenuation events are computed using Equation 4.1.

from the Fresnel test. Otherwise, three possible outcomes may take place (Figure 4.3). In the case of absorbers, the ray is terminated. In the case of attenuators that can significantly contribute to both absorption and scattering, a probabilistic test (Section 4.2.1) is used to determine whether the ray is absorbed. If the test fails, the ray is scattered (Section 4.2.1) and the random walk continues. Otherwise, the ray is terminated. In the case of attenuators that primarily scatter light, the ray is scattered (Section 4.2.2) and the random walk proceeds.

In the following sections, we describe how the light attenuation contributions of absorbers, attenuators and large scale cellular structures are accounted for in the algorithmic formulation of the model.

4.1 Absorbers

In order to account for the contributions of the absorbers present in a given layer, we compute the spectral volumetric absorption coefficient associated with that layer, which corresponds to the weighted sum of the specific spectral absorption coefficients of each absorber. For example, the absorption in the papillary dermis is primarily due to water, lipids and blood pigments. Let the blood borne pigments oxyhemoglobin, deoxyhemoglobin, carboxyhemoglobin, methemoglobin, sulfhemoglobin, beta-carotene and bilirubin be denoted by oh , dh , ch , mh , sh , bc and bil , respectively. The corresponding volumetric absorption coefficient of the papillary dermis can then be calculated as:

$$\begin{aligned} \mu_a^p(\lambda) = & \zeta_{water}(\lambda)v_{water}^p + \zeta_{lipids}(\lambda)v_{lipids}^p + \\ & [\zeta_{oh}(\lambda)v_{oh}^b + \zeta_{dh}(\lambda)v_{dh}^b + \zeta_{ch}(\lambda)v_{sh}^b + \\ & \zeta_{mh}(\lambda)v_{mh}^b + \zeta_{sh}(\lambda)v_{sh}^b + \\ & \zeta_{bc}(\lambda)v_{bc}^b + \zeta_{bil}(\lambda)v_{bil}^b]v_{blood}^p, \end{aligned} \quad (4.2)$$

where ζ_i , v_i^p and v_i^b correspond, respectively, to the specific absorption coefficient of a given absorber i , its volume fraction within the papillary dermis and its volume fraction within whole blood.

Recall that melanin may be found dispersed in a colloidal form or clustered within the melanosomes (Section 3.1). In the former case, its specific absorption coefficients (for eumelanin and pheomelanin) are aggregated to the specific absorption coefficients of the pigments found in a given layer as described above. In the latter case, the computation of its attenuation coefficient takes into account its concentration within each individual melanosome. This coefficient is then employed in the absorption tests performed considering the specific geometrical and

optical characteristics of these melanin-containing organelles (Section 4.2.1).

For completeness, the biophysical constants and formulae used to compute the spectral absorption coefficients considered in this thesis are provided in Appendix A along with the absorption spectra (Figure A.1) of the main absorbers found in the cutaneous tissues.

4.2 Attenuators

Melanosomes and connective fibres are incorporated into the model as attenuators. Based on experimental investigations [107], the perturbations caused by these materials on the propagated light is assumed to be azimuthally symmetric. Accordingly, the corresponding azimuthal angle of perturbation is uniformly sampled from $[0, 2\pi)$.

4.2.1 Melanosomes and Melanosome Complexes

Individually dispersed melanosomes (in darkly pigmented specimens) and melanosome complexes (in lightly and moderately pigmented specimens) are probabilistically generated, positioned and oriented on the fly in a given epidermal layer (Figure 4.4). This approach enables the simulation of light interactions with each melanosome without having to explicitly store these organelles as well as avoiding expensive ray-melanosome intersection tests.

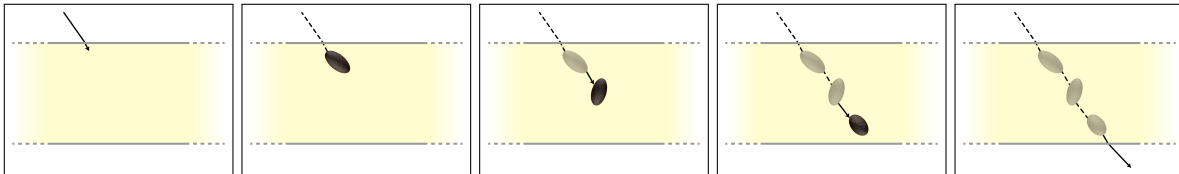


Figure 4.4: Diagram illustrating a possible path (from left to right) that can be followed by a ray traversing an epidermal layer occupied by individual melanosomes (represented by prolate spheroids). The distance to the next melanosome is probabilistically computed according to a pathlength distribution. The orientation of the melanosome and the hitting point on its surface are also probabilistically generated. The light interaction with the melanosome is simulated, and the ray is either terminated inside the melanosome or scattered. In the latter case, the melanosome is discarded and a new one is generated. This process is repeated until the ray is either absorbed or scattered outside of the layer. The same stochastic procedure is employed for melanosome complexes.

Melanosomes are modelled as prolate spheroids employing dimensions reported in the literature [136], while melanosome complexes are modelled as spheres [103]. Based on experimental observations [180], for lightly pigmented specimens, the sphere diameter is set to be

twice the major axis of the spheroids representing the encapsulated melanosomes. Similarly, for moderately pigmented specimens, this diameter is set to be equal to the major axis of the spheroids [180].

The attenuation coefficient of a melanosome is given by its geometric attenuation coefficient [100]:

$$\mu_g = \frac{S v}{V 4}, \quad (4.3)$$

where S is the surface area, V is the volume and v is the volume fraction. The ratio S/V for a prolate spheroid is calculated as:

$$\frac{S}{V} = \frac{3}{2a} \left(\frac{a}{b} + \frac{\arcsin c}{c} \right), \quad (4.4)$$

where a and b correspond to the lengths of the semi-minor and semi-major axes respectively, and $c = \sqrt{(1 - a^2/b^2)}$.

Once the distance D is computed by substituting μ_g into Equation 4.1, the orientation of the prolate spheroid is selected by sampling the probability distribution functions (PDFs) associated with the orientation that was considered while generating the distance. These PDFs [210] are given by:

$$P_m(\alpha) = \frac{\chi_1(1 - |\cos \alpha|) + \chi_2|\cos \alpha|}{\chi_1 + \chi_2}, \quad (4.5)$$

$$P_m(\beta) = \frac{1}{2\pi}, \quad (4.6)$$

where α and β correspond, respectively, to the polar and azimuthal angles defining the ray direction, and χ_1 and χ_2 correspond to the cross-sectional areas of the spheroid associated with its minor and major axes respectively. Note that if the spheroid overlaps its predecessor, it is rejected and another one is generated. Similarly, the spheroid is also rejected if it crosses a layer boundary. Finally, the hitting point on the spheroid surface is randomly selected among the set of points facing the ray, *i.e.*, by uniformly selecting a random point from the spheroid's projected surface facing the ray.

After the position, orientation and hitting point are selected, the model simulates the light-melanosome interactions taking into account the dual photon-wave nature of these interactions. As observed by Latimer [107], when light traverses an organelle, the light waves tend to reach out and interact with parts of the organelle which are geometrically outside their straight line path, resulting in an absorption enhancement. In order to account for this absorption enhancement, the ray traversing the melanosome is tested for absorption considering the possibility of multiple internal interactions as described next. The distance that the ray can travel

until the next attenuation event is computed employing Equation 4.1 and using the aggregated specific absorption coefficients of eumelanin and pheomelanin as the corresponding attenuation coefficient (Section 4.1). If this distance does not allow the ray to exit the melanosome, the ray is terminated. Otherwise, a Fresnel test is performed to determine whether the ray is either transmitted out or reflected back to the interior of the spheroid due to the refractive index difference between the clustered melanin and the surrounding medium (epidermal tissue). In the latter case, the ray is diffusely perturbed to account for the irregular morphology of the different melanosome parts [103] subjected to the light-organelle interactions [107] mentioned earlier. Accordingly, the polar perturbation angle is sampled from $[0, \pi/2)$ using a PDF based on the cosine distribution [18], *i.e.*, the polar perturbation angle is given by $\arccos(\sqrt{1 - \xi_2})$, where ξ_2 represents a random number uniformly sampled from $[0,1)$. Rejection sampling [76] is employed to guarantee that the perturbed ray, denoted by \vec{r}_p , remains inside the melanosome, *i.e.*, if $\vec{r}_p \cdot \vec{n} < 0$, where \vec{n} corresponds to the inward normal at the intersection point, the ray is rejected. In this case, another perturbed ray is obtained and the rejection test is repeated. After applying this perturbation procedure, the process inside the melanosome reiterates from the absorption test.

In the case of the melanosome complexes, their attenuation coefficient is also obtained using Equation 4.3, with the ratio S/V given by $3/r_s$ [100], where r_s is the radius of the corresponding sphere. When a ray encounters a melanosome complex, it interacts with at most n_m encapsulated melanosomes, where n_m corresponds to the ratio of the diameter of the encapsulating sphere to the minor axis of the spheroid representing the melanosomes [180]. Each of these interactions will involve the melanosome orientation selection and the absorption test described above.

If a ray is not absorbed by an individually dispersed melanosome or a melanosome complex, it is scattered. The forward scattering behaviour of the melanosomes [32] is simulated using a data-driven procedure that also follows the dual photon-wave nature of the light-organelle interactions [107] mentioned earlier. More specifically, the corresponding polar scattering angle θ_m is sampled from an exponential distribution that has a mean angle θ_o . This mean angle was selected to be 5° based on wave optics experimental observations on the scattering behaviour of pigment-containing organelles [107]. Furthermore, since light-melanosome interactions have an increasingly diminished contribution to light attenuation from 780 nm to 1300 nm , being essentially negligible beyond $\approx 1400 \text{ nm}$ [7], we linearly reduce θ_o to 0 over this region. Accordingly, the polar angle θ_m is generated using Algorithm 1, where ξ_3 and ξ_4 are random numbers uniformly sampled from $[0, 1)$. Similarly, in the case of a melanosome complex, Algorithm 1 is applied if all encapsulated melanosomes fail the absorption test.

Algorithm 1 Exponential perturbation (mean angle θ_o)

$\phi = \arctan(\theta_o)$
 $max = (1/\theta_o) \exp(-\phi/\theta_o) \sin(\phi)$
repeat
 $\xi_3, \xi_4 = \text{random}[0, 1)$
 $\theta_m = \pi \xi_3$
until $max \xi_4 \leq (1/\theta_o) \exp(-\theta_m/\theta_o) \sin(\theta_m)$
return θ_m

4.2.2 Connective Fibres

It has been proposed [90] that the scattering caused by the thin connective fibres in the papillary dermis follows the Rayleigh scattering formulation. Hence, the attenuation coefficient associated with these fibres is calculated using the following expression [117] for the Rayleigh scattering coefficient:

$$\mu_s^R(\lambda) = \frac{128\pi^5 r^6 v_f}{3\lambda^4} \left(\frac{4}{3}\pi r^3\right)^{-1} \left(\frac{\eta^2 - 1}{\eta^2 + 1}\right)^2, \quad (4.7)$$

where r and v_f represent the radius and the volume fraction occupied by the connective fibres, respectively, and η corresponds to the ratio between the refractive index of these scatterers to the refractive index of their surrounding medium (papillary dermis). Based on data provided by Jacques [90], we consider $r = 100 \text{ nm}$, $\eta = 1.127^\dagger$, and $v_f = 0.22$ as default values in our simulations.

The ray direction of propagation is perturbed considering the Rayleigh scattering distribution [117]. Accordingly, the polar angle θ_R is generated using Algorithm 2, where ξ_5 and ξ_6 are random numbers uniformly sampled from $[0, 1)$. Since the attenuation coefficient computed for these materials describes bulk scattering, the contributions of these attenuators are taken into account only once per ray pass through the papillary dermis.

[†]Note that this value suggested by Jacques [90] was based on empirical approximations to the relevant refractive indices. Hence, it may be subjected to change as more accurate values for these refractive indices become available.

Algorithm 2 Rayleigh perturbation

```
repeat  
     $\xi_5, \xi_6 = \text{random}[0, 1)$   
     $\theta_R = \pi \xi_5$   
until  $\xi_6 \leq \left(\frac{3\sqrt{6}}{8}\right) (1 + \cos^2 \theta_R) \sin \theta_R$   
return  $\theta_R$ 
```

4.3 Large Scale Cellular Structures

A portion of the light that interacts with the skin surface (stratum corneum) cells may be reflected back to the environment following the execution of a Fresnel test [7]. To account for the influence of the skin surface roughness on the distribution of the reflected rays, the surface normals are perturbed using a procedure based on the Trowbridge-Reitz function [188], which represents rough air-cell interfaces using randomly-curved microareas. Accordingly, when a ray impinges on the skin surface, the azimuthal angle of the perturbed surface normal is uniformly sampled from $[0, 2\pi)$, while the polar angle θ_s is generated using the following distribution:

$$P_s(\theta_s) = \frac{s^4}{(s^2 \cos^2 \theta_s + \sin^2 \theta_s)^2} \sin \theta_s, \quad (4.8)$$

where s is the roughness parameter associated with the aspect ratio of the stratum corneum cells, *i.e.*, the flatter the cells (lower s), the closer the spatial distribution of reflected rays approaches a specular distribution. We note that Equation 4.8 has been adapted from the original formulation describing the Trowbridge-Reitz function [188].

Since the large cellular structures found in the hypodermis reflect most of the impinging light (Section 3.2), the dermal–hypodermal junction is set to have a reflectance equal to one. In addition, considering that light becomes progressively more diffuse as it travels further within the dermis [92], the rays reflected at the dermal–hypodermal junction are diffusely perturbed, *i.e.*, the azimuthal perturbation angle is uniformly sampled from $[0, 2\pi)$ and the polar perturbation angle is sampled from $[0, \pi/2)$ using the PDF based on the cosine distribution previously provided (Section 4.2.1).

5 Tanning Simulation Framework Description

The proposed framework for the physiologically-based simulation of skin tanning dynamics, schematically presented in Figure 5.1, takes as input the UVR exposure dose and the initial values for the biophysical parameters that characterize a given skin specimen. These input values are used to calculate the changes in the skin biophysical parameters affected by the tanning mechanisms responsible for time-dependent variations in melanin pigmentation and epidermal thickness. The simulations of these mechanisms are performed within the two main algorithmic components of the framework, referred to as melanin dynamics and tanning dynamics, which are described in Sections 5.1 and 5.2 respectively. The discrete time-stepping approach employed in these simulations can account for single or multiple exposure doses of different intensities, as well as arbitrary illumination geometries. The updated parameter values resulting from the simulations are then used as input into the light interaction model to output the modified skin appearance attributes in terms of spectral reflectance and BSSRDF. We also note that, unless otherwise stated, the formulae presented in this chapter were originally derived for the simulations described in this thesis.

5.1 Melanin Dynamics

In this section, we describe the component of the framework that simulates the changes in melanin content and distribution. The algorithms and methods used within this section are based on the current understanding of the skin facultative pigmentation process [26, 160, 181, 184]. It is also important to note that the two forms of melanin found in the skin tissues, namely eumelanin and pheomelanin, are treated the same way during the melanin dynamics simulations since their proportions are known to remain relatively constant following UVR exposure [82, 123]. However, their proportions within the cutaneous tissues are accounted for in the computation of the resulting skin appearance attributes (Section 5.3). In addition, for consistency with related literature, the volume fraction, or percentage, of a given layer occupied by melanin is expressed in terms of melanin content, and denoted by m . Similarly, the relative

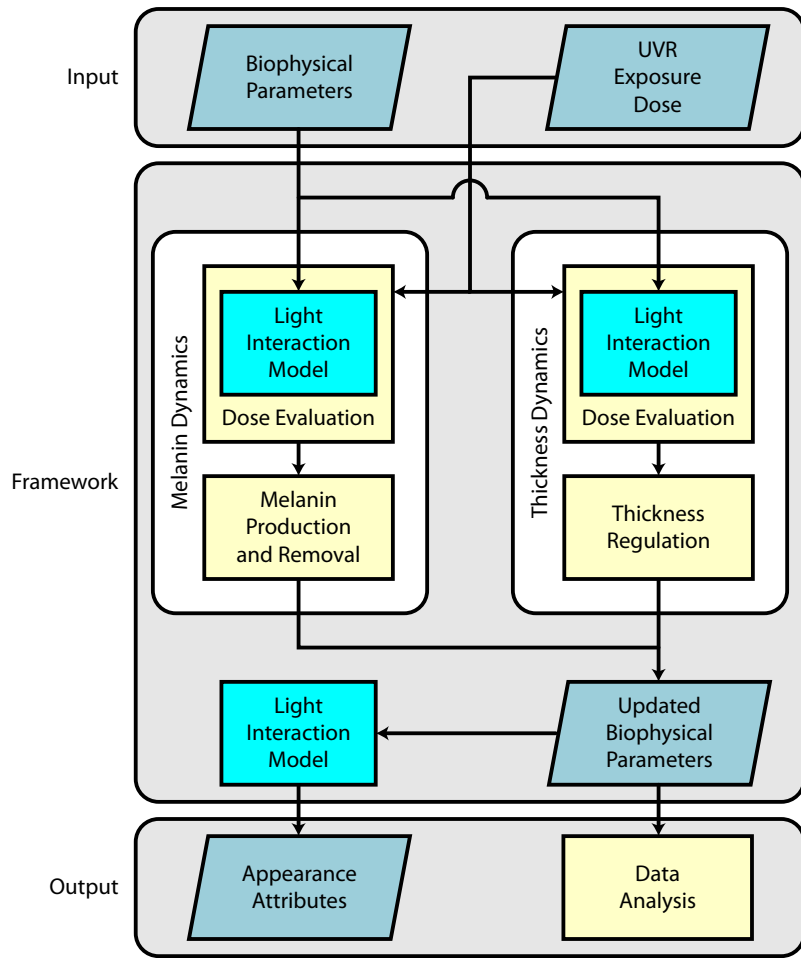


Figure 5.1: Diagram depicting the main modules of the proposed framework for the simulation and visualization of skin tanning dynamics. Note that it employs a light interaction model, HyLloS (Chapter 4), to evaluate whether the dose of UVR impinging on a skin specimen is sufficient to trigger the stimulation of melanin production and skin thickening. This model is also used to translate the results from the tanning dynamics simulations to skin appearance attributes.

amount of melanin found in a given epidermal layer with respect to the total amount of melanin found in all epidermal layers is expressed in terms of relative melanin content, and denoted by \hat{m} .

5.1.1 UVR Dose Evaluation

Initially, we need to determine the minimum UVR threshold at which the melanogenesis process is activated for a skin specimen. This quantity, henceforth referred to as the minimum melanogenesis threshold (MMT), is evaluated using the following expression:

$$\Psi_{\circ} = \int_{\lambda} \alpha_m(\lambda) \psi_{\circ}(\lambda) A(\lambda) d\lambda, \quad (5.1)$$

where α_m is the melanogenesis action spectrum (MAS), ψ_{\circ} is the MMD as a function of its component wavelengths (spectral MMD) and $A(\lambda)$ is the spectral absorptance of the skin specimen. The MAS is plotted in Figure 3.4 (left) and the spectral absorptance is computed using the proposed HyLloS model (Chapter 4).

Since the amount of absorbed UVR [26,66,123] is markedly affected by the content, concentration and distribution of melanin within the various epidermal layers, it is necessary to use a light interaction model that can account for the particle nature of these attenuation agents and can provide predictive results in the UV region of the light spectrum. As we stated earlier, the absence of a model with these capabilities at the time of this work was the main driving force behind the development of HyLloS. Nevertheless, we note that any model that can satisfy the above requirements may also be used in this stage of the simulation.

Recall that to elicit a tanning response, a minimum dose is required, and this dose may be administered at a single or multiple wavelengths [158]. Accordingly, MED_{SED} (Equation 3.2) can elicit the same tanning response that would be triggered by a spectral MMD [160]. Hence, we can simplify the calculation of the MMT to yield:

$$\Psi_{\circ} = \alpha_m(298) MMD_{SED} A(298). \quad (5.2)$$

Note that α_m and A are evaluated at 298 nm for consistency with MED_{SED} (Equation 3.2).

We then simulate the changes in skin biophysical parameters, which depend on the amount of UVR impinging on the skin specimen, *i.e.*, the exposure dose. For each exposure dose, we

calculate the effective melanogenesis signal (EMS):

$$\Psi(t) = \int_{\lambda} \alpha_m(\lambda) \psi(\lambda, t) A(\lambda) d\lambda, \quad (5.3)$$

where $\psi(\lambda, t)$ represents the spectral (radiant) exposure dose received by the skin specimen at time t . The dose received at time t can be related to the MMD* by dividing Ψ by Ψ_{\circ} :

$$d(t) = \frac{\Psi(t)}{\Psi_{\circ}}. \quad (5.4)$$

During this process, energy (relative to MMD and MAS) may be retained with the skin. This retained energy can be expressed as[†]:

$$e_{\circ}(t) = d(t) + e_{\circ}(t-1)\delta_{e_{\circ}}, \quad (5.5)$$

where $\delta_{e_{\circ}}$ is the decay of the residual energy.

As a result of this energy accumulation, a signal substance [66, 172] is then produced, triggering the melanogenesis process. The rate of production of this signal substance can be related to the stored energy:

$$s_{\circ}(t) = e(t) + s_{\circ}(t-1)\delta_{s_{\circ}}, \quad (5.6)$$

$$e(t) = \begin{cases} 0 & \text{when } e_{\circ}(t) < 1 \\ e_{\circ}(t) & \text{otherwise,} \end{cases} \quad (5.7)$$

where $\delta_{s_{\circ}}$ is the decay of the rate of production. Note that the variable $e(t)$ is defined to ensure that a tanning response occurs only when the EMS exceeds the MMT (*i.e.*, exposure dose exceeds MMD).

Finally, the actual amount of the signal substance produced at a time t can then be expressed as:

$$s(t) = s_{\circ}(t) + s(t-1)\delta_s, \quad (5.8)$$

where δ_s is the decay of the signal substance.

*If ψ is given in terms of SED, then $d(t)$ can be directly evaluated as $\psi(t)/MED_{SED}$.

[†]This equation can also be written as: $e_{\circ}(t) = \sum_{t_i \leq t} d(t_i)\delta_{e_{\circ}}^{(t-t_i)}$. Similar constructions can be used for other formulae presented in this thesis.

5.1.2 Melanin Production and Removal

Melanin can be introduced into the three main epidermal layers, namely stratum basale (layer 1), stratum spinosum (layer 2) and stratum granulosum (layer 3), in two ways: produced directly within each layer by melanocytes through melanogenesis, or transferred upwards from the layer below through epidermal cell migration [103]. Furthermore, melanin can be removed from each layer in two ways: degraded naturally, or transferred upwards to the layer above [184]. A diagram illustrating these phenomena is presented in Figure 5.2.

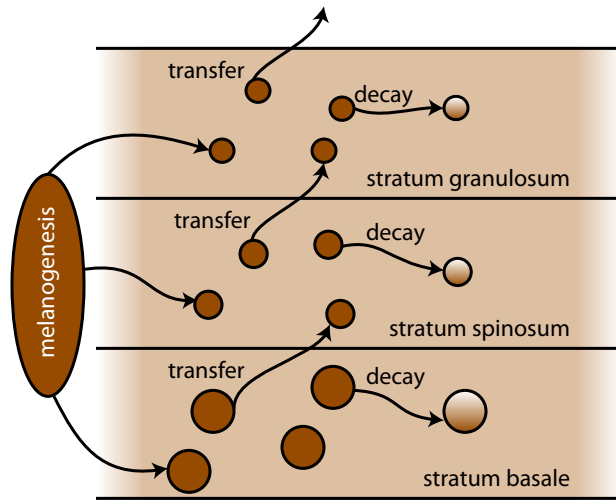


Figure 5.2: Diagram illustrating the melanin production and removal phenomena considered in our melanin dynamics simulations. The spheres represent melanosomes. The smaller spheres in the upper layers represent smaller melanosomes found in the upper layers of skin. The lighter spheres represent melanosomes encapsulating degraded melanin.

We denote the melanin production rate in a given layer i (with $i = 1, 2, 3$) as $m_{p,i}$, and the fraction of melanin transferred from layer i to the layer above as $m_{t,i}$:

$$m_{p,i}(t) = M(t)m_{p,i,f} + m_{p,i,c}, \quad (5.9)$$

$$m_{t,i}(t) = M(t)m_{t,i,f} + m_{t,i,c}, \quad (5.10)$$

where $m_{p,i,c}$ and $m_{t,i,c}$ are constitutive melanin production and transfer rates for layer i , respectively, $m_{p,i,f}$ and $m_{t,i,f}$ represent the increase in facultative melanin production and transfer rates, respectively, and $M(t)$ is a factor used to modulate the facultative melanin production and transfer rates. This factor is a function of the amount of signal substance (Equation 5.8),

i.e., a larger amount of signal substance would increase the tanning response up to an equilibrium level. It is expressed as:

$$M(t) = \frac{s^\kappa(t)}{s^\kappa(t) + \omega^\kappa}, \quad (5.11)$$

where κ and ω correspond to coefficients associated with the Hill function for physicochemical equilibrium [69] used to represent the effectiveness of the signal substance regulating the melanogenesis process. The relative melanin content in layer i is given by:

$$\begin{aligned} \hat{m}_i(t) = & m_{p,i}(t) + \\ & \delta_m(1 - m_{t,i}(t-1))\hat{m}_i(t-1) + \\ & m_{t,i}(t-1)\hat{m}_{i-1}(t-1), \end{aligned} \quad (5.12)$$

where δ_m is the fraction of melanin that remains from melanin degradation. Since there is no layer below the stratum basale capable of transferring melanin upwards, the third term of Equation 5.12 can be omitted when applied to the stratum basale.

At time $t = 0$, $\hat{m}_i(t)$ corresponds to the steady state. That is, if there is no tanning, then $\hat{m}_i(0) = \hat{m}_i(t)$ for any t . Similarly, $m_{p,i}(t) = m_{i,c}^p$ and $m_{t,i}(t) = m_{t,i,c}$. Thus, the steady state value for layer i can be written as:

$$\hat{m}_i(0) = \begin{cases} \frac{m_{p,i,c}}{1 - \delta_m(1 - m_{t,i,c})} & \text{when } i = 1 \\ \frac{m_{p,i,c} + m_{t,i-1,c}m_{i-1}}{1 - \delta_m(1 - m_{t,i,c})} & \text{otherwise.} \end{cases} \quad (5.13)$$

We remark that Equation 5.12 is used to describe the relative melanin content between the different layers in relation to the initial content. That is, the sum of melanin contents assigned to the three layers at time $t = 0$ is equal to 1, and the total normalized increase in melanin pigmentation at time t can be calculated as:

$$\Delta\hat{m}(t) = \sum_{i=1}^3 \hat{m}_i(t). \quad (5.14)$$

Accordingly, the fraction of total melanin located in layer i at time t is given by $\hat{m}_i(t)/\Delta\hat{m}(t)$.

Then, for each layer i at time t , the updated melanin content can be evaluated as:

$$\begin{aligned}
m_i(t) &= \text{epidermal melanin pigmentation increase at time } t \times \\
&\quad \text{proportion of total melanin in layer } i \text{ at time } t \times \\
&\quad \text{original epidermal melanin pigmentation content} \div \\
&\quad \text{proportion of epidermis occupied by layer } i \\
&= \Delta \hat{m}(t) \frac{\hat{m}_i(t)}{\Delta \hat{m}(t)} \left[\sum_{\iota=1}^3 \left(\frac{\bar{m}_\iota \tau_\iota}{\tau_e} \right) \right] \left[\frac{\tau_i}{\tau_e} \right]^{-1} \tag{5.15}
\end{aligned}$$

$$= \frac{\hat{m}_i(t)}{\tau_i} \sum_{\iota=1}^3 (\bar{m}_\iota \tau_\iota), \tag{5.16}$$

where \bar{m}_i is the original melanin content for layer i , τ_i corresponds to the original thickness of layer i , and τ_e represents the original thickness of the epidermis, *i.e.*, the sum of τ_1 , τ_2 and τ_3 .

5.2 Thickness Dynamics

In contrast to the melanin production mechanism, the hyperplasia mechanism is not limited to the epidermal layers [112, 145]. We note, however, that both adaptive mechanisms are dependent on UVR exposure [26], and their simulations follow a similar algorithmic approach.

5.2.1 UVR Dose Evaluation

We start by determining the minimum exposure dose necessary to elicit a skin thickening response. We refer to this quantity as the minimum thickening threshold (MTT), and evaluate it using the following expression:

$$\Psi'_\circ = \int_{\lambda} \alpha_e(\lambda) \psi'_\circ(\lambda) A(\lambda) d\lambda, \tag{5.17}$$

where α_e is the erythema action spectrum (EAS) and ψ'_\circ is the spectral MED. The EAS is plotted in Figure 3.4 (right). We employ the EAS here since it has been indicated that changes in skin thickness are related to erythema responses [112]. Like Ψ_\circ (Equation 5.2), Ψ'_\circ can be rewritten to yield:

$$\Psi'_\circ = \alpha_e(298) MED_{SED} A(298). \tag{5.18}$$

Next, for each exposure dose, we calculate the effective thickening signal (ETS) absorbed by the skin specimen:

$$\Psi'(t) = \int_{\lambda} \alpha_e(\lambda) \psi(\lambda, t) A(\lambda) d\lambda, \quad (5.19)$$

which can then be quantified in terms of the MTT:

$$d'(t) = \frac{\Psi'(t)}{\Psi'_o}. \quad (5.20)$$

During this process, energy (relative to MED and EAS) may also be retained in the skin. This retained energy can be expressed as:

$$e'_o(t) = d'(t) + e'_o(t-1)\delta_{e'_o}, \quad (5.21)$$

where $\delta_{e'_o}$ accounts for the decay of this residual energy.

Analogous to the procedure employed in the melanin dynamics component, the rate of production of the signal substance associated with the hyperplasia process can be related to the stored energy as:

$$s'_o(t) = e'(t) + s'_o(t-1)\delta_{s'_o}, \quad (5.22)$$

$$e'(t) = \begin{cases} 0 & \text{when } e'_o(t) < 1 \\ e'_o(t) & \text{otherwise,} \end{cases} \quad (5.23)$$

where $\delta_{s'_o}$ is the decay of the rate of production. Note that the variable $e'(t)$ is defined to ensure that a skin thickening response occurs only when the ETS exceeds the MTT.

Finally, the actual amount of the signal substance produced at a time t can then be expressed as:

$$s'(t) = s'_o(t) + s'(t-1)\delta_{s'}, \quad (5.24)$$

where $\delta_{s'}$ is the decay of the signal substance.

5.2.2 Thickness Regulation

The regulation of skin thickness is assumed to be the result of two competing processes: the generation and loss of skin cells. The generation of skin cells, denoted as τ_p , can be expanded

upon as:

$$\tau_p(t) = M'(t)\tau_{p,tan} + \tau_{p,base}, \quad (5.25)$$

where $\tau_{p,base}$ represents to the baseline skin cell production rate, $\tau_{p,tan}$ corresponds to the increase in this production rate, and $M'(t)$ is a factor that modulates the effect of this increase. Analogous to the melanogenesis process, this factor is a function of the amount of the corresponding signal substance, and it is expressed in terms of the Hill function for physicochemical equilibrium [69] as:

$$M'(t) = \frac{s'^{\kappa'}(t)}{s'^{\kappa'}(t) + \omega'^{\kappa'}}, \quad (5.26)$$

with κ' and ω' representing coefficients associated with this function [69].

The actual skin thickness is then given by:

$$\tau(t) = \tau_p(t) + \tau(t-1)\delta_\tau, \quad (5.27)$$

where δ_τ accounts for the loss in skin cells. At time $t = 0$, $\tau(t)$ corresponds to the steady state:

$$\tau(0) = \frac{\tau_{p,base}}{1 - \delta_\tau}. \quad (5.28)$$

Finally, the normalized thickness change at time t can be evaluated as:

$$\Delta\tau(t) = \frac{\tau(t)}{\tau(0)}. \quad (5.29)$$

Recall that the thickness regulation algorithm computes the change in thickness for the entire skin. Hence, at time t , one simply scales the original values assigned to each skin layer by $\Delta\tau(t)$. In addition, we remark that melanin content is expressed in terms of volume fraction. Accordingly, to avoid inadvertently altering the amount of melanin present in the cutaneous tissues when scaling the thickness, one divide the melanin content of each of the layers by $\Delta\tau(t)$.

5.3 Framework Output

Once the dynamics simulations are completed, the values for the updated biophysical parameters, namely melanin content and thickness, can be used as input for a light interaction model to enable the computation of skin appearance attributes quantified in terms of spectral reflectance and BSSRDF. These, in turn, can be employed in the generation of images portraying the resulting skin appearance changes.

Note that the model employed in this task, HyLloS (Chapter 4), takes into account the distribution of melanin in colloidal and aggregated (encapsulated within the melanosomes) forms. Hence, the change in melanin content resulting from the dynamics simulations is applied to the contents of both forms of melanin found in each epidermal layer according to their original proportions used in the characterization of the specimen at hand. Besides melanin content, accounting for the distribution is important since both the content and distribution have impact on appearance attributes [131, 136, 180, 204]. This aspect is demonstrated in Figure 5.3 in which HyLloS yields distinct reflectance curves in the visible spectral domain for specimens that have the same overall melanin content. The two cases being considered are the basal case, where all melanosomes are in the stratum basale, and the dispersed case, where melanosomes are distributed throughout the epidermis. Note that similar results can also be obtained within the UV and IR spectral domains (Appendix C). In general, these results agree with the literature in suggesting that dispersed melanosomes increase absorptance [131, 136, 180, 204].

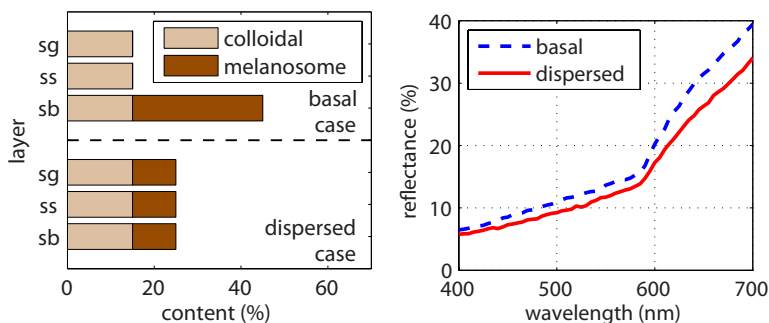


Figure 5.3: Effect of different melanin distributions on visible reflectance of a darkly pigmented specimen. Left: bar chart presenting the different distributions of melanin in colloidal and melanosome forms. The epidermal layers, namely stratum granulosum, stratum spinosum and stratum basale are denoted by sg, ss and sb, respectively. Top three bars are for the basal case and the bottom three bars are for the dispersed case. Right: visible reflectance between the two cases are significantly different even when the melanin content is the same.

Animations showing skin appearance changes over time can be produced by employing

the updated parameter values provided by the framework at every time step. In the case of features like tan lines, their rendering can be performed by taking advantage of the contrast provided by the original and modified appearance attributes. Alternatively, the updated biophysical parameters can be used in data-driven investigations of skin related photobiological phenomena.

6 Evaluation Methodology

In this chapter, we describe how we evaluated the predictive capabilities of the HyLloS model and the tanning simulation framework in Sections 6.1 and 6.2 respectively. In each of these sections, we present the data and procedures used in our evaluations and discuss issues regarding the usability and performance of the proposed light interaction model and tanning simulation framework. We will also present an input sensitivity analysis for HyLloS (Section 6.1.3) to assess the impact of its key parameters.

6.1 Evaluating the HyLloS Model

In order to evaluate the predictive capabilities of the HyLloS model, we have compared its results with measured data and experimental observations reported in the literature. An input sensitivity analysis is used to demonstrate the impact of the different constituents on skin spectral responses. Additionally, renderings are presented that utilize the appearance attributes generated by the model in the UV, visible and IR spectral domains.

6.1.1 Skin Characterization Data

In the absence of measured skin characterization data for the specimens used in the actual experiments, the values assigned to the pigmentation parameters employed in the computation of the HyLloS modelled curves (Tables 6.1 and 6.2) were selected based on the specimens' original descriptions and the corresponding ranges for these parameters provided in related scientific works [82, 90, 103, 110]. In order to account for melanosome degradation in the upper epidermal layers [131], the axes of the melanosomes located in the stratum spinosum and stratum granulosum were set to be, respectively, 50% and 25% of the values (in $\mu m \times \mu m$) provided by Olson [136], namely 0.40×0.17 and 0.69×0.28 for lightly and darkly pigmented specimens respectively.

Parameter	S1	S2	S3	S4	Source
Surface Fold Aspect Ratio*	0.1	0.25	0.1	0.45	[114, 182]
SC Thickness (<i>cm</i>)	0.001	0.001	0.0004	0.0004	[7, 49]
SG Thickness (<i>cm</i>)	0.0017	0.0033	0.0033	0.0007	[162]
SS Thickness (<i>cm</i>)	0.0017	0.0033	0.0033	0.0007	[162]
SB Thickness (<i>cm</i>)	0.0017	0.0033	0.0033	0.0007	[170]
PD Thickness (<i>cm</i>)	0.02	0.01	0.02	0.023	[6]
RD Thickness (<i>cm</i>)	0.1	0.1	0.125	0.2	[6]
SG Melanosome Content (%)	1.0	0.0	0.0	10.0	[103, 110]
SS Melanosome Content (%)	1.0	0.0	0.0	10.0	[103, 110]
SB Melanosome Content (%)	1.0	3.75	3.0	10.0	[103, 110]
SG Colloidal Melanin Content (%)	0.8	1.25	1.35	15.0	[3, 103, 143]
SS Colloidal Melanin Content (%)	0.8	1.25	1.35	15.0	[3, 103, 143]
SB Colloidal Melanin Content (%)	0.8	1.25	1.35	15.0	[3, 103, 143]
Melanosome Eum. Conc. (<i>mg/mL</i>)	90.0	50.0	32.0	50.0	[82, 186]
Melanosome Pheom. Conc. (<i>mg/mL</i>)	4.0	2.0	2.0	4.0	[82, 186]
Melanosome Dimensions ($\mu m \times \mu m$)	0.41×0.17	0.41×0.17	0.41×0.17	0.69×0.28	[136]
Papillary Dermis Blood Content (%)	0.2	0.7	0.3	2.5	[56, 90]
Reticular Dermis Blood Content (%)	0.2	0.7	0.3	2.5	[56, 90]
Oxygenated Blood Fraction (%)	75.0	95.0	75.0	75.0	[8]

Table 6.1: Values for specimen dependent parameters employed by HyLloS. The datasets S1, S2 and S3 correspond to specimens with relative low level of melanin pigmentation [41, 198], while dataset S4 corresponds to a specimen with a high level of melanin pigmentation [93, 94]. Accordingly, the simulations consider the melanosomes distributed as complexes (Figure 3.1 (left)) when using datasets S1, S2 and S3, and as individually dispersed particles (Figure 3.1 (right)) when using dataset S4 [136, 180]. *Note that in the case of the comparisons involving goniometric data (Figures 6.7 and 6.8), the aspect ratio of the surface folds was set to 0.3 to approximate the description of the lightly pigmented individual whose measured skin goniometric data [116] was employed as a reference in this thesis.

Parameter	Value	Source
Stratum Corneum Refractive Index	1.55	[48, 183]
Epidermis Refractive Index	1.4	[183, 191]
Papillary Dermis Refractive Index	1.39	[92, 183]
Reticular Dermis Refractive Index	1.41	[92, 183]
Melanin Refractive Index	1.7	[20]
Hemoglobin Concentration in Whole Blood (<i>mg/mL</i>)	147.0	[56, 113]
Methemoglobin Concentration in Whole Blood (<i>mg/mL</i>)	1.5	[81]
Carboxyhemoglobin Concentration in Whole Blood (<i>mg/mL</i>)	1.5	[43]
Sulfhemoglobin Concentration in Whole Blood (<i>mg/mL</i>)	0.0	[209]
Whole Blood Bilirubin Concentration (<i>mg/mL</i>)	0.003	[213]
Stratum Corneum Beta-carotene Concentration (<i>mg/mL</i>)	2.1E-4	[109]
Epidermis Beta-carotene Concentration (<i>mg/mL</i>)	2.1E-4	[109]
Blood Beta-carotene Concentration (<i>mg/mL</i>)	7.0E-5	[109]
Stratum Corneum Water Content (%)	35.0	[2, 125]
Epidermis Water Content (%)	60.0	[2, 197]
Papillary Dermis Water Content (%)	75.0	[2, 197]
Reticular Dermis Water Content (%)	75.0	[2, 197]
Stratum Corneum Lipid Content (%)	35.0	[203]
Epidermis Lipid Content (%)	20.0	[2, 31, 174]
Papillary Dermis Lipid Content (%)	15.1	[2, 31, 174]
Reticular Dermis Lipid Content (%)	17.33	[2, 31, 174]
Stratum Corneum Keratin Content (%)	65.0	[60, 64, 170]
Stratum Corneum Urocanic Acid Density (<i>mol/L</i>)	0.01	[211]
Skin DNA Density (<i>mg/mL</i>)	0.185	[2, 57, 196]

Table 6.2: Values for specimen independent parameters employed by HyLloS. The refractive indices for the skin layers were measured at 1300 *nm* as reported in the listed sources.

We note that HyLloS can be run online [126] via a model distribution system [16]. Accordingly, using a dedicated website (Figure 6.1), researchers are able to specify simulation conditions (*e.g.*, angle of incidence and spectral range), modify specimen characterization parameters, and obtain modelled directional-hemispherical reflectance curves, including those depicted in the quantitative comparisons presented in this work. The standard version of this website depicts model parameters normally employed to characterize distinct skin specimens. Their default values were employed to generate the modelled reflectance curve associated with the dataset S3 indicated in this thesis. For consistency with the related scientific literature, the values assigned to model parameters have been restricted to physiologically valid ranges. The full set of model parameters, including those normally not subject to change for the simulations (Table 6.2), can also be accessed and modified in the extended version (which is linked from the standard version) of this website. Regarding the rendered images in the visible domain presented herein, unless otherwise stated, they were generated considering BSSRDF readings and

light sources that approximate a standard D65 illuminant [85].

6.1.2 Quantitative and Qualitative Comparisons

Existing skin appearance models designed for applications in the visible domain, such as the diffusion theory based model proposed by Donner and Jensen [50] (henceforth referred to as DJ06 after its developers) and the stochastic model proposed by Krishnaswamy and Baranoski [14, 104] (known as BioSpec), assume melanin to be uniformly distributed in a single layer representing the epidermis. Moreover, they do not take into account either the particle nature or the distribution patterns of the melanosomes (Section 3.2). These limitations preclude these models from accounting for detour and sieve effects (Section 3.3), which can lead to prominent discrepancies, notably in the blue region of spectrum characterized by higher melanin absorption. Such discrepancies can be observed in the graphs presented in Figure 6.2. These graphs show comparisons of modelled results provided by DJ06, BioSpec and HyLloS with measured results provided by Vrhel et al. [198] considering an angle of incidence of 45° , which are made available in a spectra database at the North Carolina State University (NCSU). In these comparisons, we employed NCSU curves used as references in the original evaluations of DJ06 and BioSpec. Note that the DJ06 modelled results depicted in Figure 6.2 were originally computed with the amount of eumelanin set to zero as reported by Donner and Jensen [50]. Although this can mitigate the absorption related limitations of the diffusion theory approximation outlined in Section 2, we remark that eumelanin is the dominant form of melanin present in human skin under normal physiological conditions [7, 32, 82, 103].

According to the trichromatic theory of colour perception [85], the human eye’s response to short-wavelength (associated with the 400 nm to 500 nm “blue” region of the visible spectral domain) light stimulus is significantly weaker than its response to medium- and long-wavelength light stimuli (respectively associated with the 500 nm to 600 nm “green” and 600 nm to 700 nm “red” regions of the visible spectral domain). Since the previously mentioned discrepancies are located in the blue region of the visible spectrum, it is expected that they have a lower impact in the rendering of believable images of human skin. In order to illustrate this aspect, we have generated skin swatches using the data presented in Figure 6.2 (reflectance from 400 nm to 700 nm , with a resolution of 5 nm) in conjunction with a standard XYZ to sRGB conversion procedure [177]. As it can be observed in the images depicted in Figures 6.3 and 6.4, despite these discrepancies, all three models can be effectively employed in the rendering of believable skin images. We remark, however, that the parameter values used in the computation of the curves modelled by BioSpec and HyLloS (Figure 6.2) were in closer agreement with the biophysical characteristics of skin specimens under normal physiological conditions, particularly with respect to eumelanin content.

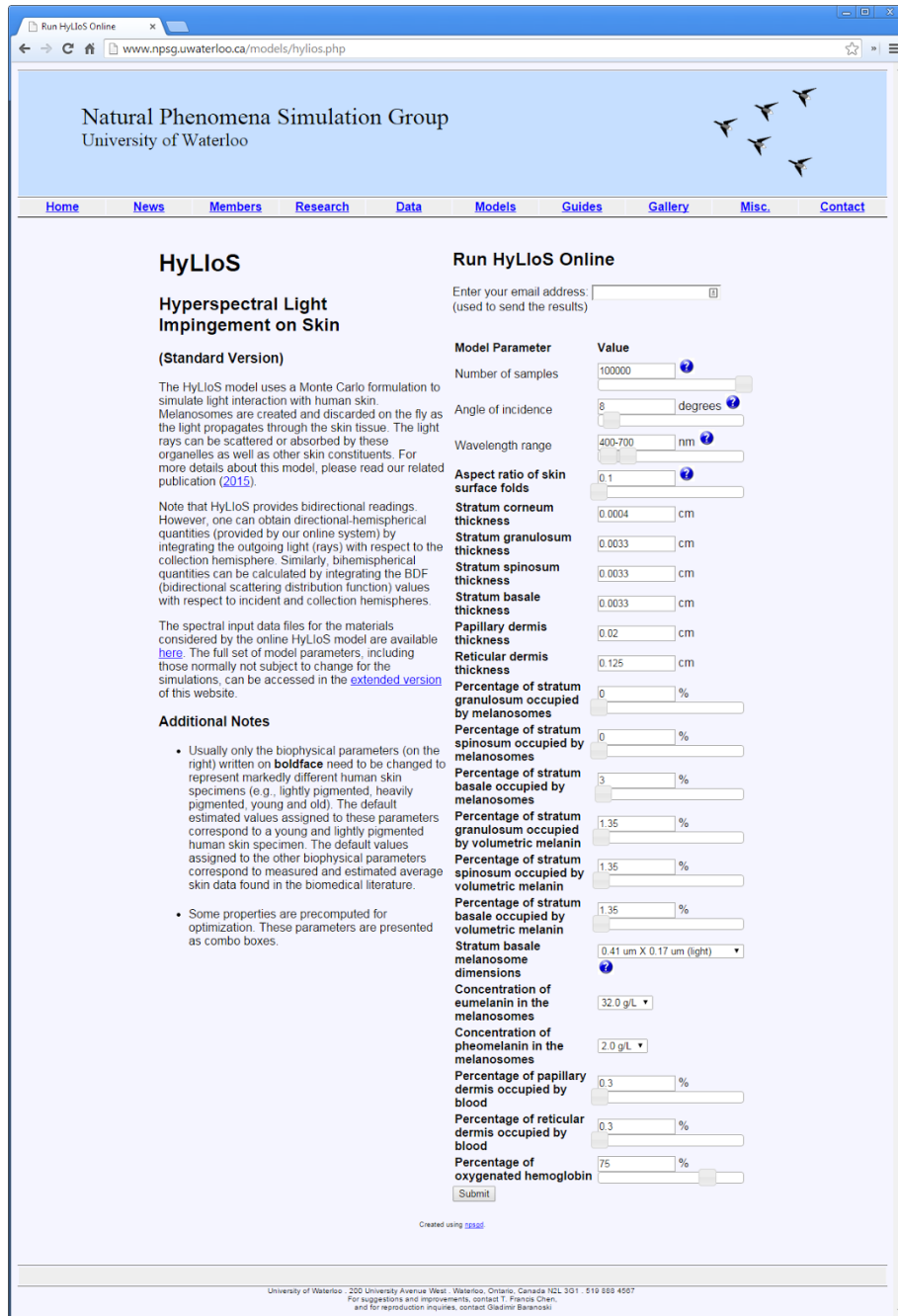


Figure 6.1: Website for running the HyLloS model online [126].

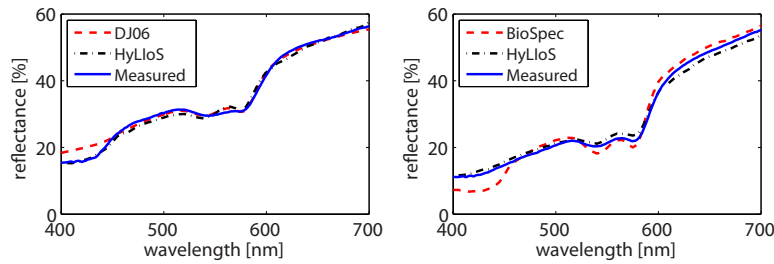


Figure 6.2: Comparisons of modelled spectral curves obtained using DJ06 [50], BioSpec [18] and HyLloS models with measured NCSU spectral curves 117 (left) and 113 (right) [198]. The HyLloS curves on the left and right were computed using the pigmentation datasets S1 and S2 respectively (Tables 6.1 and 6.2).



Figure 6.3: Skin swatches generated using modelled spectral curves provided by DJ06 (left) and HyLloS (centre) models along with a reference swatch (right) generated using measured data (NCSU spectral curve 117) provided by Vrhel et al. [198]. The respective spectral curves are depicted in Figure 6.2 (left).

The first principles simulation approach employed by HyLloS accounts not only for detour and sieve effects, but also for the strong forward scattering behaviour of the epidermal layers, notably in the UV domain [28] as shown in the plot presented in Figure 6.5. Recall that the particle nature and distribution patterns of the melanosomes have an even stronger influence on the skin spectral responses in the UV range [7,32], and the existing spectral models, different from HyLloS, do not account for these factors. Hence, the simple incorporation of additional absorbers acting in the UV domain into these models would likely lead to discrepancies similar to those observed in the blue region of the visible spectrum (Figure 6.2).

In order to demonstrate the predictive capabilities of HyLloS across the UV–Visible–IR range, we compared modelled curves with measured curves provided by Cooksey and Allen [41] and Jacquez et al. [93, 94], which were obtained for lightly and darkly pigmented skin speci-

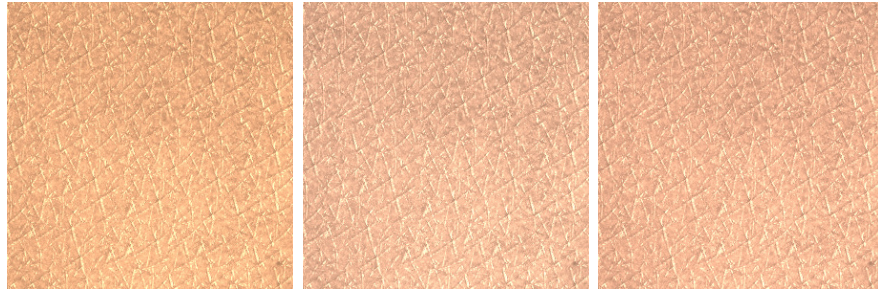


Figure 6.4: Skin swatches generated using modelled spectral curves provided by BioSpec (left) and HyLloS (centre) models along with a reference swatch (right) generated using measured data (NCSU spectral curve 113) provided by Vrhel et al. [198]. The respective spectral curves are depicted in Figure 6.2 (right).

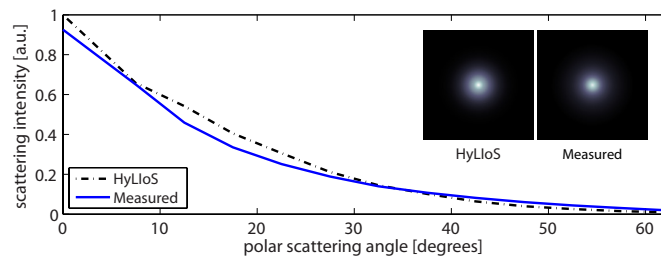


Figure 6.5: Comparison of modelled subsurface scattering data obtained using HyLloS with measured subsurface scattering data provided by Bruls and van der Leun [28] for the epidermis of a lightly pigmented skin specimen considering normal incidence of UV light (at 302 nm). The modelled data was computed using the pigmentation dataset S2 (Tables 6.1 and 6.2). The insets depict orthographic projections of the measured and modelled subsurface scattering data presented in the graph.

mens considering angles of incidence of 8° and 16.75° respectively. As it can be observed in the graphs provided in Figure 6.6, the relevant hyperspectral features (represented by the “peaks” and “valleys”) and trends are reproduced by the modelled curves. For example, for wavelengths longer than $\approx 1300\text{ nm}$, the absorption is dominated by the presence of water and lipids instead of melanin pigmentation [7], resulting in a similarity between the measured reflectance spectra in this region. Such a similarity can also be observed between the modelled reflectance spectra. We note that localized quantitative variations can be expected across the UV–Visible–IR domains since we employed for both specimens the same average values for key characterization parameters such as the water content and the refractive index associated with each skin layer. As demonstrated by Cooksey and Allen [41], population variability is the most significant source of uncertainty in the measurement of skin reflectance. We note, however, that

our modelled results were obtained using parameter values within physiologically valid ranges indicated in the scientific literature.

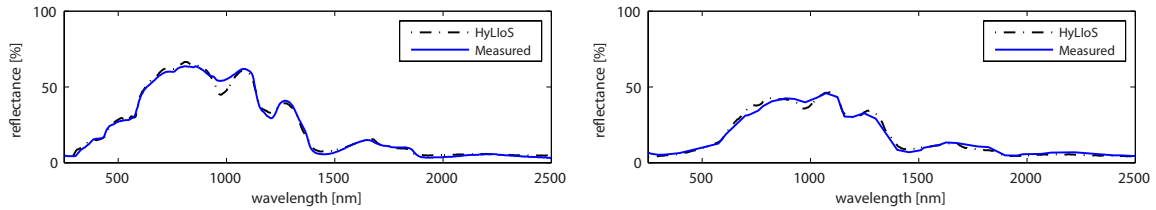


Figure 6.6: Comparisons of modelled hyperspectral curves obtained using HyLloS with measured curves for a lightly pigmented specimen (left) provided by Cooksey and Allen [41] and a darkly pigmented specimen (right) provided by Jacquez et al. [93, 94]. The HyLloS curves (from 250 nm to 2500 nm) for the lightly and darkly pigmented specimens were computed using the pigmentation datasets S3 and S4 respectively (Tables 6.1 and 6.2).

We also examined the predictions of HyLloS with respect to the spatial distribution of light. Although these predictions can be represented in terms of BSSRDF, we quantified them in terms of BRDF and integrated the resulting values over the visible domain to obtain BRDF curves that could be compared to measured BRDF curves provided by Marschner et al. [116]. As it can be observed in the comparisons depicted in Figure 6.7, HyLloS can capture the angular dependency of the spatial distribution of light interacting with human skin in the visible domain. Moreover, recall that IR light can penetrate deeper into the cutaneous tissues than UV light [7], and it can reach the dermal layers where it becomes progressively more diffuse [92]. As a result, the subsurface reflectance has a more dominant role in the IR domain, and the overall reflected IR light, notably in the region below 1300 nm (less susceptible to water absorption), has a more diffuse distribution than UV light [7, 78]. The scattering plots presented in Figure 6.8 indicate that HyLloS can capture these distinct spatial distribution patterns of UV and IR light interacting with human skin.

The images presented in Figure 6.9 further demonstrate that HyLloS can capture the distinct scattering behaviours of human skin in the hyperspectral domain. For example, the subject’s face shows a more specular (glossier) behaviour under UV light, and a more diffuse behaviour under IR light (below 1300 nm), which are consistent with observations reported in the scientific literature [7, 78]. It can also be observed that although a more compact BRDF representation may be sufficient to capture the scattering profile in the UV domain (Figure 6.9 (left)), it cannot fully describe the “soft”, more diffuse, “ethereal” skin appearance in the IR domain [59, 167] provided by a BSSRDF representation (Figure 6.9 (right)).

It has been observed that a progressive increase in the overall epidermal melanin content

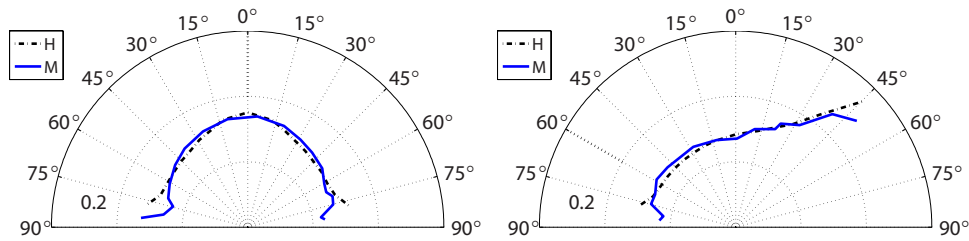


Figure 6.7: Comparison of modelled BRDF curves (H) provided by HyLloS with measured BRDF curves (M) provided by Marschner et al. [116] for a lightly pigmented specimen considering two angles of incidence: 0° (left) and 60° (right). The modelled curves were obtained considering the pigmentation dataset S1 (Tables 6.1 and 6.2).

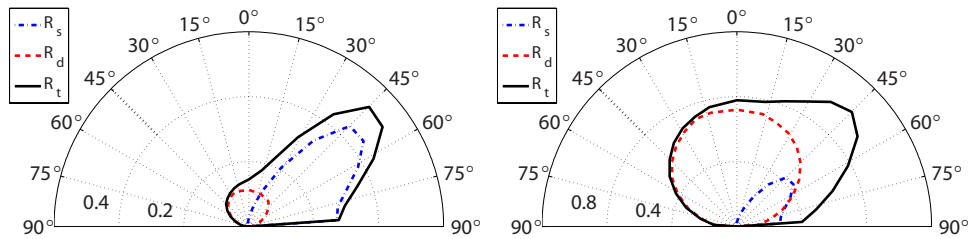


Figure 6.8: Scattering plots provided by HyLloS showing surface (R_s), subsurface (R_d), and total (R_t) reflectance distributions in the UV (left) and IR (right) domains. Note the more diffuse total reflectance distribution of IR light (below 1300 nm) as reported in the scientific literature [7, 78]. These plots correspond to normalized bidirectional reflectance values at 365 nm (left) and 1100 nm (right) multiplied by the cosine of the reflection angle. The bidirectional reflectance values were computed considering an angle of incidence of 45° and using the pigmentation dataset S1 (Tables 6.1 and 6.2).

leads to a fast convergence to low reflectance values in the UV domain [63]. As demonstrated by the images presented in Figure 6.10, HyLloS can reproduce this trend. Moreover, these images are also consistent with measurements showing practically identical reflectance responses for moderately and darkly pigmented specimens in the UV domain [41, 94].

Within the IR domain, the skin spectral responses are primarily determined by the absorption bands of water [41, 93]. A myriad of physiological and environmental factors can alter the barrier activity of skin, thus intensifying water loss [9]. A reduction of water content in the cutaneous tissues [24], in turn, results in an increase in reflectance in the IR domain [7, 9]. As shown by the images presented in Figure 6.11, this behaviour is also captured by HyLloS.

The presence of pigmentation irregularities, such as freckles and moles, is accentuated when a skin specimen is viewed under UV light due to the strong attenuation properties of mela-

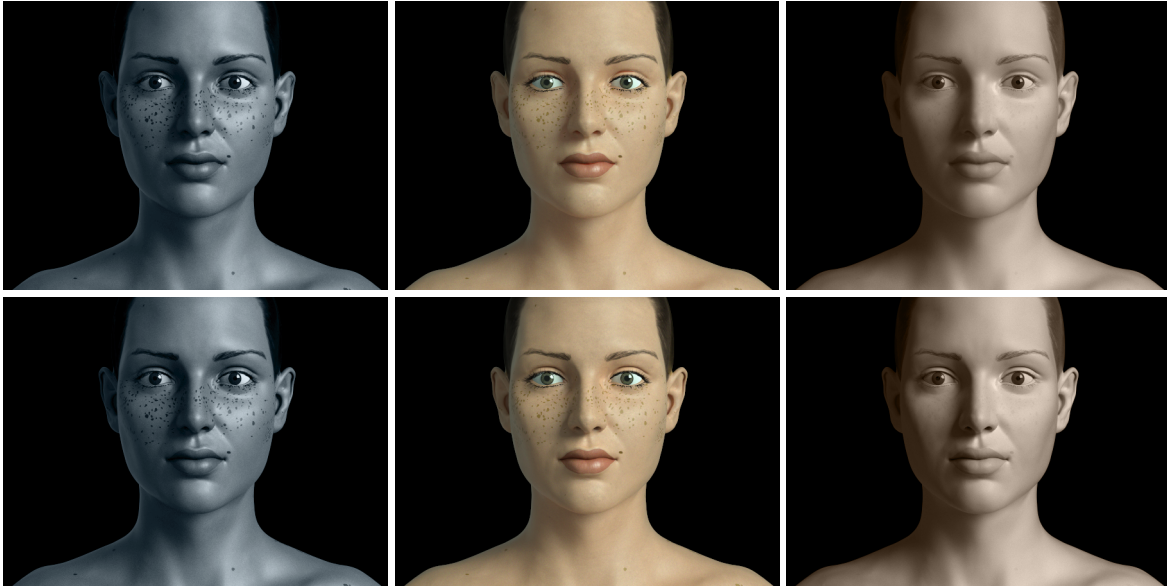


Figure 6.9: Images showing distinct skin appearance features in the UV (left), visible (centre) and IR (right) spectral domains. These images were rendered using BSSRDF (top row) and BRDF (bottom row) representations of spatial light distributions provided by the proposed hyperspectral model in these domains. Note that HyLloS can predictively simulate not only the intensification of pigmentation irregularities in the UV range, but also the “soft”, “ethereal” (more diffuse and less affected by the presence of pigmentation irregularities) appearance of human skin in the IR range [167], notably below 1300 nm [7]. The UV and IR responses (at 365 nm and 1100 nm respectively) are depicted using pseudo colour.

nin in this spectral domain [63, 143]. This phenomenon is predictively simulated by HyLloS as depicted in the images of a lightly pigmented individual (1.5% epidermal melanin content) presented in Figure 6.9. In these images, it can also be observed that the presence of these irregularities is less apparent in the IR domain, which is also consistent with empirical observations reported in the IR imaging literature [59, 167].

Due to the increasingly diminished contributions of melanin to light attenuation beyond 1100 nm , the presence of pigmentation irregularities may become completely undetectable in this region dominated by water absorption [7, 93]. In addition, the subsurface scattering contributions to skin reflectance tend to decrease due to the dominant role of water absorption, resulting in a more specular (glossier) and darker (lower reflectance) appearance of skin in this domain. As demonstrated by the images presented Figure 6.12, these trends are also predictively reproduced by HyLloS.



Figure 6.10: Images showing the effects of increased overall melanin pigmentation on skin UV responses as reported in the scientific literature [7, 41, 63, 94, 130]. Left: 1.5%. Centre: 7%. Right: 30%. The UV responses (at 365 nm) provided by HyLioS are depicted in pseudo colour. Polygonal mesh courtesy of XYZ RGB Inc.

6.1.3 Input Sensitivity Analysis

In the previous section, we have illustrated some of the effects that the main absorbers found within the cutaneous tissues have on modelled skin appearance attributes obtained using HyLioS. Due to the different roles of these materials in the UV (250 nm to 400 nm), visible (400 nm to 700 nm) and IR (700 nm to 2500 nm) regions of the light spectrum, it is expected that for applications targeting a specific spectral domain, the parameters associated with a number of these materials may be kept fixed, *i.e.*, set to standard (average) values. In order to assess this possibility, we have performed an input sensitivity analysis [74, 75] in which we compared reflectance values obtained considering the complete dataset S3 with reflectance values computed using modified versions of this dataset. These versions, in turn, account for the removal of specific materials, namely melanin, blood, DNA, keratin, water and lipids. Note that we selected, without loss of generality, dataset S3 as baseline since its corresponding modelled reflectance curve (Figure 6.6 (top)) covers the entire hyperspectral region of interest. We also remark that this dataset is available in the HyLioS website [126], which can be used to reproduce the results presented in this section by setting the parameters associated with a specific material to zero. The impact of each of the selected materials was quantified in terms of the mean sensitivity index [74, 75] expressed as:

$$MSI = \frac{1}{N} \sum_{i=1}^N \frac{|\rho_b(\lambda_i) - \rho_m(\lambda_i)|}{\max\{\rho_b(\lambda_i), \rho_m(\lambda_i)\}}, \quad (6.1)$$



Figure 6.11: Images showing the magnifying effects of water loss on skin IR responses as reported in the scientific literature [7,9]. These effects were simulated by reducing the water content of the cutaneous tissues of a lightly pigmented specimen (1.5% epidermal melanin content) within physiological limits [24]. Left: No reduction. Centre: 20% reduction. Right: 40% reduction. The IR responses (at 1650 nm) provided by HyLloS are depicted in pseudo colour. Polygonal mesh courtesy of XYZ RGB Inc.

where ρ_b and ρ_m correspond to the reflectances associated with the baseline and modified datasets respectively, and N is the total number of wavelengths sampled with a 5 nm resolution.

The overall results of our analysis presented in Table 6.3 show that melanin and water have the largest impact on the modelled reflectances. It is necessary to consider, however, that although a given material may not have a large impact in a certain spectral domain, it can still have a significant effect in the model's predictions. In order to demonstrate this aspect, we also present the results of our analysis grouped by materials that have their greatest impact in the visible, UV and IR domains. These results, in turn, are further illustrated by skin swatches rendered using the corresponding modelled reflectances. The swatches depicting visible traits (Figure 6.14) were generated using the same approach employed in the rendering of the swatches depicted in Figures 6.3 and 6.4. The colours of the swatches in the UV and IR domains (Figures 6.15 and 6.17) were obtained by integrating the respective reflectance values over the relevant spectral region, and applying a tinted greyscale filter to the resulting values.

As it can be observed in Figure 6.13 (left), the contributions of melanin and blood to skin appearance are prominent in the visible domain as the removal of either material significantly increases skin reflectance. Also, note that the characteristic omega shape observed in the 500 nm to 600 nm range vanishes with the removal of blood. These effects are reflected in the skin swatches (Figure 6.14), which depict a lighter appearance associated with the modified datasets.



Figure 6.12: Images showing IR responses at 1200 nm (left) and 1400 nm (right) for a lightly pigmented specimen (1.5% epidermal melanin content). Note, as reported in the scientific literature [7, 93], the disappearance of pigmentation irregularities that occurs beyond 1100 nm , as well as the more specular and darker appearance resulting from reduced subsurface scattering at a wavelength (1400 nm) characterized by strong water absorption. Both (pseudo colour) images had their brightness increased for visualization purposes.

	Removed Materials					
	Melanin	Blood	DNA	Keratin	Water	Lipids
MSI	0.415	0.229	0.135	0.068	0.611	0.026
SD	Vis	Vis	UV	UV	IR	IR
MSI_H	0.123	0.049	0.018	0.012	0.491	0.022

Table 6.3: MSI values were computed for the spectral domain, denoted by “SD”, in which the removal of each selected material has the highest impact. The MSI values computed considering the entire hyperspectral region of interest (250 nm to 2500 nm), denoted by MSI_H , are also included for reference.

In addition, these materials have a significant impact outside the visible domain (Figure 6.13 (right)). Note that the baseline dataset corresponds to a lightly pigmented specimen. For specimens with higher melanin pigmentation levels, the dominant role of melanin is expected to be even more pronounced [7]. Furthermore, changes in the distribution of melanin can also have a noticeable impact on skin reflectance as illustrated by additional *in silico* experiments presented in Appendix C.

Besides melanin and blood, other materials also have an impact, albeit not as pronounced, in the UV domain. For example, the removal of DNA or keratin yields higher reflectance (Figure 6.15 (left)), and results in a lighter UV appearance of skin (Figure 6.16). Although the removal of these materials affects other spectral regions, its effect is more significant in the UV domain (Figure 6.15 (right)).

The presence of water and lipids primarily affects the skin reflectance in the IR region, with water being the more dominant material (Figures 6.17 (left)). Accordingly, after water removal,

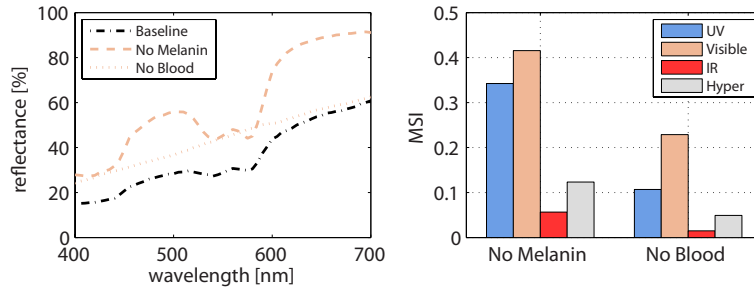


Figure 6.13: Comparison of modelled results provided by HyLloS depicting the impact of melanin and blood on skin reflectance, which were obtained considering the complete dataset S3 as the baseline and two modified versions: with no melanin and no blood. Left: reflectance curves in the visible domain. Right: MSI values for each modified reflectance curve with respect to the baseline curve across the UV, visible, IR and the entire hyperspectral region of interest (250 *nm* to 2500 *nm*) denoted by “Hyper”.

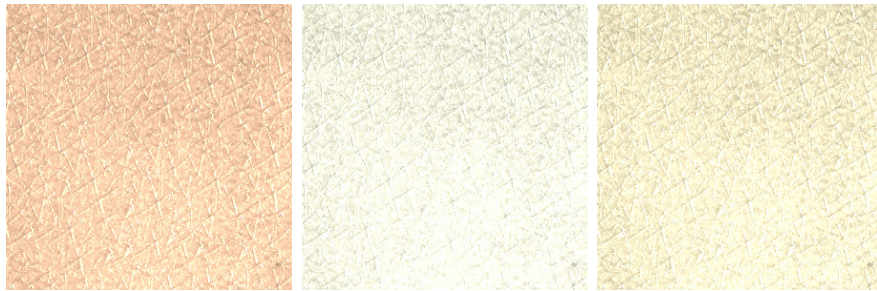


Figure 6.14: Skin swatches illustrating the impact of melanin or blood removal on the visible appearance of human skin considering the complete dataset S3 as baseline (left) and two modified versions: with no melanin (centre) and no blood (right).

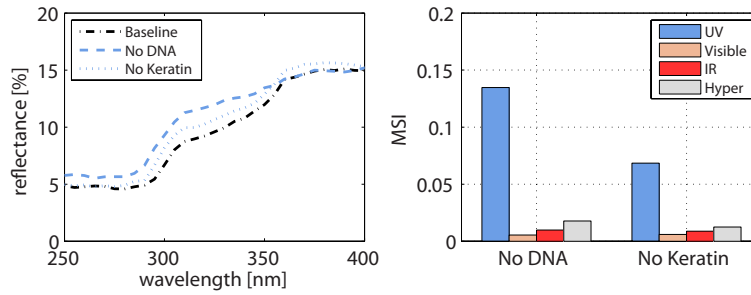


Figure 6.15: Comparison of modelled results provided by HyLIoS depicting the impact of DNA and keratin on skin reflectance, which were obtained considering the complete dataset S3 as the baseline, and two modified versions: with no DNA and no keratin. Left: reflectance curves in the UV domain. Right: MSI values for each modified reflectance curve with respect to the baseline curve across the UV, visible, IR and the entire hyperspectral region of interest (250 *nm* to 2500 *nm*) denoted by “Hyper”.

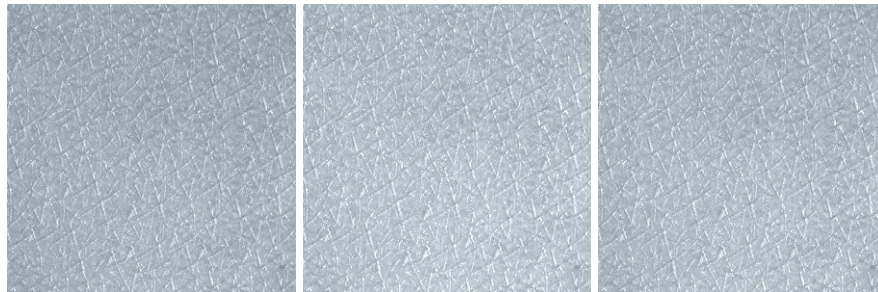


Figure 6.16: Skin swatches illustrating the impact of DNA or keratin removal on the UV appearance of human skin considering the complete dataset S3 as baseline (left) and two modified versions: with no DNA (centre) and no keratin (right). The UV responses are depicted in pseudo colour.

skin appears significantly lighter in the IR domain (Figure 6.18). On the other hand, these materials have comparably negligible impact in the UV and visible domains (Figure 6.17 (left)).

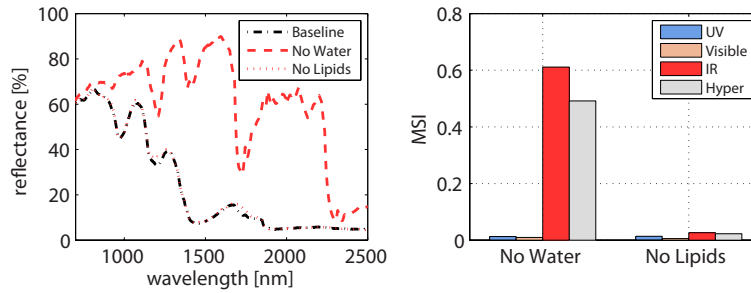


Figure 6.17: Comparison of modelled results provided HyLloS depicting the impact of water and lipids on skin reflectance, which were obtained considering the complete dataset S3 as the baseline and two modified versions: with no water and no lipids. Left: reflectance curves in the IR domain. Right: MSI values for each modified reflectance curve with respect to the baseline curve across the UV, visible, IR and the entire hyperspectral region of interest (250 nm to 2500 nm) denoted by “Hyper”.

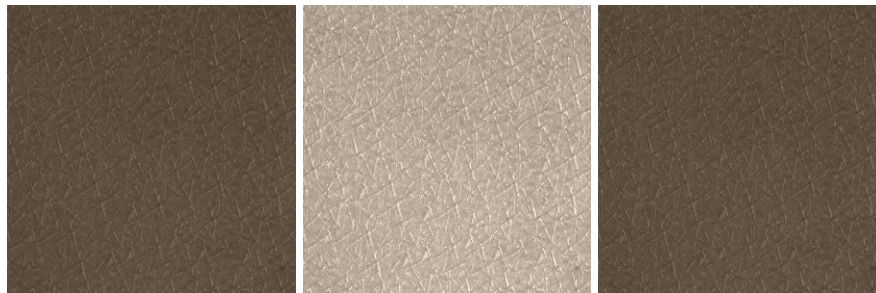


Figure 6.18: Skin swatches illustrating the impact of water or lipids removal on the IR appearance of human skin considering the complete dataset S3 as baseline (left) and two modified versions: with no water (centre) and no lipids (right). The IR responses are depicted in pseudo colour.

In summary, for simulations aimed at believable rendering applications (Figures 6.19 and 6.20), the results presented in this section indicate that only the HyLloS’ parameters associated with specific constituent materials need to be modified in order to generate images of skin specimens with distinct appearance traits in a selected spectral region. For example, in the case of the visible domain dominated by melanin and blood, a subset of parameters presented in Table 6.1 relating to melanin and blood content can lead to the most significant skin appear-

ance variations in this region. We note, however, that HyLIoS’ detailed parameter space enables experimentations with a wider range of biophysical factors associated with different physiological conditions affecting skin appearance. Such a capability is an asset for simulations aimed at broader applications in the life and health sciences (e.g., [11, 15, 36]). In Appendix D, we present one related case where HyLIoS was employed in the investigation of algorithms for the effective compression and reconstruction of skin reflectance databases [35].



Figure 6.19: Rendered images illustrating changes in the visible appearance of human skin considering an increase in epidermal melanin content from 1.5% (left) to 7% (right). Note that we employed a back/side light source to make the translucency effects prominent. Polygonal mesh courtesy of XYZ RGB Inc.



Figure 6.20: Images illustrating rendering applications of HyLIoS in the UV (left), visible (centre) and IR (right) spectral domains. The scene depicts an upper back/shoulder (epidermal melanin content equal to 1.5%) with sunscreen and water in an outdoor beach setting. The UV and IR responses (at 365 nm and 1650 nm respectively) are depicted using pseudo colour. The dark appearance of sunscreen and water outside the visible domain are attributed to their strong absorptive behaviour in the UV and IR regions respectively. Note that we have positioned the light source high above the subject in order to mimic a typical outdoor beach setting.

6.1.4 Usability and Performance Issues

We observe that the current (CPU-based) implementation of HyLloS is not particularly suitable for real-time applications in the visible domain that demand results on the order of milliseconds. For example, it took ≈ 30 s on a dual 6-core 2.66-GHz Intel Xeon machine to obtain the 5 nm resolution curves depicted in Figure 6.2 using 10^5 sample rays. Since several factors (e.g., image resolution, spectral sampling and geometry) affect rendering time, it may take minutes or hours to generate an image. However, there are several hardware and software strategies that can be explored to enhance performance. For example, appearance attributes can be computed offline, and quickly accessed on demand during the image generation process. We intend to explore such alternatives in our future work as outlined in Chapter 7.

In this stage of our work, our primary goal is to obtain a high-fidelity description of light and skin interactions while balancing data constraints. As such, while the expansive parameter space has its advantages for conducting investigations for scientific applications, it is not streamlined to directly provide artist-guided controls. Plans to address this issue are also outlined in Chapter 7.

6.2 Evaluating the Tanning Simulation Framework

In this section, we evaluate the predictive capabilities of the tanning simulation framework, and illustrate its applicability to the visualization of skin appearance changes resulting from tanning processes triggered by different UVR exposure conditions. We also address its performance and current limitations.

6.2.1 Tanning Dynamics Specification Data

We considered time-steps of 1 hour in the tanning dynamics simulations performed in this investigation. These simulations are controlled by a number of biophysical parameters, which are listed in Tables 6.4 to 6.6 along with the values assigned to them in this investigation. Although these values are based on experimental measurements reported in the literature [112, 181] (Appendix B), we note that for specimen dependent parameters, such as those listed in Table 6.4, these values may be adjusted to describe individuals with lower or higher tanning ability. As outlined in Section 5.3, the results from the tanning dynamics simulations are translated to skin appearance attributes employing the HyLloS model (Chapter 4).

epidermal layer	parameter	constitutive pigmentation level		
		\mathcal{L}	\mathcal{I}	\mathcal{H}
	$m_{p,i,c}$	0.0000	0.0000	0.0000
stratum	$m_{t,i,c}$	0.0004	0.0064	0.0003
granulosum	$m_{p,i,f}$	0.0000	0.0000	0.0000
	$m_{t,i,f}$	0.0000	0.0900	0.0700
	$m_{p,i,c}$	0.0000	0.0030	0.0020
stratum	$m_{t,i,c}$	0.0051	0.0090	0.0029
spinosum	$m_{p,i,f}$	0.0000	0.0150	0.0065
	$m_{t,i,f}$	0.0200	0.0010	0.0010
	$m_{p,i,c}$	0.0100	0.0080	0.0080
stratum	$m_{t,i,c}$	0.0081	0.0051	0.0018
basale	$m_{p,i,f}$	0.0110	0.0075	0.0085
	$m_{t,i,f}$	0.0450	0.0250	0.0300

Table 6.4: Values for constitutive pigmentation dependent parameters employed in the melanin dynamics component of the framework. The three parameter datasets associated with distinct constitutive pigmentation levels, namely \mathcal{L} (Low), \mathcal{I} (Intermediate) and \mathcal{H} (High), are based on experimental measurements performed by Tadokoro et al. [181].

parameter	δ_{e_o}	δ_{s_o}	δ_s	δ_m	κ	ω
value	0.98	0.99	0.985	0.99	0.7	500

Table 6.5: Values for constitutive pigmentation independent parameters employed in the melanin dynamics component of the framework. These values are based on experimental measurements performed by Tadokoro et al. [181].

6.2.2 Quantitative and Qualitative Comparisons

Initially, we assessed the capability of the framework to account for a phenomenon directly connected to tanning responses. More specifically, we tested its predictions with respect to photoaddition and arbitrary UVR exposure dose schedules. Photoaddition is the phenomenon where multiple smaller exposure doses yield a physiological response similar to one from a larger single dose [173]. As it can be observed in Figure 6.21, while each of the small doses independently produces a smaller pigmentation response (a small percentage increase in melanin content), in combination, they produce a response similar to that of the single large dose.

We then proceeded to compare the predictions of the framework with results of controlled experiments performed by Miller et al. [121]. In these experiments, three UVR exposure dose schedules, presented in Figure 6.23 (first column), were used to elicit skin tanning responses from a number of subjects characterized by low constitutive pigmentation levels. Accordingly, using a virtual experimental setup analogous to the actual one (Figure 6.22), the same UVR exposure doses and a specimen with the same characteristics ($MMD_{SED} = 2.89$, $MED_{SED} = 1.7$)

parameter	$\delta_{e'_o}$	$\delta_{s'_o}$	$\delta_{s'_l}$	δ_τ	κ'	ω'	$\tau_{p,base}$	$\tau_{p,tan}$
value	0.985	0.2	0.98	0.9	1	20	0.1	0.025

Table 6.6: Values for constitutive pigmentation independent parameters employed in the thickness dynamics component of the framework. These values are based on experimental measurements performed by Lopez et al. [112].

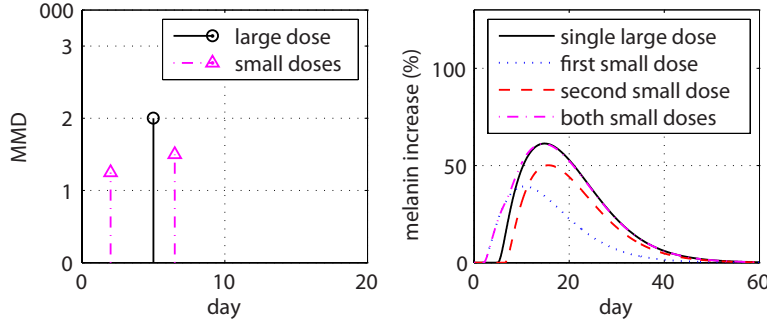


Figure 6.21: Simulated data illustrating the framework’s capability to account for the photoaddition phenomenon [173]. Left: two different UVR exposure dose schedules. Right: simulated melanin increase results provided by the framework. The simulations were performed considering a specimen with low constitutive pigmentation level (Tables 6.4 to 6.6).

as one employed by Miller et al. [121], we performed tanning dynamics simulations for a specimen with a low constitutive pigmentation level (Tables 6.4 to 6.6). The resulting simulated physiological changes are presented in Figure 6.23 (second to fourth columns). This information was then used as input for HyLlOs in order to obtain reflectance values. These, in turn, were employed to obtain $L^*a^*b^*$ colour space* coordinates considering the same standard D65 illuminant used by Miller et al. [121]. As it can be observed in Figure 6.23 (rightmost column), the simulated and measured values obtained for the lightness (L^*) coordinate show good agreement, especially considering the variations in the actual experiments (indicated by error bars) associated with expected differences in the subjects’ biophysical characteristics. In Figure 6.24, we present a sequence of images to illustrate the temporal visible appearance changes resulting from three UVR exposure schedules considered in these comparisons.

It has been experimentally demonstrated that individuals with a high level of constitutive pigmentation have a higher MMD (Section 3.4), *i.e.*, a higher UVR exposure dose is required to trigger their tanning process [158, 159]. Hence, since these specimens are less sensitive to

*The $L^*a^*b^*$ colour space defined by the CIE employs three coordinates to specify colour. The L^* coordinate approximately correlates to lightness while coordinates a^* and b^* together approximately correlate to hue. For more technical explanations of these terms, the interested reader is referred to the relevant CIE technical report [40].

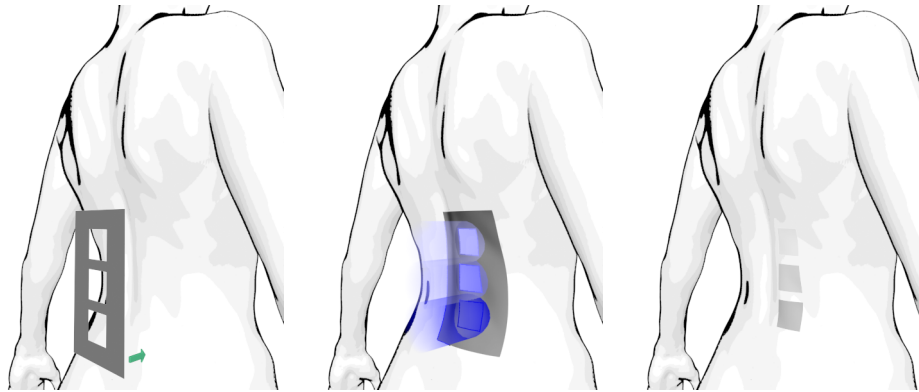


Figure 6.22: Artistic conception illustrating a standard experimental setup used for tanning experiments. A template is placed on the body (left) to isolate patches of skin in order to administer distinct measured UVR doses (centre). The changes in these patches relating to different exposure doses (right) are then recorded.

UVR [122], their appearance changes are less noticeable than those verified in specimens with lower constitutive pigmentation levels when subjected to the same exposure regime [147]. This behaviour is captured by the framework as illustrated in the images presented in Figure 6.25. More specifically, it can be observed that the higher the constitutive pigmentation (darker native appearance) of a given specimen, the less tanning it elicits. In fact, the weakest exposure dose schedule considered in our simulation is not sufficient to elicit a noticeable visible response in the darkest specimen (Figure 6.25 (right), top patch).

It is important to note that the increase in facultative pigmentation is more pronounced in individuals with high constitutive pigmentation levels than in those with low constitutive pigmentation levels when exposed to comparable UVR doses [122], *i.e.*, when subjected to doses proportional to their respective sensitivity to UVR (quantified in terms of MMD or MED). As a result, these individuals are considered to have a higher tanning ability [121, 143, 147]. This behaviour is also captured by the framework as illustrated in the images presented in Figure 6.26. These images were obtained by scaling the exposure doses applied to the specimens with intermediate and high constitutive pigmentation levels by factors of 1.4 and 2.4, respectively, according to their distinct sensitivities to UVR reported in experiments described in the scientific literature [160, 181]. As expected, the specimens with higher constitutive pigmentation levels show more noticeable appearance changes associated with stronger pigmentation build-ups.

It has also been demonstrated that different tanning abilities can be observed even among individuals with a similar level of constitutive pigmentation [161]. Accordingly, although individuals belonging to the SPT I, II, III and IV groups are all characterized by a low constitutive pigmentation level, SPT III and IV individuals have a higher tanning ability than the

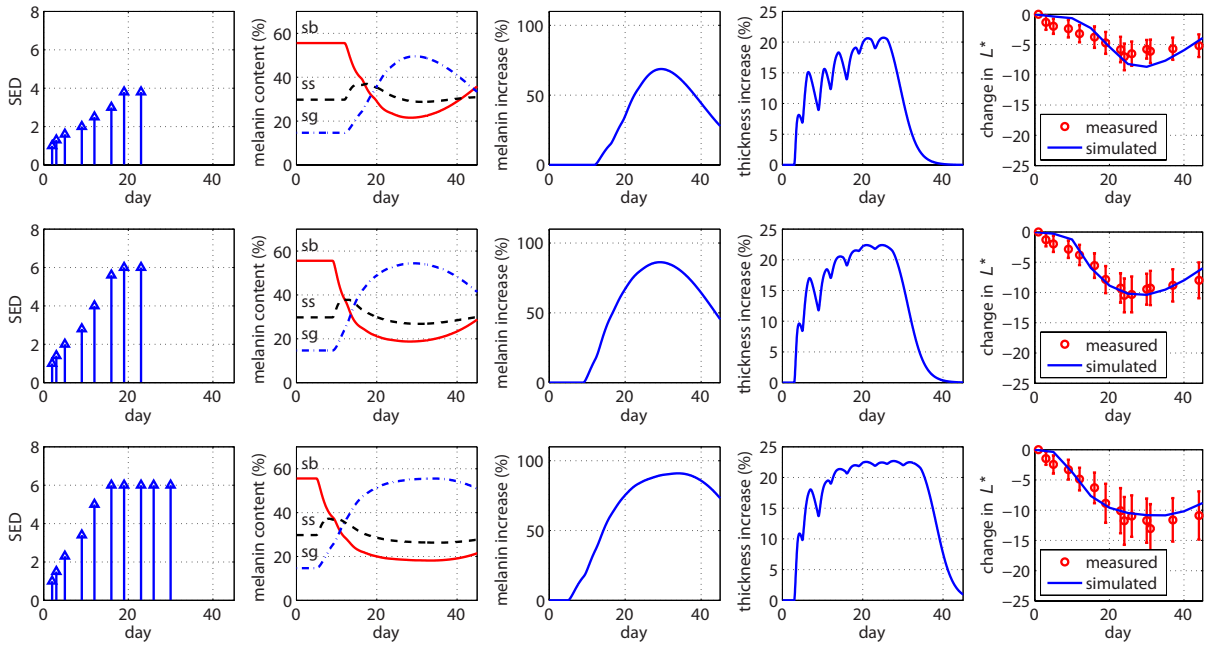


Figure 6.23: Simulated physiological changes resulting from three tanning processes triggered by three distinct UVR exposure dose schedules. First column: exposure dose schedules employed by Miller et al. [121]. Second column: changes in relative melanin content, which is associated with this pigment’s distribution in the different epidermal layers, namely stratum basale (sb), stratum spinosum (ss) and stratum granulosum (sg). Third column: changes in total melanin content. Fourth column: changes in skin thickness. Fifth column: comparisons of simulated results with measured values provided by Miller et al. [121]. These comparisons are presented in terms of the change in the lightness L^* coordinate of the $L^*a^*b^*$ colour space, with the bars depicting the standard deviations from the measured mean values.

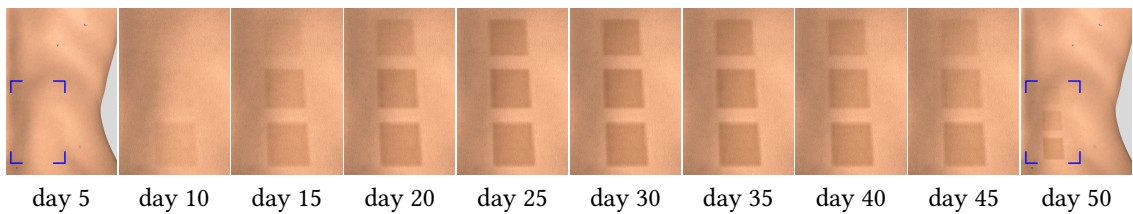


Figure 6.24: Sequence of images portraying the temporal changes in skin appearance as a result of the tanning processes described in Figure 6.23. The marked areas in the leftmost and rightmost images denote the boundaries of the in-between images. The top, middle and bottom tanned patches, in turn, correspond to the distinct exposure dose schedules provided in the top, middle and bottom rows of Figure 6.23, respectively.

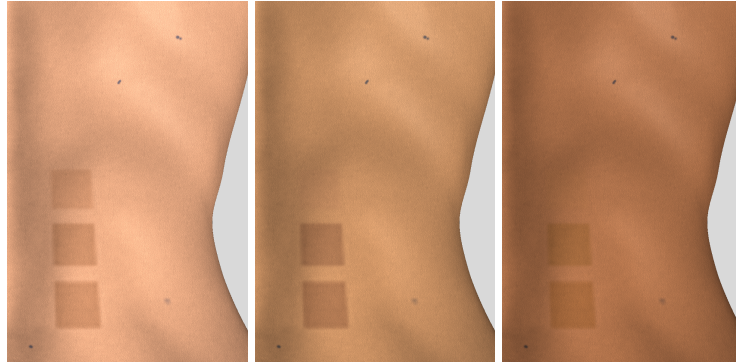


Figure 6.25: Images illustrating the distinct UVR sensitivities of specimens characterized by increasing levels of constitutive pigmentation, from low (left) to high (right). The same exposure dose schedules presented in Figure 6.23 were applied to the three specimens. The tanning responses depicted in the patches correspond to day 20, and they were obtained using the data provided in Tables 6.4 to 6.6.

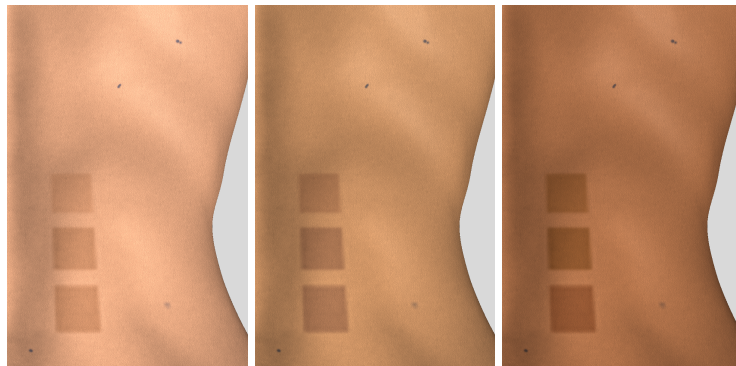


Figure 6.26: Images illustrating the different tanning abilities of specimens characterized by increasing levels of constitutive pigmentation, from low (left) to high (right). The same exposure dose schedules presented in Figure 6.23 were applied to three specimens. The tanning responses depicted in the patches correspond to day 20, and they were obtained using the data provided in Tables 6.4 to 6.6. We note that the UVR dose intensities were scaled by factors of 1.4 and 2.4 for the specimens with intermediate and high constitutive pigmentation levels respectively [160, 181].

others [111, 143]. These trends are illustrated by the images presented in Figures 6.27 and 6.28. These images show appearance changes resulting from tanning processes triggered by the same UVR exposure regime (30 SED) applied to two individuals with a low constitutive pigmentation level, but different tanning abilities. As a result, the individual with a high tanning ability shows a higher pigmentation build-up 15 days after exposure, which is particularly noticeable when one examines the appearance contrast provided by the tan lines left by the sunscreen (Figure 6.27 (right)). On the other hand, the individual with a mild tanning ability shows a lower pigmentation build-up 15 days after exposure, which can be observed by examining the appearance contrast between the untanned and tanned sides of her face (Figure 6.28 (bottom left)).

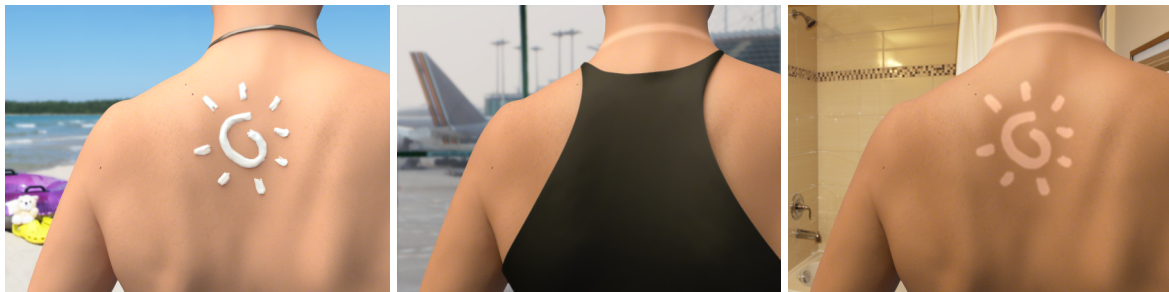


Figure 6.27: Sequence of images illustrating changes in the appearance of an individual with a high tanning ability. Left: initial appearance just before sunbathing for several hours with an effective sunscreen applied on her back as indicated. Centre: noticeable darkening on the way home inside an airport 4 days after UVR exposure. Right: significant darkening from a well developed tan as seen before taking a shower 15 days after exposure. To facilitate visual comparisons, the same illumination was used in the rendering of all three images. Note that these images were generated using the data provided in Tables 6.4 (dataset \mathcal{L} , with $m_{p,i,f}$ of the stratum basale set to 0.0858), 6.5 and 6.6.

Finally, the characteristic nonlinear appearance changes resulting from time-dependent tanning processes (triggered by a UVR exposure schedule equivalent to 30 SED) are further illustrated by an animation sequence whose main frames are presented in Figure 6.29. More specifically, one can notice a relatively rapid increase in pigmentation, reaching a broad maximum, which is then followed by a gradual fading. This behaviour is consistent with experimental observations on facultative pigmentation kinetics reported in the literature [26, 80, 158]. It is worth noting that apart from aesthetic aspects, facultative pigmentation fading is also of interest for biomedical applications since it represents the disappearance of natural photoprotection [159].

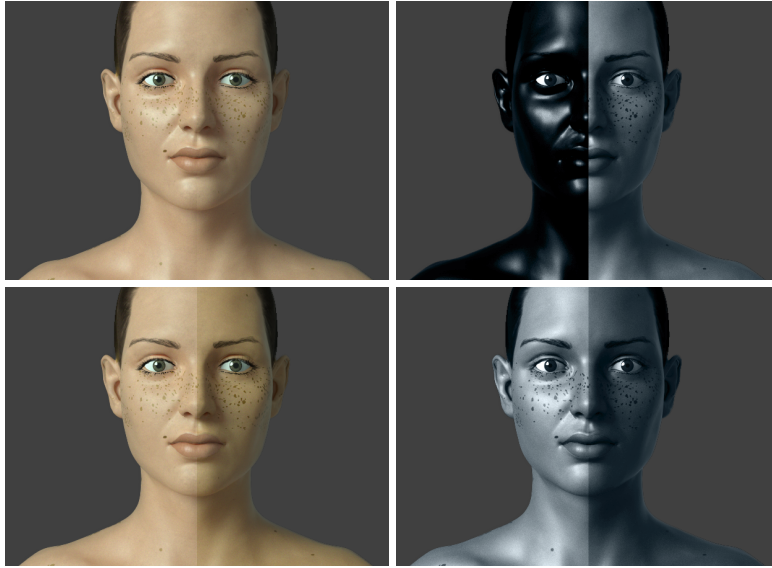


Figure 6.28: Images illustrating the visible skin appearance (left) and the corresponding UV appearance (right) of an individual with a mild tanning ability. The top row depicts the pre-exposure appearance with an effective sunscreen applied to one side of her face (depicting a glossier appearance). The bottom row depicts the appearance contrast between the untanned and tanned sides of her face 15 days after UVR exposure. Note that these images were generated using the data provided in Tables 6.4 (dataset \mathcal{L}), 6.5 and 6.6, and UV appearance attributes (at 365 nm) are depicted using pseudo colour.

6.2.3 Usability and Performance Issues

Recall that the two main components of the proposed framework, melanin and thickness dynamics, include a UVR dose evaluation step that requires the use of a light interaction model. Accordingly, the time spent on the execution of this step depends on the performance of the selected model. Apart from this step, however, the framework has a short throughput time. For instance, considering the execution of the two dynamics components of the framework using pre-computed values for the effectiveness of the UVR exposure doses, it takes less than a hundredth of a second on a 2.6 GHz dual-core Intel i5 CPU-based machine to compute the changes in biophysical parameters for a time period of a year at a temporal resolution of one hour. Hence, the incorporation of the framework into real-time visualization systems is viable, particularly taking into account that the computations for the UVR dose evaluation step can be performed offline, and their results accessed on demand during the simulations.

Similar to the HyLloS model, the proposed framework focuses on the accurate simulation of the tanning phenomenon which is controlled by biophysically meaningful parameters. As a

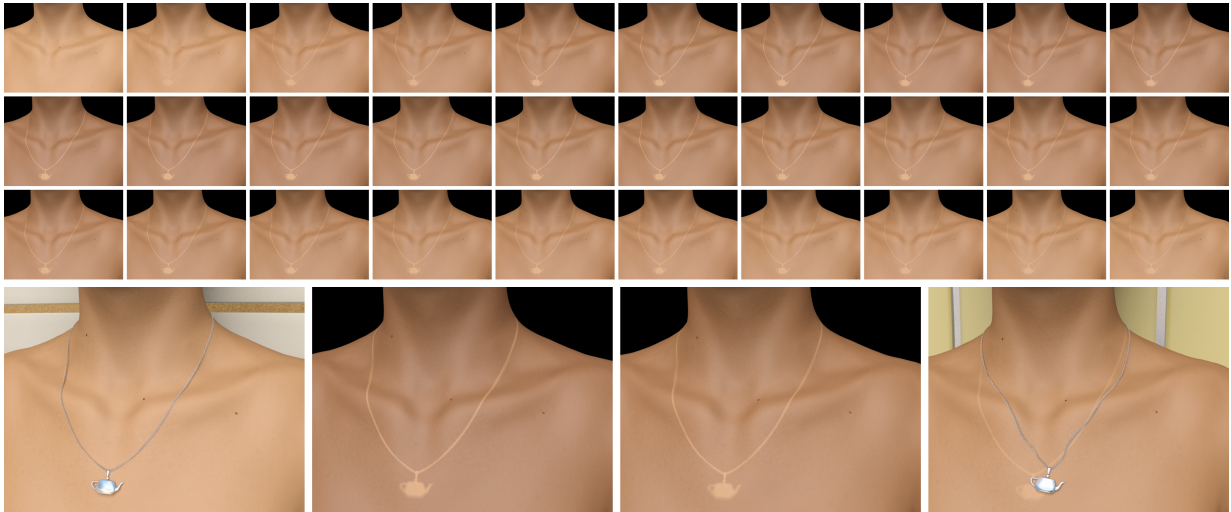


Figure 6.29: Frames from an animation illustrating nonlinear appearance changes of an individual over a period of 30 days resulting from an initial UVR exposure of several hours on a beach. The first three rows present frames (from left to right, top to bottom) depicting the sequence of daily tanning variations. The bottom row presents selected frames (from left to right) showing the initial pigmentation level at day 1, the peak pigmentation level at day 10 and faded pigmentation levels at days 20 and 30. Note that these frames were generated using the data provided in Tables 6.4 (dataset \mathcal{I}), 6.5 and 6.6.

result, these parameters cannot be directly translated to artist-guided controls for generalized features of the tanning phenomenon such as tan duration and intensity. Chapter 7 outlines plans to address this issue in the future.

7 Conclusion

Within computer graphics, one of the core areas of computer science, the modeling of material appearance plays a key role. Accordingly, it has been object of extensive research in the last decades. More recently, substantial efforts involving this line of research have been directed to overcome a major challenge, the realistic and predictive rendering of organic materials. Viewed in this context, the work presented in this thesis provides technical contributions to computer graphics and, by extension, to computer science. Moreover, by enabling the use of its outcomes to advance fundamental interdisciplinary investigations, it also contributes to the invigoration of the computer science research agenda. As appropriately stated by Priami [156], echoing previous statements by other eminent computer science scholars [101],

“ Augmenting the range of applicative domains taken from other fields is the main strategy for making computer science grow as a discipline, for improving the core themes developed so far, and for making it more accessible to a broader community. ”

Computer generated images usually portray materials in an idealized form within the visible spectral domain. However, the appearance of real materials, notably organic ones, changes over time due to invisible environmental stimuli. Accordingly, the development of algorithms capable of predictively accounting for such changes has been a pivotal element in enhancing the realism of current image synthesis systems. Furthermore, such systems present opportunities to address scientific problems that are beyond the abilities of a single discipline [108]. There has been an increasing number of research efforts that branch out into different fields as scientists are realizing the advantages that such cross fertilization presents [194]. We embraced this trend through a research endeavour with significant interdisciplinary ramifications, albeit being rooted in computer graphics, one of the most visible facets of computer science. Below, we summarize our contributions to and beyond computer graphics.

7.1 Contributions to Computer Graphics Research

We contributed to the field of computer graphics by expanding the spectral and temporal domains of material appearance modelling. More specifically, the original contributions of this work are as follows:

- We described the first skin appearance model designed for the comprehensive simulation of spectral and spatial distributions of light interacting with human skin from 250 *nm* to 2500 *nm*. We aimed to contribute to the realistic rendering of human skin for entertainment, aesthetic and educational purposes*. Accordingly, the predictive capabilities of the model were evaluated primarily through comparisons with measured data and experimental observations reported in the scientific literature.
- Through this model, we described the layered structure of the cutaneous tissues in more detail in comparison with existing skin appearance models. This enables it to appropriately generate skin appearance attributes, including the positional dependence of skin reflectance, in a more automated fashion than previous related works.
- We proposed the first physiologically-based temporal framework for the predictive simulation and visualization of skin tanning dynamics. This framework introduces to the computer graphics community UVR- and time-dependent algorithms for the predictive simulation of photobiological processes leading to characteristic changes in skin appearance attributes over time. As a result, it enables the generation of original image sequences depicting temporal tanning responses of different skin specimens subjected to distinct UVR exposure conditions.
- We designed this tanning simulation framework to have a modular architecture to allow for the seamless adjustment of its algorithms to accommodate application-specific requirements. For example, the rendering of virtual characters for entertainment applications often requires interactive frame rates. For these applications, as mentioned earlier, specific time-consuming tasks (*e.g.*, UVR dose evaluation) can be performed offline and their results incorporated into the simulations. Moreover, despite its comprehensive nature, the algorithms are amenable to straightforward implementation, which facilitates their incorporation into existing image synthesis pipelines without incurring a significant operational overhead.

*Please follow the link <http://www.npsg.uwaterloo.ca/resources/videos/Chen-HyLloS.mp4> to access the video containing relevant examples.

7.2 Contributions to Interdisciplinary Research

By addressing the predictive modelling of skin appearance attributes in the hyperspectral and temporal domains, we contribute not only to graphics applications, but also to potential interdisciplinary uses. The original contributions of this work beyond traditional graphics applications are as follows:

- We incorporated the particle nature and the different distribution patterns of the melanin-containing organelles into the HyLloS model. As such, phenomena such as detour and sieve effects affecting light absorption within the cutaneous tissues are accounted for. As a result, their incorporation into HyLloS can increase the reliability of biomedical applications based on accurate prediction of skin spectral properties through computer models. We remark that they have a strong impact in the UV and blue regions of the light spectrum where the light effects on skin physiological processes are more significant.
- We have contributed to the “culture of replication” that forms the foundation for progress within the computational sciences as well as the broader scientific community [124, 146]. More specifically, we made the HyLloS model publicly accessible so that independent parties can reproduce and verify the results presented in this thesis. This initiative also allows scientists from any discipline to use the HyLloS model for their own research without the need to understand the technical details of the underlying implementation. We achieved this by deploying a webpage where users can specify a customized set of input parameter values and remotely run the HyLloS model [126].
- We have proposed the first tanning simulation framework that enables the visualization of skin tanning phenomenon presented in the scientific literature. It can account for the UVR sensitivity of different skin types as well as arbitrary illumination conditions from different environments. To the best of our knowledge, the only other existing formulation for the simulation of tanning dynamics available in the scientific literature [184, 185] does not possess such capabilities and it addresses only melanin production.
- We developed tools that allow for further investigations in life and physical sciences. For example, the proposed light interaction model and tanning simulation framework can be used to obtain a more complete picture of the effects of various constituents on skin appearance and the adverse effects of UV exposure. Specific avenues for subsequent related work are outlined in the next section.

7.3 Future Research

Here, we outline directions for future work with respect to material appearance modelling and biomedical applications.

- Utilizing the proposed light interaction model to explore open questions in the life and physical sciences. For example, we plan to examine the effects of abnormal presence of melanin and bilirubin within the cutaneous tissues on skin spectral signatures. These studies may aid in the formulation and design of noninvasive or low cost screening procedures related to important medical conditions, namely jaundice and melanoma. These initiatives are expected to follow the same format as our investigation on abnormal skin hemoglobin content relevant for anemia [15] which was also performed using the proposed model.
- Expanding the proposed light interaction model to address the simulation of phenomena such as skin fluorescence, in which the energy of different wavelengths is not decoupled (as opposed to the energy decoupling assumption traditionally employed in image synthesis). Fluorescence remains a relatively unexplored area of material appearance modelling. Investigation of these phenomena would also have applications outside of graphics since the way a skin specimen fluoresces may provide information regarding its morphologic and biochemical characteristics [67].
- Expanding the proposed tanning simulation framework to be able to address other time- and spectrally-dependent skin phenomena. Within its current formulation, the framework does not account for highly transient and spectra-specific skin responses associated with UVR exposure. For example, soon after UVR exposure, skin might exhibit a subtle darkening that has been suggested to be a result of physicochemical processes [123]. Moreover, while the amount of energy carried by UVR at different wavelengths is accounted for by using action spectra, different wavelengths may nevertheless have diverse effects on distinct skin tissues. For example, it has been noted that UVB (280 nm to 320 nm) mainly affects the epidermal tissues, while UVA (320 nm to 400 nm) tends to affect blood vessels [39].
- Utilizing the proposed tanning simulation framework to contribute to additional theoretical and applied investigations outside of computer graphics. Examples include, but are not limited to, the evaluation of hypotheses about the photoprotection offered by different facultative pigmentation levels, the education of the general public about the harmful effects of excessive UVR exposure on skin health, and the *in silico* testing of products, such

as lotions and sunscreens, aimed at protecting individuals against these effects. These initiatives would introduce additional applications for the field of computer science to address, and, as a result, allows the field to expand its boundaries [156]. As outlined in the introduction, such initiatives are one of the primary motivations for this work.

- Examining strategies for incorporating the proposed light interaction model into real-time rendering frameworks by exploiting specialized graphics hardware and numerical reconstruction approaches based on the use of PCA and regression methods.
- Optimizing the parameter space of the proposed model and tanning simulation framework. For example, we believe future collaborations with artists and developers of material-appearance editing systems can help devise user interfaces and artist-guided controls tailored for production pipelines [168].
- Deploying the proposed tanning simulation framework online. This task would involve overcoming the technical issues relating to the flexibility in defining the framework's input (*e.g.*, skin tanning characteristics, exposure dose schedule, simulation time domain). Nevertheless, such an enterprise would be a valuable contribution to interdisciplinary research.

In closing, the simulation of light and skin interactions continues to pose significant challenges. Within computer graphics, we have yet to achieve complete predictive realism of virtual characters at interactive rates. Within health and medicine, we still do not fully understand the physiological relationship between light stimuli and skin changes. Although much progress has been made, we hope that the research presented in this thesis will contribute to strengthen the scientific foundation required for a deeper understanding of such topics and to serve as a catalyst for new far-reaching research developments within and outside computer graphics. As appropriately stated by one of the most influential computer graphics pioneers a long time ago, but still valid today:

“ The bad news is that we have still a long way to go.
The good news is that we have still a long way to go. ”

Alain Fournier
The Tiger Experience
Workshop on Rendering, Perception, and Measurement, 1999

References

- [1] AGACHE, P. Assessment of erythema and pallor. In *Measuring the Skin* (2004), P. Agache and P. Humbert, Eds., Springer, pp. 591–601.
- [2] AGACHE, P., AND HUMBERT, P. *Measuring the Skin*. Springer, 2004.
- [3] ALALUF, S., ATKINS, D., BARRET, K., BLOUNT, M., CARTER, N., AND HEATH, A. Ethnic variation in melanin content and composition in photoexposed and photoprotected human skin. *Pigment Cell & Melanoma Research* 15 (2002), 112–118.
- [4] ALTSHULER, G. B., ANDERSON, R. R., AND MANSTEIN, D. Method and apparatus for the selective targeting of lipid-rich tissues. Patent, 8 2003.
- [5] ANDERS, A., ALTHEIDE, H., KNÄLMANN, M., AND TRONNIER, H. Action spectrum for erythema in humans investigated with dye lasers. *Photochemistry and Photobiology* 61, 2 (1995), 200–205.
- [6] ANDERSON, R., AND PARRISH, J. The optics of human skin. *Journal of Investigative Dermatology* 77, 1 (1981), 13–9.
- [7] ANDERSON, R., AND PARRISH, J. Optical properties of human skin. In *The Science of Photomedicine* (N.Y., USA, 1982), J. Regan and J. Parrish, Eds., Plenum Press, pp. 147–194.
- [8] ANGELOPOULOU, E. Understanding the color of human skin. In *Storage and Retrieval for Image and Video Databases* (2001).
- [9] ATTAS, M., POSTHUMUS, T., SCHATTKA, B., SOWA, M., MANTSCH, H., AND ZHANG, S. Long-wavelength near-infrared spectroscopic imaging for in-vivo skin hydration measurements. *Vibrational Spectroscopy* 28 (2002), 37–43.
- [10] BARANOSKI, G. V. Modeling the interaction of infrared radiation (750 to 2500 nm) with bifacial and unifacial plant leaves. *Remote Sensing of Environment* 100, 3 (2006), 335–347.

- [11] BARANOSKI, G. V., AND CHEN, T. F. On the identification and interpretation of human skin spectral responses under adverse environmental conditions. In *IEEE Engineering in Medicine and Biology Society (EMBC), 37th International Conference of the* (August 2015), pp. 845–848.
- [12] BARANOSKI, G. V. G., AND CHEN, T. F. Optical properties of skin surface. In *Measuring the Skin*, P. Humbert, H. Maibach, and F. Fanian, Eds. Springer International Publishing, 2016, p. (in press).
- [13] BARANOSKI, G. V. G., CHEN, T. F., KIMMEL, B. W., MIRANDA, E., AND YIM, D. On the noninvasive optical monitoring and differentiation of methemoglobinemia and sulfhemoglobinemia. *Journal of Biomedical Optics* 17, 9 (2012), 097005–1–14.
- [14] BARANOSKI, G. V. G., CHEN, T. F., AND KRISHNASWAMY, A. Multilayer modeling of skin color and translucency. In *Computational Biophysics of the Skin*, B. Querleux, Ed. Pan Stanford Publishing, 2014, ch. 1.
- [15] BARANOSKI, G. V. G., DEY, A., AND CHEN, T. F. Assessing the sensitivity of human skin hyperspectral responses to increasing anemia severity levels. *Journal of Biomedical Optics* 20, 9 (September 2015), 095002–1–095002–14.
- [16] BARANOSKI, G. V. G., DIMSON, T., CHEN, T. F., KIMMEL, B., YIM, D., AND MIRANDA, E. Rapid dissemination of light transport models on the web. *IEEE Computer Graphics & Applications* 32 (2012), 10–15.
- [17] BARANOSKI, G. V. G., KIMMEL, B. W., CHEN, T. F., AND MIRANDA, E. Assessing the spectral sensitivity of martian terrains to iron oxide variations using the SPLITS model. *IEEE Journal of Selected Topics in Applied Earth Observations and Remote Sensing* (2015), 3404–3413.
- [18] BARANOSKI, G. V. G., AND KRISHNASWAMY, A. *Light & Skin Interactions: Simulations for Computer Graphics Applications*. Morgan Kaufmann/Elsevier, Burlington, MA, USA, 2010.
- [19] BARSLEY, R. E., WEST, M. H., AND FAIR, J. A. Forensic photography: Ultraviolet imaging of wounds on skin. *American Journal of Forensic Medicine & Pathology* 11, 4 (December 1990), 300–308.
- [20] BASHKATOV, A. N., GENINA, E. A., KOCHUBEY, V. I., STOLNITZ, M. M., BASHKATOVA, T. A., NOVIKOVA, O. V., PESHKOVA, A. Y., AND TUCHIN, V. V. Optical properties of melanin in the skin and skinlike phantoms. In *Controlling Tissue Optical Properties: Applications in Clinical Study* (2000), V. V. Tuchin, Ed., vol. 4162, SPIE, pp. 219–226.

- [21] BELL, I., AND BARANOSKI, G. Reducing the dimensionality of plant spectral databases. *IEEE Transactions on Geoscience and Remote Sensing* 42, 3 (March 2004), 57–577.
- [22] BENDIT, E. G., AND ROSS, D. A technique for obtaining the ultraviolet absorption spectrum of solid keratin. *Applied Spectroscopy* (1961).
- [23] BICKEL, B., KAUFMANN, P., SKOURAS, M., THOMASZEWSKI, B., BRADLEY, D., BEELER, T., MARSCHNER, S., MATUSIK, W., AND GROSS, M. Face cloning. *ACM Transactions on Graphics* 31, 4 (2012), 118:1–118:10.
- [24] BLANK, I. Factors which influence the water content of the stratum corneum. *Journal of Investigative Dermatology* 18, 6 (06 1952), 433–440.
- [25] BOISSIEUX, L., KISS, G., MAGNENAT-THALMANN, N., AND KALRA, P. Simulation of skin aging and wrinkles with cosmetic insight. In *Computer Animation and Simulation* (2000), N. Magnenat-Thalmann, D. Thalmann, and B. Arnaldi, Eds., Springer-Verlag, pp. 15–27.
- [26] BRENNER, M., AND HEARING, V. The protective role of melanin against UV damage in human skin. *Photochemistry and Photobiology* 84, 3 (2008), 539–549.
- [27] BROGGI, A., FEDRIGA, R., AND TAGLIATI, A. Pedestrian detection on a moving vehicle: an investigation about near infra-red images. In *Intelligent Vehicles Symposium, 2006 IEEE* (2006), pp. 431–436.
- [28] BRULS, W. G., AND VAN DER LEUN, J. Forward scattering properties of human epidermal layers. *Photochemistry and Photobiology* 40, 2 (1984), 231–242.
- [29] BUTLER, W. Absorption spectroscopy *in vivo*: theory and application. *Annual Review of Plant Physiology* 15 (1964), 451–470.
- [30] CAVALCANTI, P. G., SCHARCANSKI, J., AND BARANOSKI, G. V. G. A two-stage approach for discriminating melanocytic skin lesions using standard cameras. *Expert Systems with Applications* 40, 10 (2013), 4054–4064.
- [31] CERUSSI, A. E., BERGER, A. J., BEVILACQUA, F., SHAH, N., JAKUBOWSKI, D., BUTLER, J., HOLCOMBE, R. F., AND TROMBERG, B. J. Sources of absorption and scattering contrast for near-infrared optical mammography. *Academic Radiology* 8, 3 (March 2001), 211–218.
- [32] CHEDEKEL, M. Photophysics and photochemistry of melanin. In *Melanin: Its Role in Human Photoprotection* (Overland Park, Kansas, USA, 1995), M. C. L. Zeise and T. Fitzpatrick, Eds., Valdenmar Publishing Co., pp. 11–22. 2223b.

- [33] CHEN, B., STAMNES, K., AND STAMNES, J. Validity of the diffusion approximation in bio-optical imaging. *Applied Optics* 40, 34 (2001), 6356–6336.
- [34] CHEN, T., BARANOSKI, G., KIMMEL, B., AND MIRANDA, E. Hyperspectral modeling of skin appearance. *ACM Transactions on Graphics* 34, 3 (2015), 31:1–31:14.
- [35] CHEN, T. F., AND BARANOSKI, G. V. Effective compression and reconstruction of human skin hyperspectral reflectance databases. In *IEEE Engineering in Medicine and Biology Society (EMBC), 37th International Conference of the* (August 2015), pp. 7027–7030.
- [36] CHEN, T. F., AND BARANOSKI, G. V. Melanosome distribution patterns affecting skin reflectance: Implications for the in vivo estimation of epidermal melanin content. In *IEEE Engineering in Medicine and Biology Society (EMBC), 37th International Conference of the* (August 2015), pp. 4415–4418.
- [37] CHEN, Y., XIA, L., WONG, T., BAO, H., GUO, B., AND SHUM, H. Visual simulation of weathering by γ -ton tracing. *ACM Transactions on Graphics* 24, 3 (2005), 1127–1133.
- [38] CLENDENING, B. UV spectrophotometric analysis of DNA and RNA. Tech. rep., Hofstra University, 2002.
- [39] CLYDESDALE, G., DANDIE, G., AND KONRAD, H. M. Ultraviolet light induced injury: Immunological and inflammatory effects. *Immunology & Cell Biology* 79, 6 (2001), 547– 568.
- [40] COMMISSION INTERNATIONALE DE L’ECLAIRAGE. ILV: International lighting vocabulary, new. Tech. Rep. CIE S 017/E:2011, CIE Central Bureau, Kegelgasse 27, A-1030 Vienna, Austria, 2011.
- [41] COOKSEY, C., AND ALLEN, D. Reflectance measurements of human skin from the ultraviolet to the shortwave infrared (250 nm to 2500 nm). In *SPIE Vol. 8734, Active and Passive Signatures IV* (2013), G. Gilbreath and C. Hawley, Eds., pp. 87340N–1–9.
- [42] COOKSEY, C., TSAI, B., AND ALLEN, D. A collection and statistical analysis of skin reflectance for inherent variability over the 250 nm to 2500 nm spectral range. In *SPIE Vol. 9082, Active and Passive Signatures IV* (2014), G. Gilbreath and C. Hawley, Eds., pp. 908206–1–11.
- [43] CUNNINGTON, A. J., KENDRICK, S. F. W., WAMOLA, B., LOWE, B., AND NEWTON, C. R. J. C. Carboxyhemoglobin levels in Kenyan children with plasmodium falciparum malaria. *The American Journal of Tropical Medicine and Hygiene* 71, 1 (2004), 43–47.

- [44] DE GRAAFF, K. V. *Human Anatomy*, 4th ed. W. C. Brown Publishers, Dubuque, IO, USA, 1995.
- [45] DELPY, D., COPE, M., ZEE, P., WRAY, S., AND WYATT, J. Estimation of the optical pathlength through tissue from direct flight measurement. *Physics in Medicine and Biology* 33, 12 (1988), 1433–1442.
- [46] D’EON, E., AND IRVING, G. A quantized-diffusion model for rendering translucent materials. *ACM Transactions on Graphics* 30, 4 (2011), 56:1–13.
- [47] D’EON, E., LUEBKE, D., AND ENDERTON, E. Efficient rendering of human skin. In *18th Eurographics Workshop on Rendering* (June 2007), pp. 147–158.
- [48] DIFFEY, B. A mathematical model for ultraviolet optics in skin. *Physics in Medicine and Biology* 28, 6 (1983), 647–657.
- [49] DIFFEY, B. L. Ultraviolet radiation physics and the skin. *Physics in Medicine and Biology* 25, 3 (1980), 405.
- [50] DONNER, C., AND JENSEN, H. W. A spectral BSSRDF for shading human skin. In *17th Eurographics Workshop on Rendering* (2006), pp. 409–418.
- [51] DONNER, C., WEYRICH, T., D’EON, E., RAMAMOORTHY, R., AND RUSINKIEWICZ, S. A layered, heterogeneous reflectance model for acquiring and rendering human skin. *ACM Transactions on Graphics* 27, 5 (2008), 140:1–12.
- [52] DORONIN, A., AND MEGLINSKI, I. Online object oriented Monte Carlo computational tool for needs of the biomedical optics. *Biomedical Optics Express* 2, 9 (2011), 2461–2469.
- [53] DORSEY, J., PEDERSEN, H., AND HANRAHAN, P. Flow and changes in appearance. In *ACM SIGGRAPH* (1996), pp. 411–420.
- [54] DORSEY, J., RUSHMEIER, H., AND SILLION, F. *Digital Modeling of Material Appearance*. Morgan Kaufmann/Elsevier, Burlington, MA, USA, 2007.
- [55] FEDERICI, J. F., GUZELSU, N., LIM, H. C., JANNUZZI, G., FINDLEY, T., CHAUDHRY, H. R., AND RITTER, A. B. Noninvasive light-reflection technique for measuring soft-tissue stretch. *Applied Optics* 38, 31 (Nov 1999), 6653–6660.
- [56] FLEWELLING, R. Noninvasive optical monitoring. In *The Biomedical Engineering Handbook*, J. D. Bronzino, Ed., 2 ed. CRC Press LLC, 2000.

- [57] FLINDT, R. *Amazing Numbers in Biology*. Springer, 2006.
- [58] FOLEY, J., VAN DAM, A., FEINER, S., AND HUGHES, J. *Computer Graphics: Principles and Practice*, second ed. Addison-Wesley Publishing Company, Reading, MA, USA, 1990.
- [59] FREDEMBACH, C., BARBUSCLA, N., AND SÜSTRUNK, S. Combining visible and near-infrared images for realistic skin smoothing. In *17th Color and Imaging Conference (2009)*, pp. 242–247.
- [60] FUCHS, E. Keratins and the skin. *Annual Review of Cell and Developmental Biology* 11, 1 (1995), 123–154.
- [61] FUCHS, M., BLANZ, V., LENSCH, H., AND SEIDEL, H. Reflectance from images: a model-based approach for human faces. *IEEE Transactions on Visualization and Computer Graphics* 11, 3 (2005), 296–305.
- [62] FUKSHANSKY, L. Absorption statistics in turbid media. *Journal of Quantitative Spectroscopy and Radiative Transfer* 38 (1987), 389–406.
- [63] FULTON, J. Utilizing the ultraviolet (UV detect) camera to enhance the appearance of photodamage and other skin conditions. *Dermatologic Surgery* 23 (1997), 163–169.
- [64] GAWKRODGER, D. J. *Dermatology An Illustrated Colour Text*. Churchill Livingstone, 2002.
- [65] GHOSH, A., HAWKINS, T., PEERS, P., FREDERIKSEN, S., AND DEBEVEC, P. Practical modeling and acquisition of layered facial reflectance. *ACM Transactions on Graphics* 27, 5 (2008), 139:1–10.
- [66] GILCHREST, B., PARK, H., ELLER, M., AND YAAR, M. Mechanisms of ultraviolet light-induced pigmentation. *Photochemistry and Photobiology* 63, 1 (1996), 1–10.
- [67] GILLIES, R., ZONIOS, G., ANDERSON, R. R., AND KOLLIAS, N. Fluorescence excitation spectroscopy provides information about human skin in vivo. *The Journal of Investigative Dermatology* 115, 4 (10 2000), 704–707.
- [68] GOLUB, G., AND LOAN, C. V. *Matrix Computations*, 2nd ed. John Hopkins University Press, Baltimore, MD, USA, 1989.
- [69] GOUTELLE, S., MAURIN, M., ROUGIER, F., BARBAUT, X., BOURGUIGNON, L., DUCHER, M., AND MAIRE, P. The Hill equation: a review of its capabilities in pharmacological modelling. *Fundamental & Clinical Dermatology* 22 (2008), 633–648.

- [70] GREENBERG, D., ARVO, J., LAFORTUNE, E., TORRANCE, K., FERWERDA, J., WALTER, B., TRUMBORE, B., SHIRLEY, P., PATTANAIK, S., AND FOO, S. A framework for realistic image synthesis. In *SIGGRAPH, Annual Conference Series* (1997), pp. 477–494.
- [71] GREENBERG, D. P. 1987 Steven A. Coons Award Lecture. *SIGGRAPH Computer Graphics* 22, 1 (Feb. 1988), 7–14.
- [72] GROSS, D. C. Report from the fidelity implementation study group. In *Simulation Interoperability Workshop*. Simulation Interoperability and Standards Organization, 1999.
- [73] GU, J., TU, C., RAMAMOORTHI, R., BELHUMEUR, P., MATUSIK, W., AND NAYAR, S. Time-varying surface appearance: Acquisition, modeling and rendering. *ACM Transactions on Graphics* 25, 3 (2006), 762–771.
- [74] HAMBY, D. A review of techniques for parameter sensitivity analysis of environmental models. *Environmental Monitoring and Assessment* 32 (1994), 135–154.
- [75] HAMBY, D. A comparison of sensitivity analysis techniques. *Health Physics* 68 (1995), 195–204.
- [76] HAMMERSLEY, J. M., AND HANDSCOMB, D. C. *Monte Carlo Methods*. Methuen, London, 1964.
- [77] HANRAHAN, P., AND KRUEGER, W. Reflection from layered surfaces due to subsurface scattering. In *SIGGRAPH, Annual Conference Series* (August 1993), pp. 165–174.
- [78] HANSEN, M., ATKINSON, G., SMITH, L., AND SMITH, M. 3D face reconstructions from photometric stereo using near infrared and visible light. *Computer Vision and Image Understanding* 114 (2010), 942–951.
- [79] HARDEBERG, J. *Acquisition and Reproduction of Color Images: Colorimetric and Multispectral Approaches*. Dissertation.com, USA, 2001.
- [80] HAWK, J., AND PARRISH, J. A. Responses of normal skin to ultraviolet radiation. In *The Science of Photomedicine*, J. D. Regan and J. A. Parrish, Eds. Plenum Press, 1982, ch. 8.
- [81] HAYMOND, S., CARIAPPA, R., EBY, C. S., AND SCOTT, M. G. Laboratory assessment of oxygenation in methemoglobinemia. *Clinical Chemistry* 51, 2 (2005), 434–444.
- [82] HENNESSY, A., OH, C., DIFFEY, B., WAKAMATSU, K., ITO, S., AND REES, J. Eumelanin and pheomelanin concentrations in human epidermis before and after UVB irradiation. *Pigment Cell & Melanoma Research* 18 (2005), 220–223.

- [83] HIELSCHER, A., JACQUES, S., WANG, L., AND TITTEL, F. The influence of boundary conditions on the accuracy of diffusion theory in time-resolved reflectance spectroscopy of biological tissues. *Physics in Medicine and Biology* 40 (1995), 1957–1975.
- [84] HUANG, H., AND ANTONELLI, P. Application of principal component analysis to high-resolution infrared measurement compression and retrieval. *Journal of Applied Meteorology and Climatology* 40 (March 2001), 365–388.
- [85] HUNTER, R., AND HAROLD, R. *The Measurement of Appearance*, second ed. John Wiley & Sons, New York, NY, USA, 1987.
- [86] IGARASHI, T., NISHINO, K., AND NAYAR, S. K. The appearance of human skin: A survey. *Foundations and Trends in Computer Graphics and Vision* 3 (January 2007), 1–95.
- [87] IGLESIAS-GUITIAN, J., ALIAGA, C., JARABO, A., AND GUTIERREZ, D. A biophysically-based model of the optical properties of skin aging. *Computer Graphics Forum* 34, 2 (2015), 45–55.
- [88] INTERNATIONAL PROGRAMME ON CHEMICAL SAFETY. Environmental health criteria (EHC) 160: Ultraviolet radiation. Tech. rep., World Health Organization, 1994.
- [89] JACQUES, S., AND MCAULIFFE, D. The melanosome: threshold temperature for explosive vaporization and internal absorption coefficient during pulsed laser irradiation. *Journal of Photochemistry and Photobiology B: Biology* 53, 6 (1991), 769–775.
- [90] JACQUES, S. L. Origins of tissue optical properties in the UVA, visible, and NIR regions. *Advances in Optical Imaging and Photon Migration* 2 (1996), 364–369.
- [91] JACQUES, S. L. Optical absorption of melanin. Tech. rep., Oregon Medical Laser Center, 2001.
- [92] JACQUES, S. L., ALTER, C. A., AND PRAHL, S. A. Angular dependence of HeNe laser light scattering by human dermis. *Lasers in the Life Sciences* 1 (1987), 309–333.
- [93] JACQUEZ, J., HUSS, J., MCKEEHAN, W., DIMITROFF, J., AND KUPPENHEIN, H. Spectral reflectance of human skin in the region 0.7-2.6 μ . *Journal of Applied Physiology* 8 (1955), 297–299.
- [94] JACQUEZ, J., HUSS, J., MCKEEHAN, W., DIMITROFF, J., AND KUPPENHEIN, H. Spectral reflectance of human skin in the region 235-700 m μ . *Journal of Applied Physiology* 8 (1955), 212–214.

- [95] JIMENEZ, J., SCULLY, T., BARBOSA, N., DONNER, C., ALVAREZ, X., VIEIRA, T., MATTS, P., ORVALHO, V., GUTIERREZ, D., AND WEYRICH, T. A practical appearance model for dynamic facial color. *ACM Transactions on Graphics* 29, 6 (2010), 141:1–10.
- [96] JIMENEZ, J., SUNDSTEDT, V., AND GUTIERREZ, D. Screen-space perceptual rendering of human skin. *ACM Transactions on Applied Perception* 6, 4 (2009), 23:1–15.
- [97] JOLLIFFE, I. *Principal Component Analysis*, 2nd ed. Springer-Verlag, New York, 2002. pages 44-46.
- [98] KIM, M. H., HARVEY, T. A., KITTLE, D. S., RUSHMEIER, H., DORSEY, J., PRUM, R., AND BRADY, D. 3D Imaging spectroscopy for measuring hyperspectral patterns on solid objects. *ACM Transactions on Graphics* 31, 4 (2012), 38:1–11.
- [99] KIMMEL, B., BARANOSKI, G., CHEN, T., YIM, D., AND MIRANDA, E. Spectral appearance changes induced by light exposure. *ACM Transactions on Graphics* 32, 1 (2013), 10:1–10:13.
- [100] KIMMEL, B. W., AND BARANOSKI, G. V. G. A novel approach for simulating light interaction with particulate materials: application to the modeling of sand spectral properties. *Optics Express* 15, 15 (2007), 9755–9777.
- [101] KLAWE, M., AND SHNEIDERMAN, B. Crisis and opportunity in computer science. *Communications of the ACM* 48, 11 (Nov. 2005), 27–28.
- [102] KOLLIAS, N., AND BAQER, A. On the assessment of melanin in human skin *in vivo*. *Journal of Photochemistry and Photobiology B: Biology* 43, 1 (1986), 49–54.
- [103] KOLLIAS, N., SAYRE, R. M., ZEISE, L., AND CHEDEKEL, M. R. Photoprotection by melanin. *Journal of Photochemistry and Photobiology B: Biology* 9, 2 (1991), 135–60.
- [104] KRISHNASWAMY, A., AND BARANOSKI, G. V. G. A biophysically-based spectral model of light interaction with human skin. *Computer Graphics Forum* 23, 3 (2004), 331–340.
- [105] KRISHNASWAMY, A., AND BARANOSKI, G. V. G. Combining a shared-memory high performance computer and a heterogeneous cluster for the simulation of light interaction with human skin. In *16th Symposium on Computer Architecture and High Performance Computing* (Washington, USA, 2004), P. N. J. Gaudiot, M.L. Pilla and S. Song, Eds., IEEE Computer Society, pp. 166–171.
- [106] KUBELKA, P., AND MUNK, F. Ein beitrage zur optik der farbanstriche. *Zeitschrift für technische Physik* 12 (1931), 543.

- [107] LATIMER, P. A wave-optics effect which enhances light absorption by chlorophyll *in vivo*. *Photochemistry and Photobiology* 40, 2 (1984), 193–199.
- [108] LEDFORD, H. How to solve the world’s biggest problems. *Nature* 525, 7569 (September 2015), 308–311.
- [109] LEE, R., MATHEWS-ROTH, M. M., PATHAK, M. A., AND PARRISH, J. A. The detection of carotenoid pigments in human skin. *Journal of Investigative Dermatology* 64, 3 (03 1975), 175–177.
- [110] LISTER, T. S. *Simulating the Color of Port Wine Stain Skin*. PhD thesis, University of Southampton, U.K., February 2013.
- [111] LOCK-ANDERSEN, J., KNUDSTORP, N., AND WULF, H. Facultative skin pigmentation in Caucasians: an objective biological indicator of lifetime exposure to ultraviolet radiation? *British Journal of Dermatology* 138 (1998), 826–832.
- [112] LOPEZ, H., BEER, Z., MILLER, S., AND ZMUDZKA, B. Ultrasound measurements of skin thickness after UV exposure: a feasibility study. *Journal of Photochemistry and Photobiology B: Biology* 73, 3 (2004), 123–132.
- [113] LOVELL, A. T., HEBDEN, J. C., GOLDSTONE, J. C., AND COPE, M. Determination of the transport scattering coefficient of red blood cells. In *Proc. SPIE 3597, Optical Tomography and Spectroscopy of Tissue III* (1999), vol. 3597, pp. 175–182.
- [114] MAGNENAT-THALMANN, N., KALRA, P., L. LEVEQUE, J., BAZIN, R., BATISSE, D., AND QUERLEUX, B. A computational skin model: fold and wrinkle formation. *IEEE Transactions on Information Technology in Biomedicine* 6, 4 (2002), 317–323.
- [115] MAHLER, H., KULIK, J., GIBBONS, F., GERRAD, M., AND HARREL, J. Effects of appearance-based interventions on sun protection intentions and self-reported behaviors. *Health Psychology* 22, 2 (2003), 199–209.
- [116] MARSCHNER, S., WESTIN, S. H., LAFORTUNE, E., TORRANCE, K., AND GREENBERG, D. Reflectance measurements of human skin. Tech. Rep. PCG-99-2, Program of Computer Graphics, Cornell University, USA, January 1999.
- [117] MCCARTNEY, E. J. *Optics of the atmosphere: Scattering by molecules and particles*. John Wiley & Sons, New York, NY, USA, 1976.
- [118] MCKINLAY, A., AND DIFFEY, B. A reference action spectrum for ultraviolet induced erythema in human skin. *CIE Journal* 6, 1 (1987), 17–22.

- [119] MÉRILLOU, S., AND GHAZANFARPOUR, D. A survey of aging and weathering phenomena in computer graphics. *Computers & Graphics* 32, 2 (2008), 159–174.
- [120] MEYER-ARENDET, J. *Introduction to Modern and Classical Optics*. Prentice-Hall, New Jersey, 1984.
- [121] MILLER, S., COELHO, S., MILLER, S., YAMAGUCHI, Y., HEARING, V., AND BEER, J. Evidence for a new paradigm for ultraviolet exposure: a universal schedule that is skin phototype independent. *Photodermatology, Photoimmunology & Photomedicine* 28, 4 (2012), 187–195.
- [122] MILLER, S., COELHO, S., ZMUDZKA, B., AND BEER, J. Reduction of the UV burden to indoor tanners through new exposure schedules: a pilot study. *Photodermatology, Photoimmunology & Photomedicine* 22, 2 (2006), 59–66.
- [123] MIYAMURA, Y., COELHO, S., WOLBER, R., MILLER, S., WAKAMATSU, K., ZMUDZKA, B., ITO, S., SMUDA, C., PASSERON, T., CHOI, W., BATZER, J., YAMAGUCHI, Y., BEER, J., AND HEARING, V. Regulation of human skin pigmentation and responses to ultraviolet radiation. *Pigment Cell & Melanoma Research* 20, 1 (2006), 2–13.
- [124] MORIN, A., URBAN, J., ADAMS, P. D., FOSTER, I., SALI, A., BAKER, D., AND SLIZ, P. Shining light into black boxes. *Science* 336, 6078 (April 2012), 159–160.
- [125] NAKAGAWA, N., MATSUMOTO, M., AND SAKAI, S. *In vivo* measurement of the water content in the dermis by confocal Raman spectroscopy. *Skin Research and Technology* 16, 2 (2010), 137–141.
- [126] NATURAL PHENOMENA SIMULATION GROUP (NPSG). *Run HyLloS Online*. School of Computer Science, University of Waterloo, Ontario, Canada, 2014. <http://www.npsg.uwaterloo.ca/models/hyllos.php>.
- [127] NEWELL, W. H. A theory of interdisciplinary studies. *ISSUES IN INTEGRATIVE STUDIES* 19 (2001), 1–25.
- [128] NG, C., AND LI, L. A multi-layered reflection model of natural human skin. In *Computer Graphics International* (Hong Kong, July 2001), pp. 249–256.
- [129] NICODEMUS, F., RICHMOND, J., HSIA, J., GINSBERG, I., AND LIMPERIS, T. Geometrical considerations and nomenclature for reflectance. In *Physics-Based Vision Principles and Practice: Radiometry* (Boston, 1992), L. Wolff, S. Shafer, and G. Healey, Eds., Jones and Bartlett Publishers, pp. 94–145.

- [130] NIELSEN, K., ZHAO, L., STAMNES, J., STAMNES, K., AND MOAN, J. Reflectance spectra of pigmented and nonpigmented skin in the UV spectral region. *Photochemistry and Photobiology* 80 (2004), 450–455.
- [131] NIELSEN, K. P., ZHAO, L., STAMNES, J. J., STAMNES, K., AND MOAN, J. The importance of the depth distribution of melanin in skin for DNA protection and other photobiological processes. *Journal of Photochemistry and Photobiology B: Biology* 82, 3 (2006), 194–198.
- [132] NUNEZ, A., AND MENDENHALL, M. Detection of human skin in near infrared hyperspectral imagery. In *Geoscience and Remote Sensing Symposium, 2008. IGARSS 2008. IEEE International* (July 2008), vol. 2, pp. II-621 –II-624.
- [133] NUNEZ, A. S. *A Physical Model of Human Skin and Its Application for Search and Rescue*. PhD thesis, Air Force Institute of Technology, Wright-Patterson Air Force Base, Ohio, USA, December 2009.
- [134] NUNEZ, A. S., MENDENHALL, M. J., AND GROSS, K. Melanosome level estimation in human skin from hyperspectral imagery. In *First Workshop on Hyperspectral Image and Signal Processing: Evolution in Remote Sensing - WHISPERS* (2009).
- [135] OLIVARIUS, F. F., WULF, H. C., THERKILDSEN, P., POULSEN, T., CROSBY, J., AND NORVAL, M. Urocanic acid isomers: relation to body site, pigmentation, stratum corneum thickness and photosensitivity. *Archives of Dermatological Research* 289 (1997), 501–505.
- [136] OLSON, R. L., GAYLOR, J., AND EVERETT, M. A. Skin color, melanin, and erythema. *Archives of Dermatology* 108, 4 (1973), 541–544.
- [137] OUDHIA, A. UV-VIS spectroscopy as a nondestructive and effective characterization tool for II-VI compounds. *Recent Research in Science and Technology* 4, 8 (2012), 109–111.
- [138] PADOAN, R., STEEMERS, T., KLEIN, M., AALDERINK, B., AND DE BRUIN, G. Quantitative hyperspectral imaging of historical documents: Technique and applications. In *9th International Conference on NDT of Art* (May 2008).
- [139] PALMER, K. F., AND WILLIAMS, D. Optical properties of water in the near infrared. *Journal of the Optical Society of America* 64, 8 (Aug 1974), 1107–1110.
- [140] PAMPLONA, V., OLIVEIRA, M., AND BARANOSKI, G. Photorealistic models for pupil light reflex and iridal pattern deformation. *ACM Transactions on Graphics* 28 (2009), 106:1–106:12.

- [141] PARRISH, J., JAENICKE, K., AND ANDERSON, R. Erythema and melanogenesis action spectra of normal human skin. *Photochemistry and Photobiology* 36, 2 (1982), 187–191.
- [142] PARTRIDGE, M., AND CALVO, R. Fast dimensionality reduction and simple pca. *Intelligent Data Analysis* 2, 3 (1998), 1–14.
- [143] PATHAK, M. Functions of melanin and protection by melanin. In *Melanin: Its Role in Human Photoprotection* (Overland Park, Kansas, USA, 1995), M. C. L. Zeise and T. Fitzpatrick, Eds., Valdenmar Publishing Co., pp. 125–134.
- [144] PAUWELS, M., AND ROGIERS, V. Safety evaluation of cosmetics in the EU. reality and challenges for the toxicologist. *Toxicology Letters* 151, 1 (2004), 7–17.
- [145] PEARSE, A., GASKELL, S., AND MARKS, R. Epidermal changes in human skin following irradiation with either UVB or UVA. *Journal of Investigative Dermatology* 88, 1 (1987), 83–87.
- [146] PENG, R. D. Reproducible research in computational science. *Science* 334, 6060 (2011).
- [147] PEZIC, A., PONSONBY, A., CAMERON, F., RODDA, C., ELLIS, J., HALLIDAY, J., SIERO, W., LUCAS, R., AND DWYER, T. Constitutive and relative facultative skin pigmentation among Victorian children including comparison of two visual skin charts for determining constitutive melanin density. *Photochemistry and Photobiology* 89 (2013), 714–723.
- [148] PLEWIG, G., SCHEUBER, E., REUTER, B., AND WAIDELICH, W. Thickness of corneocytes. In *Stratum Corneum*, R. Marks and G. Plewig, Eds. Springer-Verlag, Berlin, 1983.
- [149] POON, T., KUCHEL, J., BADRUDDIN, A., HALLIDAY, G., BARNETSON, R., IWAKI, H., AND HATAO, M. Objective measurement of minimal erythema and melanogenic doses using natural and solar-simulated light. *Photochemistry and Photobiology* 78, 4 (2003), 331–336.
- [150] POPE, R., AND FRY, E. Absorption spectrum (380–700 nm) of pure water. II. Integrating cavity measurements. *Applied Optics* 36, 33 (Nov 1997), 8710–8723.
- [151] PRAHL, S. *Light Transport in Tissue*. PhD thesis, The University of Texas at Austin, USA, December 1988.
- [152] PRAHL, S. A. Optical absorption of hemoglobin. Tech. rep., Oregon Medical Laser Center, 1999.
- [153] PRAHL, S. A. PhotochemCAD spectra by category. Tech. rep., Oregon Medical Laser Center, 2001.

- [154] PRAHL, S. A. Optical absorption of fat. Tech. rep., Oregon Medical Laser Center, 2004.
- [155] PRATT, W. *Digital Image Processing*. Wiley & Sons, New York, NY, USA, 1978.
- [156] PRIAMI, C. Algorithmic systems biology. *Communications of the ACM* 52, 5 (May 2009), 80–88.
- [157] RANDEBERG, L., BONESRØNNING, J., DALAKER, M., NELSON, J., AND SVAASAND, L. Methemoglobin formation during laser induced photothermolysis of vascular skin lesions. *Lasers in Surgery and Medicine* 34, 5 (2004), 414–419.
- [158] RAVNBAK, M., PHILIPSEN, P., WIEGELL, S., AND WULF, H. Skin pigmentation kinetics after UVB exposure. *Acta Dermato-Venereologica* 88, 3 (2008), 223–228.
- [159] RAVNBAK, M., PHILIPSEN, P., WIEGELL, S., AND WULF, H. Skin pigmentation kinetics after exposure to ultraviolet A. *Acta Dermato-Venereologica* 89, 4 (2009), 357–363.
- [160] RAVNBAK, M., PHILIPSEN, P., AND WULF, H. The minimal melanogenesis dose/minimal erythema dose ratio declines with increasing skin pigmentation using solar simulator and narrowband ultraviolet B exposure. *Photodermatology, Photoimmunology & Photomedicine* 26, 3 (2010), 133–137.
- [161] RAVNBAK, M. H. *Objective determination of Fitzpatrick skin type*. PhD thesis, University of Copenhagen, 2010.
- [162] ROBERTSON, K., AND REES, J. L. Variation in epidermal morphology in human skin at different body sites as measured by reflectance confocal microscopy. *Acta Dermato-Venereologica* 90, 4 (2010), 368–373.
- [163] ROSEN, C., JACQUES, S., STUART, M., AND GANGE, R. Immediate pigment darkening: visual and reflectance spectrophotometric analysis of action spectrum. *Journal of Photochemistry and Photobiology B: Biology* 51, 5 (1990), 583–588.
- [164] ROSEN, C. F. Topical and systemic photoprotection. *Dermatologic Therapy* 16, 1 (2003), 8–15.
- [165] RUHLE, W., AND WILD, A. The intensification of absorbance changes in leaves by light-dispersion. differences between high-light and low-light leaves. *Planta* 146 (1979), 551–557.
- [166] SAIDI, I. *Transcutaneous optical measurement of hyperbilirubinemia in neonates*. PhD thesis, Rice University, Houston, Texas, USA, 1994.

- [167] SANDIDGE, D. *Digital Infrared Photography Photo Workshop*. Wiley Publishing Inc., Indianapolis, IN, USA, 2009.
- [168] SCHMIDT, T., PELLACINI, F., NOWROUZEZAHRAI, D., JAROSZ, W., AND DACHSBACHER, C. State of the art in artistic editing of appearance, lighting and material. *Computer Graphics Forum* (2015). in press.
- [169] SCHROEDER, P., HAENDELER, J., AND KRUTMANN, J. The role of infrared radiation in photoaging of skin. *Experimental Gerontology* 43 (2008), 629–632.
- [170] SHIMIZU, H. *Shimizu's Textbook of Dermatology*. Hokkaido University Press, 2007.
- [171] SIGGAARD-ANDERSEN, O., NØRGAARD-PEDERSEN, B., AND REM, J. Hemoglobin pigments. spectrophotometric determination of oxy-, carboxy-, met-, and sulfhemoglobin in capillary blood. *Clinica Chimica Acta* 42, 1 (1972), 85 – 100.
- [172] SKLAR, L., ALMUTAWA, F., LIM, H., AND HAMZAVI, I. Effects of ultraviolet radiation, visible light, and infrared radiation on erythema and pigmentation: a review. *Photochemical & Photobiological Sciences* 12 (2013), 54–64.
- [173] SPENCER, M., AND AMONETTE, R. Indoor tanning: Risks, benefits, and future trends. *Journal of the American Academy of Dermatology* 33, 2 (1995), 288–298.
- [174] SQUIER, C. A., COX, P., AND WERTZ, P. W. Lipid content and water permeability of skin and oral mucosa. *Journal of Investigative Dermatology* 96, 1 (1991), 123–126.
- [175] STAM, J. An illumination model for a skin layer bounded by rough surfaces. In *12th Eurographics Workshop on Rendering Techniques* (2001), Springer-Verlag, pp. 39–52.
- [176] STAR, W. M. Light dosimetry *in vivo*. *Physics in Medicine and Biology* 42, 5 (1997), 763.
- [177] STONE, M. *A Field Guide to Digital Color*. AK Peters, Natick, MA, USA, 2003.
- [178] STRICKLAND, E. Blood and money. *IEEE Spectrum* 49, 6 (June 2012), 36–41.
- [179] SUTHERLAND, J. C., AND GRIFFIN, K. P. Absorption spectrum of DNA for wavelengths greater than 300 nm. *Radiation Research* 86, 3 (1981), pp. 399–410.
- [180] SZABO, G., GERALD, A., PATHAK, M., AND FITZPATRICK, T. B. Racial differences in the fate of melanosomes in human epidermis. *Nature* 222, 5198 (06 1969), 1081–1082.

- [181] TADOKORO, T., YAMAGUCHI, Y., BATZER, J., COELHO, S., ZMUDZKA, B., MILLER, S., WOLBER, R., BEER, J., AND HEARING, V. Mechanisms of skin tanning in different racial/ethnic groups in response to ultraviolet radiation. *Journal of Investigative Dermatology* 124, 6 (2005), 1326–1332.
- [182] TALREJA, P. S., KASTING, G. B., KLEENE, N. K., PICKENS, W. L., AND WANG, T. Visualization of the lipid barrier and measurement of lipid pathlength in human stratum corneum. *AAPS PharmSciTech* 3, 2 (2001), 48–56.
- [183] TEARNEY, G. J., BREZINSKI, M. E., SOUTHERN, J. F., BOUMA, B. E., HEE, M. R., AND FUJIMOTO, J. G. Determination of the refractive index of highly scattering human tissue by optical coherence tomography. *Optics Letters* 20, 21 (Nov 1995), 2258–2260.
- [184] THINGNES, J., OYEHAUG, L., AND HOVIG, E. Mathematical and biological processes of skin pigmentation. In *Computational Biosphysics of the Skin*, B. Querleux, Ed. Pan Stanford Publishing, Singapore, 2014, pp. 3–24.
- [185] THINGNES, J., OYEHAUG, L., HOVIG, E., AND OMHOLT, S. The mathematics of tanning. *BMC Systems Biology* 3, 1 (2009), 60.
- [186] THODY, A. J., HIGGINS, E. M., WAKAMATSU, K., ITO, S., BURCHILL, S. A., AND MARKS, J. M. Pheomelanin as well as eumelanin is present in human epidermis. *Journal of Investigative Dermatology* 97, 2 (08 1991), 340–344.
- [187] TRIPP, B. P., AND ORCHARD, J. Population coding in sparsely connected networks of noisy neurons. *Frontiers in Computational Neuroscience* 6, 23 (2012).
- [188] TROWBRIDGE, T. S., AND REITZ, K. P. Average irregularity representation of a rough surface for ray reflection. *Journal of the Optical Society of America* 65, 5 (May 1975), 531–536.
- [189] TSUMURA, N., KAWABUCHI, M., HANEISHI, H., AND MIYABE, Y. Mapping pigmentation in human skin by multi- visible-spectral imaging by inverse optical scattering technique. In *IS&T/SID Eighth Color Imaging Conference* (2000), pp. 81–84.
- [190] TSUMURA, N., OJIMA, N., SATO, K., SHIRAISHI, M., SHIMIZU, H., NABESHIMA, H., AKAZAKI, S., HORI, K., AND MIYAKE, Y. Image-based skin color and texture analysis/synthesis by extracting hemoglobin and melanin information in the skin. In *SIGGRAPH, Annual Conference Series* (New York, NY, USA, 2003), pp. 770–779.

- [191] TUCHIN, V. *Tissue optics: light scattering methods and instruments for medical diagnosis*. SPIE PM. SPIE/International Society for Optical Engineering, Bellingham, WA, USA, 2007.
- [192] TYO, J., KONSOLAKIS, A., DIERSEN, D., AND OLSEN, R. Principal-components-based display strategy for spectral imagery. *IEEE Transactions on Geoscience and Remote Sensing* 41, 3 (March 2003), 708–718.
- [193] VAGNI, F. Survey of hyperspectral and multispectral imaging technologies. Tech. Rep. RTO-TR-SET-065-P3, NATO Research and Technology Organisation, May 2007.
- [194] VAN NOORDEN, R. Interdisciplinary research by the numbers. *Nature* 525, 7569 (September 2015), 306–307.
- [195] VAN VEEN, R. L., STERENBORG, H., PIFFERI, A., TORRICELLI, A., AND CUBEDDU, R. Determination of VIS-NIR absorption coefficients of mammalian fat, with time- and spatially resolved diffuse reflectance and transmission spectroscopy. In *Biomedical Topical Meeting* (2004), Optical Society of America, p. SF4.
- [196] VARCOE, J. S. *Clinical Biochemistry: Techniques and Instrumentation : A Practical Course*. World Scientific, 2001.
- [197] VIATOR, J. A., KOMADINA, J., SVAASAND, L. O., AGUILAR, G., CHOI, B., AND STUART, N. A comparative study of photoacoustic and reflectance methods for determination of epidermal melanin content. *Journal of Investigative Dermatology* 122, 6 (06 2004), 1432–1439.
- [198] VRHEL, M., GERSHON, R., AND IWAN, L. Measurement and analysis of object reflectance spectra. *Color Research and Application* 19, 1 (1994), 4–9.
- [199] WANG, J., TONG, X., LIN, S., PAN, M., WANG, C., BAO, H., GUO, B., AND SHUM, H. Appearance manifolds for modeling time-variant appearance of materials. In *ACM SIGGRAPH 2006* (2006), ACM, pp. 754–761.
- [200] WANG, L., JACQUES, S., AND ZHENG, L. MCML – Monte Carlo modelling of light transport in multi-layered tissues. *Computer Methods and Programs in Biomedicine* 47 (1995), 131–146.
- [201] WANG, L., LEEDHAM, G., AND CHO, S.-Y. Infrared imaging of hand vein patterns for biometric purposes. *IET Computer Vision* 1, 3-4 (December 2007), 113–122.

- [202] WEYRICH, T., MATUSIK, W., PFISTER, H., BICKEL, B., DONNER, C., TU, C., MCANDLESS, J., LEE, J., NGAN, A., JENSEN, H. W., AND GROSS, M. Analysis of human faces using a measurement-based skin reflectance model. In *SIGGRAPH, Annual Conference Series* (New York, USA, 2006), pp. 1013–1024.
- [203] WILLIAMS, M. L., HINCENBERGS, M., AND HOLBROOK, K. A. Skin lipid content during early fetal development. *Journal of Investigative Dermatology* 91, 3 (09 1988), 263–268.
- [204] WOLBER, R., SCHLENZ, K., WAKAMATSU, K., SMUDA, C., NAKANISHI, Y., HEARING, V., AND ITO, S. Pigmentation effects of solar simulated radiation as compared with uva and uvb radiation. *Pigment Cell & Melanoma Research* 21, 4 (08 2008), 487–491.
- [205] WULF, H., PHILIPSEN, P., AND RAVNBAK, M. Minimal erythema dose and minimal melanogenesis dose relate better to objectively measured skin type than to Fitzpatrick's skin type. *Photodermatology, Photoimmunology & Photomedicine* 26, 6 (2010), 280–284.
- [206] YABE, K., ANDO, Y., ITO, M., AND TERAOKA, N. Simple method for screening aflatoxin-producing molds by UV photography. *Applied and Environmental Microbiology* 53, 2 (February 1987), 230–234.
- [207] YAMAGUCHI, Y., BRENNER, M., AND HEARING, V. J. The regulation of skin pigmentation. *Journal of Biological Chemistry* 282, 38 (2007), 27557–27561.
- [208] YANG, M., TUCHIN, V., AND YAROSLAVSKY, A. Principles of light-skin interactions. In *Light-Based Therapies for Skin of Color* (London, 2009), E. Baron, Ed., Springer-Verlag, pp. 1–44.
- [209] YARYNOVSKA, I. H., AND BILYI, A. Absorption spectra of sulfhemoglobin derivatives of human blood. In *Optical Diagnostics and Sensing VI* (2006), G. Cote and A. Priezzhev, Eds., vol. 6094, SPIE, pp. 1–6.
- [210] YIM, D., BARANOSKI, G. V. G., KIMMEL, B. W., CHEN, T. F., AND MIRANDA, E. A cell-based light interaction model for human blood. *Computer Graphics Forum* 31, 2 (2012), 845–854.
- [211] YOUNG, A. R. Chromophores in human skin. *Physics in Medicine and Biology* 42, 5 (1997), 789.
- [212] ZONIOS, G., DIMOU, A., BASSUKAS, I., GALARIS, D., TSOLAKIDIS, A., AND KAXIRAS, E. Melanin absorption spectroscopy: new method for noninvasive skin investigation and melanoma detection. *Journal of Biomedical Optics* 13, 1 (2008), 014017.

- [213] ZUCKER, S. D., HORN, P. S., AND SHERMAN, K. E. Serum bilirubin levels in the u.s. population: gender effect and inverse correlation with colorectal cancer. *Hepatology* 40, 4 (Oct 2004), 827–835.

APPENDICES

A Supplementary Biophysical Data

As stated in this thesis, in order to evaluate the predictive capabilities of the HyLloS model (Chapter 4), we have compared its results, recommended as being provided as an independent unit of the rendering pipeline [70], with measured data and experimental observations reported in the literature. The measured skin characterization data for the specimens used in the actual experiments were not provided. As such, the values assigned to the parameters employed in the computation of the HyLloS modelled curves (Tables 6.1 and 6.2) were selected based on the specimens' qualitative descriptions. These values were selected to be within biophysically valid ranges provided in the scientific literature. We remark that the values assigned for most of the biophysical quantities (Table 6.2) employed in the formulation of the model correspond to average values available in the literature that are not normally subject to change, and, therefore, can be kept fixed for the simulations. The absorption spectra of the light-absorbing materials employed in the simulations performed by the HyLloS model are plotted in Figure A.1.

In the remainder of this appendix, we list specific details needed to derive the biophysical parameters used to produce the HyLloS modelled results.

- The stratum corneum is composed of 10 to 30 layers of flattened corneocyte cells (whose thickness varies from $0.2 \mu m$ to $0.7 \mu m$) separated by intercellular spaces on the order of $0.1 \mu m$, leading to a total thickness varying from $3 \mu m$ to $36 \mu m$ [2, 148].
- The spectral refractive indices of the layers are computed using the Gladstone and Dale law [191] considering their refractive indices (measured at $1300 nm$) specified in Table 6.2 along with the water content of each layer and the spectral refractive index of water provided by Palmer and Williams [139].
- The spectral absorption coefficients for the melanins are derived from their spectral extinction coefficient ($\varepsilon(\lambda)$) curves (Figure A.1) employing the following expression:

$$\zeta(\lambda) = \varepsilon(\lambda) \ln(10) c_c, \tag{A.1}$$

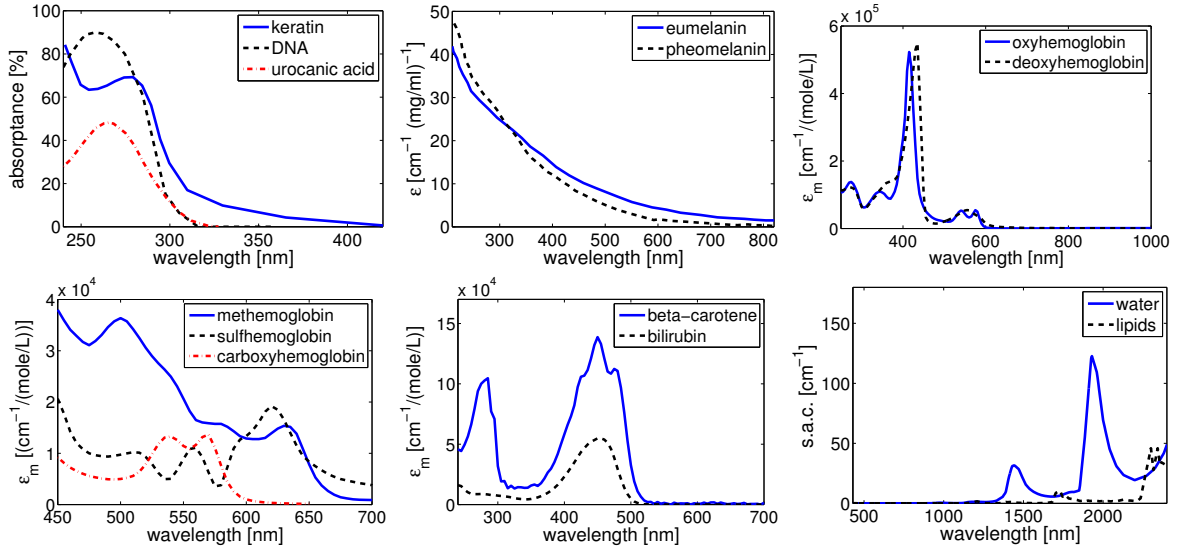


Figure A.1: Absorption spectra of the main absorbers acting within the skin tissues. Top left: absorbance curves for solid keratin over a distance of $4 \mu\text{m}$ [22], $50 \mu\text{g/mL}$ of DNA, and $15 \mu\text{mole/L}$ of urocanic acid over a distance of 1cm [38, 137, 179, 211]. Top centre: extinction coefficient (ε) curves for melanin [91]. Top right: molar extinction coefficient (ε_m) curves for functional hemoglobins [152]. Bottom left: molar extinction coefficient (ε_m) curves for dysfunctional hemoglobins [157, 171, 209]. Bottom centre: molar extinction coefficient (ε_m) curves for beta-carotene and bilirubin [153]. Bottom right: specific absorption coefficient (s.a.c.) curves for water [139, 150] and lipids [4, 154, 195].

where c_c corresponds to their concentration.

- The spectral absorption coefficients for the hemoglobins, beta-carotene and bilirubin are derived from their spectral molar extinction coefficient ($\varepsilon(\lambda)$) curves (Figure A.1) employing the following expression:

$$\zeta(\lambda) = \frac{\varepsilon_m(\lambda) \ln(10) c_c}{M_w}, \quad (\text{A.2})$$

where M_w corresponds to their respective molar weights. The molar weights employed for the hemoglobins, beta-carotene and bilirubin are 66500 g/mole , 537 g/mole and 585 g/mole , respectively [18].

- The spectral absorption coefficients of keratin, DNA and urocanic acid are derived from their spectral absorbance ($A(\lambda)$) curves (Figure A.1). We note that $-\log(1 - A(\lambda))$ is equal to the spectral absorbance denoted by $A_b(\lambda)$ [22]. Moreover, in order to obtain

the spectral absorption coefficients*, one needs to multiply the corresponding $A_b(\lambda)$ by $\ln(10)$ and make appropriate adjustments with respect to the concentration and thickness (depth) of the sample used in its measurement [120]. The specific formula for each relevant material are provided below:

- In the case of keratin, its spectral absorption coefficient can then be computed as:

$$\zeta(\lambda) = -\ln(1 - A(\lambda)). \quad (\text{A.3})$$

However, since the absorbance data is measured over $4 \mu\text{m}$, we need to scale $\zeta(\lambda)$ by 4×10^4 to have it in $1/\text{cm}$ units.

- In the case of DNA, its spectral absorption coefficient can be computed as:

$$\zeta(\lambda) = -\ln(1 - A(\lambda)) \delta, \quad (\text{A.4})$$

where δ corresponds to the density of DNA in human skin. The DNA mass per cell is $\approx 6.4 \times 10^{-12} \text{ g}$ [196], and there are $\approx 1.1 \times 10^{11}$ cells [57] in skin. Hence, since the average volume occupied by human skin in fully developed specimens is $\approx 3.8 \text{ L}$ [2], the density of DNA in skin can be estimated as $\approx 0.185 \text{ g/L}$.

- In the case of urocanic acid, its spectral absorption coefficient can be computed as:

$$\zeta(\lambda) = -\ln(1 - A(\lambda)) M_w. \quad (\text{A.5})$$

From the literature, the molar weight of urocanic acid in stratum corneum ranges from 0.0029 mole/L to 0.0287 mole/L [135], and we use an intermediate value of 0.01 mole/L in our simulations.

*The absorption coefficient of a given material can be expressed in terms of its absorptivity which is given by the product of the absorbance and $\ln(10)$ divided by the concentration and thickness (depth) of the sample used in its measurement [120].

B Deriving Tanning Specification Data

The tanning simulation framework (Chapter 5) describes the physiological changes of skin using a first principles approach based on the current understanding of this biophysical phenomenon [26, 160, 181, 184]. However, the empirical investigations related to tanning that we have examined are focused on the aggregate large scale biophysical changes rather than the small scale physiological phenomena. In the absence of such detailed information, we used physical measurements regarding overall changes in skin pigmentation (provided by Tadokoro et al. [181]) and thickness (provided by Lopez et al. [112]) to guide the selection of the parameter values in relation to the melanin dynamics (Section 5.1) and thickness dynamics components (Section 5.2) respectively. Exposure doses that are consistent with the experimental conditions were used as input for the tanning simulation framework*. The values assigned to its parameters were then adjusted to fit the measured data. The resulting figures are presented in Tables 6.4 to 6.6.

Using the values in Tables 6.4 and 6.5, the melanin dynamics component replicates the temporal epidermal melanin distribution data reported by Tadokoro et al. [181] as seen in Figure B.1 (top row). The same simulated dataset also provides good agreement with reported values regarding overall melanin content change ($\sim 10\%$ increase on day 7), as seen in Figure B.1 (bottom row). In Figure B.2, the thickness dynamics component of the framework uses the values in Table 6.6 to replicate the temporal trends reported by Lopez et al. [112] regarding thickness changes in the skin epidermis. As stated in this thesis, these parameter values may be adjusted to describe specimens with lower or higher tanning ability.

We remark that there is only one other algorithmic formulation available in the scientific literature that addresses the simulation of the tanning phenomenon [184, 185]. This formulation is also constrained by similar data scarcity issues and relies on similar data fitting approaches to obtain their parameter values.

*Tadokoro et al. [181] employed an initial exposure dose of 1 MED to acquire their data. However, we assume this dose is at least 1 MMD to elicit a melanogenesis response.

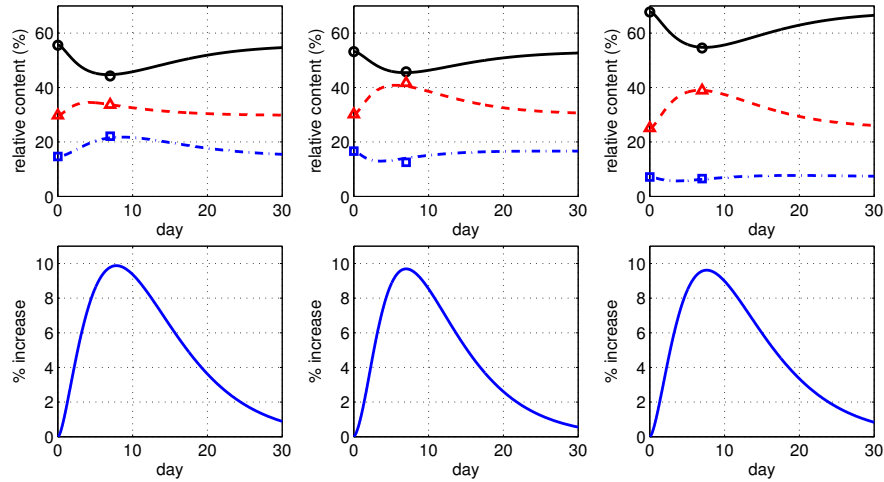


Figure B.1: Data used to guide the selection of parameter values for the melanin dynamics component of the tanning simulation framework. From left to right: data for lightly, moderately and darkly pigmented specimens. Top row: comparisons of measured pigmentation distribution changes with the simulated pigmentation distribution changes. The measured values provided by Tadokoro et al. [181] for the stratum basale, stratum spinosum and stratum granulosum are represented by circles, triangles and squares, respectively. The simulated values for the stratum basale stratum, spinosum and stratum granulosum are represented by the solid, dashed and dash-dotted lines, respectively. Bottom row: corresponding simulated overall pigmentation change. The simulated data was generated using the melanin dynamics component of the framework described in Section 5.1 along with the parameter values presented in Tables 6.4 and 6.5 considering one initial exposure dose of 1 MMD.

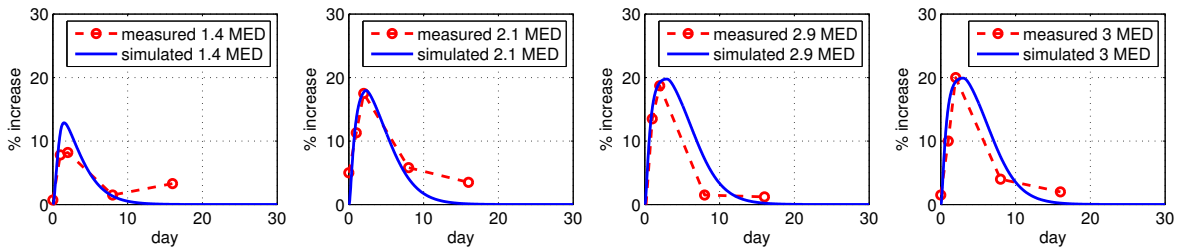


Figure B.2: Data used to guide the selection of parameter values for the thickness dynamics component of the tanning simulation framework. The measured data was provided by Lopez et al. [112]. The simulated data was generated using the thickness dynamics component of the framework described in Section 5.2 along with the parameter values presented in Table 6.6.

C Melanosome Distribution Patterns Affecting Skin Reflectance

During the development of the HyLloS model (Chapter 4), one of our goals was to incorporate the distribution patterns of melanin and particle nature of melanosomes situated within the skin tissues. This was motivated by observations [7, 131, 143] that the effects of melanin on skin appearance attributes (*e.g.*, colour) and UV light attenuation must be related not only to its skin content, but also to where it is found and how it is dispersed within the cutaneous tissues.

Although these effects may be perceptually negligible to the naked eye (Figures 6.3 and 6.4), they may be significant for technical applications in fields like biomedicine that require the correct interpretation of skin spectral responses. Such applications range from noninvasive health-monitoring programs (*e.g.*, [56, 191]) to the screening (*e.g.*, [13, 166]) and treatment of medical conditions (*e.g.*, [208]).

Moreover, its use in inversion procedures aimed at the estimation of skin biophysical parameters, such as the content and distribution patterns of its main light attenuation agents, has a pivotal relevance for medical and cosmetics research. For example, UV and visible skin responses can be used in the assessment of the intrinsic photoprotective properties of a skin specimen [130], while IR responses can be used in the assessment of skin hydration [9], a key factor contributing to the protective properties of this complex organ. These research efforts, in turn, contribute to the scientific foundation required to increase the efficacy of products (*e.g.*, sunscreens) designed to mitigate the harmful effects of light overexposure such as photoaging [169] and skin cancer [143].

Several techniques employed in *in vivo* estimation of melanin content do not explicitly account for the particle nature and dispersion patterns of the melanosomes. For example, Kollias and Baqer [102] presented a technique for the estimation of melanin content based on the measurement of skin reflectance values in the 600 *nm* to 720 *nm* range. It was later modified [89] to account for reflectance values in the 600 *nm* to 850 *nm* range. This technique, which is often employed in skin pigmentation research (*e.g.*, [41, 163]), explicitly assumes melanin occurring

only in colloidal form [102].

There are also inversion procedures [18] in which the interpretation of measured skin reflectance values is based on the analysis of results derived from models of light interactions with cutaneous tissues (*e.g.*, [134, 189]). Although, the models employed in these procedures account for the epidermal melanin content in terms of average epidermal volume occupied by melanosomes, they do not explicitly account for the particle nature and dispersion patterns of the melanosomes either.

In this appendix, we investigate the impact of the different forms of melanin and their distribution patterns on human skin reflectance using HyLloS. In the following section, we concisely review the *in silico* framework used in our investigation, and in Section C.2 we present our findings and discuss their practical implications. Finally, in Section C.3, we outline perspectives for further investigation on this topic.

C.1 Methods and Data

We remark that HyLloS employs a first principles modelling approach that explicitly accounts for the particle nature and the different dispersion patterns of the melanosomes within the epidermal layers (stratum granulosum, spinosum and basale). Hence, it enables the computation of skin reflectance considering melanin occurring in colloidal form (colloidal case) as well as clustered within melanosomes, which may be located in the stratum basale (baseline case) or dispersed throughout the epidermal layers (dispersion case).

Using HyLloS, we generated directional-hemispherical reflectance curves for skin specimens with different levels of pigmentation (light and dark) considering an angle of incidence of 10° and using the model parameters corresponding to specimens S3 (lightly pigmented) and S4 (darkly pigmented) provided in Tables 6.1 and 6.2. The default values for specimen S3 correspond to its baseline case. To obtain the baseline case for specimen S4, the default values need to be modified to set the melanosome content for the stratum granulosum, spinosum and basale to 0.0%, 0.0% and 30.0%, respectively.

Regarding the dispersion case, the melanosomes were considered dispersed in equal percentages in the stratum spinosum, granulosum and basale. For specimen S3, this involves setting the melanosome content for all three epidermal layers to 1.0% while the default values for S4 already corresponds to the dispersion case.

We then compared the baseline and dispersion cases' reflectance curves with curves obtained considering the occurrence of melanin only in colloidal form (colloidal case). These were

computed with melanosome percentages set to zero and their corresponding melanin content values transferred to the colloidal melanin percentages in the respective epidermal layers.

For completeness, we also provide root mean square error (RMSE) values computed for the reflectance curves associated with the baseline and dispersion (test) cases with respect to reflectance curves associated with the colloidal (reference) case considering the 250 *nm* to 1400 *nm* region notably affected by melanin [7]. These values were computed using the following expression:

$$RMSE = \sqrt{\frac{1}{N} \sum_{i=1}^N (\rho_{\alpha}(\lambda_i) - \rho_{\beta}(\lambda_i))^2}, \quad (C.1)$$

where ρ_{α} and ρ_{β} correspond to the reference and test reflectance datasets respectively, and N represents the total number of wavelengths sampled with a 5 *nm* resolution within a selected spectral region.

C.2 Findings and Discussion

As it can be observed in the comparisons between the baseline and colloidal cases depicted in Figure C.1, reflectance values may be underestimated when one considers the occurrence of melanin only in the colloidal form, particularly in the 600 *nm* to 900 *nm* region. Although the same trend applies to both specimens, the RMSE values presented in Figure C.2 indicate a larger impact for the lightly pigmented specimen in the visible region, and a larger impact for the darkly pigmented specimen in the near-infrared (NIR*) region.

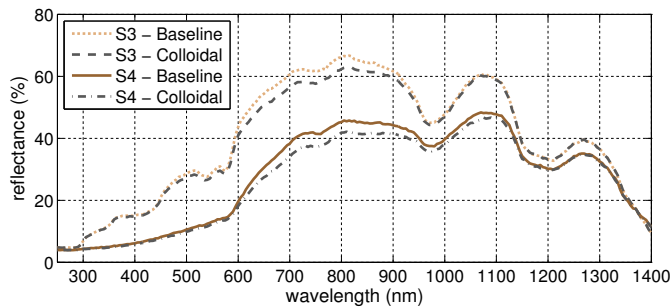


Figure C.1: Reflectance curves for a lightly (S3) and a darkly (S4) pigmented specimen considering the baseline and colloidal cases.

*According to the CIE, the NIR spectral domain, often referred to as IR-A [40], goes from 700 *nm* to 1400 *nm*.

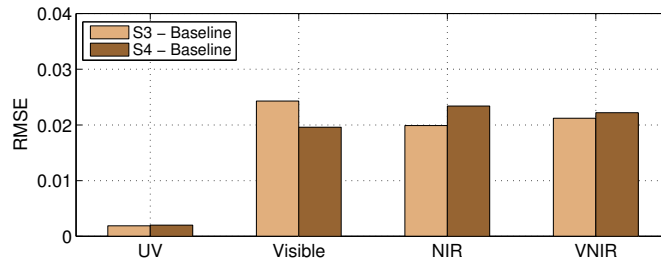


Figure C.2: RMSE values for the baseline (case) reflectance curves of a lightly (S3) and a darkly (S4) pigmented specimen with respect to their corresponding colloidal (case) reflectance curves. The spectral regions denoted by UV, Visible, NIR and VNIR (Visible–NIR) go from 250 *nm* to 400 *nm*, 400 *nm* to 700 *nm*, 700 *nm* to 1400 *nm* and 400 *nm* to 1400 *nm*, respectively.

The comparisons between the dispersion and colloidal cases depicted in Figure C.3 show a similar trend for the lightly pigmented specimen. For the darkly pigmented specimen, however, the reflectance values are slightly overestimated in the 600 *nm* to 900 *nm* region when one considers the occurrence of melanin only in colloidal form. Accordingly, the RMSE values presented in Figure C.4 indicate a larger impact for the lightly pigmented specimen across the entire UV–NIR region of interest.

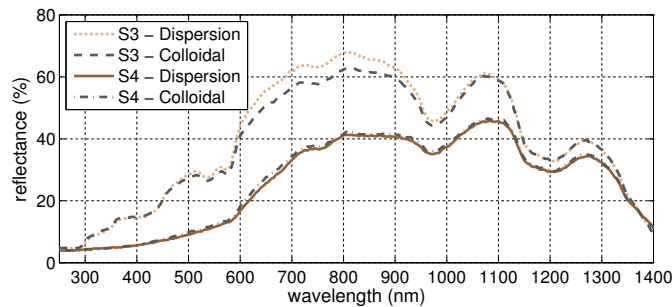


Figure C.3: Reflectance curves for a lightly (S3) and a darkly (S4) pigmented specimen considering the dispersion and colloidal cases.

The reflectance curves for the darkly pigmented specimen presented in Figures C.1 and C.3 also show lower reflectance values for the dispersion case in comparison with the baseline case. Such reflectance decrease is observed when an individual’s facultative pigmentation (determined by environmental stimuli [7]) is enhanced by UV light exposure. It has been stated that this reflectance decrease (resulting in an increasingly darker skin tone in the visible domain) is primarily caused by an increase in melanosome dispersion (accompanied by a degradation into smaller particles) toward the surface of the skin [204]. Moreover, such reflectance variations

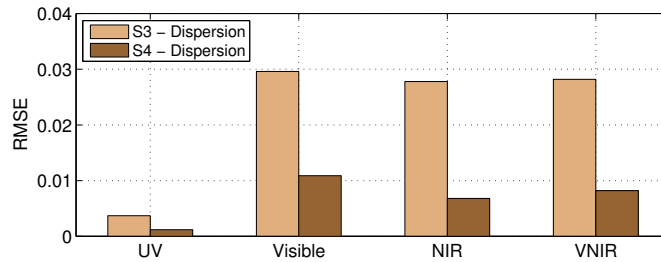


Figure C.4: RMSE values for the dispersion (case) reflectance curves of a lightly (S3) and a darkly (S4) pigmented specimen with respect to their corresponding colloidal (case) reflectance curves. The spectral regions denoted by UV, Visible, NIR and VNIR go from 250 nm to 400 nm, 400 nm to 700 nm, 700 nm to 1400 nm and 400 nm to 1400 nm, respectively.

are more noticeable in individuals characterized by a higher level of constitutive pigmentation (genetically determined, uninfluenced by UV light exposure [7]). As further illustrated by the plot presented in Figure C.5, this reflectance decrease cannot be predictively reproduced when one considers the occurrence of melanin only in colloidal form.

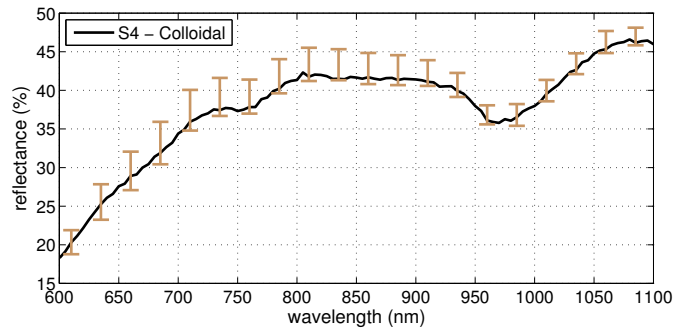


Figure C.5: Variations (bars) in the reflectance values of a darkly pigmented specimen considering melanosomes located in the stratum basale and dispersed throughout the epidermis. The corresponding colloidal (case) reflectance curve is included for comparison.

The shortcomings of overlooking the particle nature and distribution patterns of the melanosomes can be associated with changes in cutaneous light absorption profiles elicited by detour and sieve effects (Section 3.3). Recall that the net result of these effects depends on the absorption spectra of the relevant pigments as well as on the distribution and volume fraction of related structures [29,62]. In the case of human skin, these structures are represented by melanosomes and melanosome complexes [136], and the pigment of interest, melanin, may also be present in the surrounding medium in colloidal form [143], further influencing the net result of detour and sieve effects. Hence, by considering the occurrence of melanin only in colloidal

form and ignoring detour and sieve effects associated with the particle nature and distribution patterns of these melanin-containing organelles, one cannot establish a correct correlation between reflectance values and epidermal melanin content.

In order to take detour and sieve effects into account, one may consider adjusting the *in vitro* absorption spectra of the pigments of interest (eumelanin and pheomelanin) according to the lengthening of the optical path verified in the skin tissues [18], referred as differential path-length in biomedical investigations [45]. In plant sciences, a similar adjustment is performed using a quantity called ratio of intensification [29] or factor of intensification [165]. The main difficulty in employing this correction factor is the scarcity of available measured data to allow its accurate quantification for different *in vivo* conditions.

Although light transport algorithms based on first principles approaches also depend on data availability, notably with respect to specimen characterization data, such a dependence is less restrictive than the dependence associated with the measurement of differential path-length. We remark that the latter involves a larger number of unknowns, including not only specimen characterization data, but also different illumination geometries as well as spectral and temporal dimensions associated with the actual measurement conditions. Such conditions, on the other hand, can be reproduced through computational experiments in a straightforward manner. Hence, we believe that by explicitly accounting for the particle nature and distribution patterns of the melanosomes, predictive simulation frameworks supported by first principles light interaction models, such as HyLloS (Chapter 4), can provide effective contributions for the enhancement of melanin content estimations based on reflectance inversion procedures.

C.3 Concluding Remarks

Melanin has been the object of extensive studies across different disciplines not only due its impact on skin appearance, but more importantly its central role on the photoprotection of this complex organ. Its *in vivo* identification (different forms and types) and quantification remain elusive tasks, however. Although recent advances offer a myriad of opportunities for improving the accuracy of these procedures, we believe that the scientific community has to take a synergistic and comprehensive view of the biological and optical processes taking place within the cutaneous tissues, without overlooking important phenomena affecting their interactions with light, in order to achieve tangible progress in this area. Such an approach will be essential for enhancing the qualitative and quantitative predictions regarding the occurrence and photobiological functions performed by this fundamental material.

D Effective Compression and Reconstruction of Human Skin Hyperspectral Reflectance Databases

The access to robust skin hyperspectral reflectance databases is essential for the enhancement of a wide range of biomedical applications, from the assessment of biophysical properties of cutaneous tissues (*e.g.*, [55, 102, 197]) and the investigation of photobiological processes affecting skin health and appearance (*e.g.*, [131, 163, 208]), to the prevention and screening of diseases (*e.g.*, [13, 30, 191, 212]). Although such databases are still not readily available, this situation is likely to change rapidly with the development of new technologies for the accurate measurement [42] and predictive modelling of skin responses within and outside the visible domain as demonstrated by HyLloS (Chapter 4). It is worth noting that in the case of computer models, reliable spectral reflectance data is required to evaluate their predictions results in the first place.

When assembling databases composed of measured reflectance data, one needs to consider several dimensions associated with data capture procedures such as spectral resolution, illumination and viewing geometry. Furthermore, in the case of databases composed of modelled reflectances, one may need to account for additional dimensions associated with the combination of distinct specimen characterization parameters. Although, in theory, space could be saved by storing these parameters instead of the modelled reflectance data, the accurate computation of this data is often highly time consuming. Hence, for applications that demand high interactivity rates, it usually needs to be precomputed, stored offline and quickly accessed on the fly.

Regardless of the nature of the stored data, measured or modelled, the main guidelines in the design of hyperspectral reflectance databases are compactness and low reconstruction error [21]. In this appendix, we investigate how PCA [68, 97], which is widely employed in many areas (*e.g.*, signal processing [155], pattern recognition [142], colorimetry [79], applied meteorology [84] and remote sensing [192]), can be used to achieve these goals with respect to

hyperspectral skin responses. In order to achieve higher accuracy to computational cost (memory space) ratios for human skin hyperspectral databases, we also propose the application of a piecewise PCA approach (PPCA) based on characteristic cutaneous light attenuation profiles.

D.1 Methods and Data

Consider a skin hyperspectral reflectance database represented by a $s_x \times w_x$ matrix M_x , where each row contains the reflectance spectrum of a given specimen, and each column stores the reflectance values with respect to the sample wavelengths. The goal is to reduce the dimensionality of M_x , *i.e.*, the PCA approach is applied to the entire dataset, rather than to each specimen’s reflectance spectrum.

In order to implement PCA, we choose to use the singular value decomposition (SVD) technique [155] due to its numerical stability. Using this technique, one can obtain the $w_x \times w_x$ matrix V_x and the matrix $C_x = M_x * V_x$. While V_x stores the basis of principal components (as column vectors), C_x stores the coordinates (coefficients) relative to the basis (as row vectors).

Since the goal is to reduce the dimension of the data, one usually chooses a reduced number of components, $s'_x \ll s_x$, and stores smaller versions (the first s'_x columns) of C_x and V_x , more specifically the $s_x \times s'_x$ matrix C'_x and the $w_x \times s'_x$ matrix V'_x respectively. Accordingly, the reconstructed reflectance spectrum of a selected specimen i , where $1 \leq i \leq s$, is given by:

$$\rho_r = C'_{x,i} * (V'_x)^T, \quad (\text{D.1})$$

where $C'_{x,i}$ corresponds to the i^{th} row of matrix C'_x .

It has been observed that while the melanins (eumelanin and pheomelanin) and hemoglobins (oxy- and deoxygenated) dominate light attenuation within human skin in the UV–Visible (250 *nm* to 700 *nm*) range and their influence is increasingly diminished in the IR-A (700 *nm* to 1400 *nm*) region, lipids and water start to contribute to light attenuation in this region and have a dominant role in the IR-B (1400 *nm* to 2500 *nm*) range [7]. These well defined regions suggest that the use of an adaptive PCA approach may result in lower reconstruction errors and more compactness.

In other words, instead of an integral application of PCA over the entire hyperspectral domain of interest (250 *nm* to 2500 *nm*), we can perform a piecewise application of PCA, in which each piece corresponds to one of the three regions (UV–Visible, IR-A and IR-B). Since the effectiveness of the PCA approach depends on the representativeness of the reflectance data used in the singular value decomposition, applying PPCA to matrices for each of the three regions

yields different components than applying PCA to a matrix for the entire domain of interest. After eliminating components that have a small impact on the overall reflectance curves, reconstructing a particular curve with PPCA gives pieces for each region, which might not join smoothly at region boundaries. Although it would be possible to use a constrained PPCA algorithm to ensure smooth joins, we found such discontinuities to be negligible with respect to skin reflectance data.

In our experiments, we considered a skin reflectance hyperspectral database (SHRD) composed of 144 distinct skin directional-hemispherical curves (Figure D.1) with a spectral resolution of 5 nm. These curves correspond to 144 distinct skin specimens (denoted from N1 to N144) and were obtained using the HyLloS model (Chapter 4). In their computation, we considered dataset S3 (Tables 6.1 and 6.2) as the baseline specimen, an angle of incidence of 10° and variations in the parameters associated with the main light attenuation agents: eumelanin (from 24 to 62.5 g/L), pheomelanin (from 1.5 to 5 g/L), dermal blood content (from 0.225 to 3.12 %), water content (from 26.25 to 93.75 %), and lipids content (from 11.32 to 0.25 %). Note that these parameter ranges are within physiologically valid limits indicated in the scientific literature.

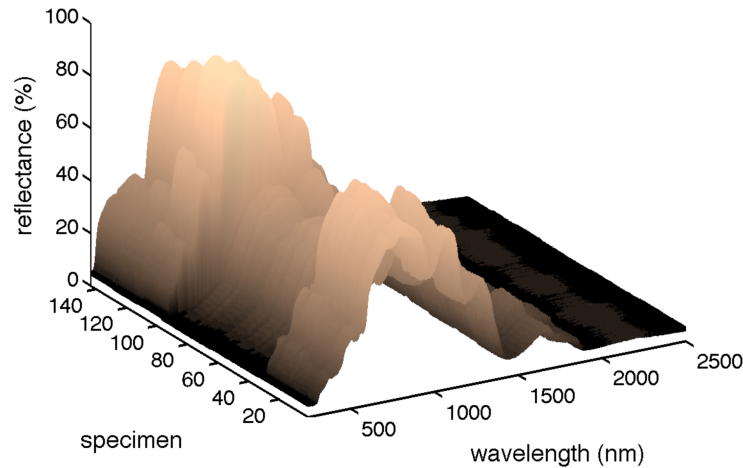


Figure D.1: Plot depicting the skin hyperspectral reflectance database (SHRD) employed in this investigation.

Since relevant biomedical applications (e.g., [102, 197]) require the use of reference reflectance curves obtained at amelanotic skin sites such as those found in vitiligo subjects, we have also included in the database amelanotic curves obtained by removing the melanin pigmentation. Considering that such curves markedly depart from typical skin reflectance curves, they also allowed us to expand our scope of *in silico* experimental observations.

For consistency with related works (*e.g.*, [21, 79]), we use the RMSE measure (Equation C.1) in our experiments. As one increases the number of components (and coefficients) used in the reconstruction of spectral curves, their RMSE values with respect to the original modelled curves decrease. The goal is to obtain the best compromise between the number of components and the RMSE. We selected as reference for low-reconstruction error a RMSE value equal to 0.01, which has also been employed for this purpose in works involving other optically-complex natural materials such as plant leaves [21].

In order to further illustrate different levels of reconstruction fidelity, we have also generated skin swatches. These swatches were generated using the same procedure employed in Sections 6.1.2 and 6.1.3. More specifically, in the case of visible reflectance data, we employed a standard XYZ to sRGB conversion procedure [18] considering a light source that approximates a standard D65 illuminant [177]. In the case of UV and IR (*i.e.*, encapsulating IR-A and IR-B) reflectance data, we integrated the reflectance values over their respective spectral region and applied a tinted greyscale filter to the resulting values, which are depicted in pseudo colours.

D.2 Findings and Discussion

Initially, we applied PCA to the SHRD melanotic subset, and computed the RMSE values associated with all reconstructed melanotic curves obtained using different numbers of components. The summary of the resulting maximum RMSE values provided in Table D.1 indicates that only two components were required to reconstruct the melanotic curves with a RMSE below 0.01. This level of compression is significant, especially if compared to similar results obtained for plant leaves, which required at least five components [21]. A comparison between the original and reconstructed curve for specimen N32 (with the maximum RMSE value) is presented in Figure D.2, and their close agreement is further illustrated by the skin swatches depicted in Figure D.3.

We then applied PCA to the SHRD amelanotic subset, and computed the RMSE values associated with all reconstructed amelanotic curves obtained using different numbers of components. The summary of the resulting maximum RMSE values provided in Table D.1 indicates that three components were required to reconstruct the amelanotic curves with a RMSE below 0.01. A comparison between the original and reconstructed curve for specimen N135 (with the maximum RMSE) is presented in Figure D.4.

Finally, we applied the PCA approach to the entire SHRD, and computed the RMSE values associated with all reconstructed melanotic and amelanotic curves obtained using different numbers of PCA components. Due to the noticeable deviation of the amelanotic curves from

PCA Components	Specimens		
	Melanotic	Amelanotic	All
1	0.0504	0.0337	0.0738
2	0.0099	0.0172	0.0245
3	0.0058	0.0099	0.0171
4	0.0037	0.0030	0.0069
8	0.0014	0.0012	0.0023

Table D.1: Maximum RMSE values computed for the PCA reconstructed curves (250 nm to 2500 nm) with respect to the curves for the 96 melanotic, 48 amelanotic and all 144 specimens depicted in the SHRD obtained using the HyLloS model. The values in boldface for the melanotic and amelanotic subsets as well as the entire database correspond to specimens N32, N135 and N127, respectively.

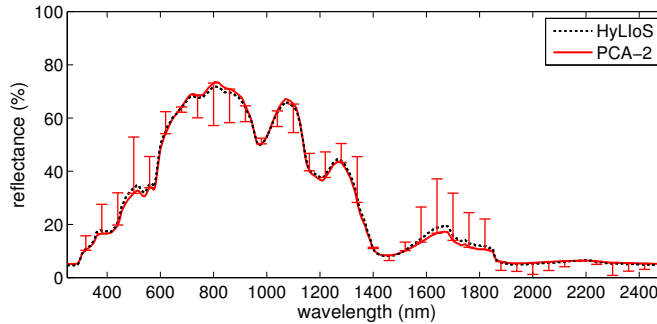


Figure D.2: Modelled (HyLloS) and reconstructed (PCA using two components) curves for specimen N32. Error bars represent differences between the curves, magnified by a factor of 10. Resulting RMSE values for the UV-Visible, IR-A and IR-B regions were 0.0117, 0.0118 and 0.0109, respectively.

typical skin reflectance curves, it was expected that a larger number of components would be required to keep the reconstruction error low. Although we needed to use more components (in comparison with the reconstruction of the curves in the melanotic subset), the summary of the resulting maximum RMSE values provided in Table D.1 indicates that only four components were required to reconstruct all curves with a RMSE below 0.01. Hence, even considering extreme responses associated with amelanotic specimens, one can obtain a high compression accompanied by a relatively low-reconstruction error as illustrated by the comparison between the original and reconstructed curve for specimen N127 (with the maximum RMSE value) presented in Figure D.5.

When we repeated the experiments employing the PPCA approach (Figures D.6 to D.8), we were able to obtain even more accurate reconstructed curves using the same number of



Figure D.3: Skin swatches in the UV (left), visible (centre) and IR (right) ranges obtained for specimen N32 using PCA with one component (top), two components (middle) and the original modelled curve (bottom) provided by HyLloS.

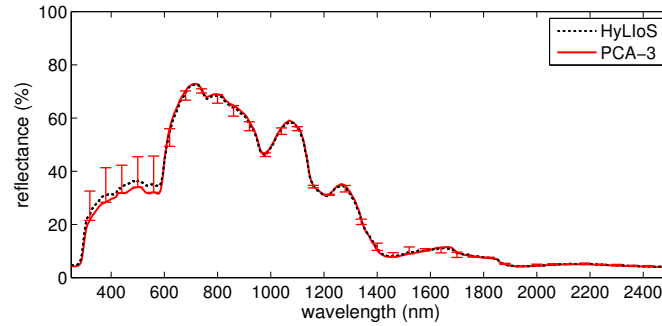


Figure D.4: Modelled (HyLloS) and reconstructed (PCA using three components) curves for specimen N135. Error bars represent differences between the curves, magnified by a factor of 10. Resulting RMSE values for the UV-Visible, IR-A and IR-B regions were 0.0209, 0.0172 and 0.0140, respectively.

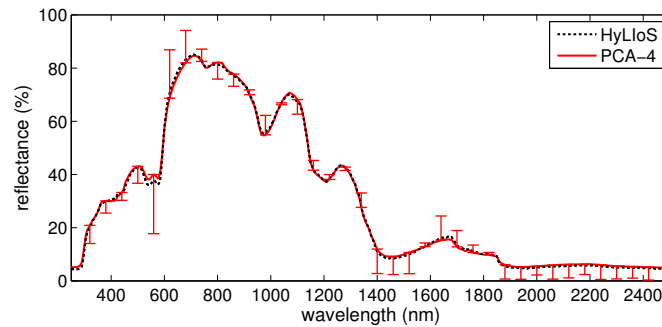


Figure D.5: Modelled (HyLloS) and reconstructed (PCA using four components) curves for specimen N127. Error bars represent differences between the curves, magnified by a factor of 10. Resulting RMSE values for the UV-Visible, IR-A and IR-B regions were 0.0127, 0.0105 and 0.0087, respectively.

components. Besides the overall reduction of reconstruction errors, indicated by the lower RMSE values computed for the PPCA reconstructed curves, a more detailed inspection of the results provided by PCA (Figures D.2, D.4 and D.5) and PPCA (Figures D.6, D.7 and D.8) revealed a closer qualitative agreement provided by the latter approach, notably in the visible domain. This aspect is also highlighted by the comparison of PCA and PPCA derived skin swatches depicted in Figure D.9.

We remark that light attenuation is not affected by the melanins and hemoglobins in the IR-B. As a result, in this region of the light spectrum, one can observe fewer variations among the spectral profiles of the different specimens (Figure D.1). This, in turn, leads to the smallest RMSE values obtained in the IR-B.

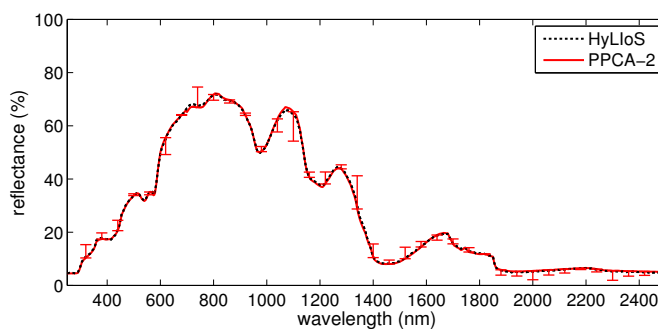


Figure D.6: Modelled (HyLloS) and reconstructed (PPCA using two components) curves for specimen N32. Error bars represent differences between the curves, magnified by a factor of 10. Resulting RMSE values for the UV-Visible, IR-A and IR-B regions are 0.0024, 0.0058 and 0.0024, respectively.

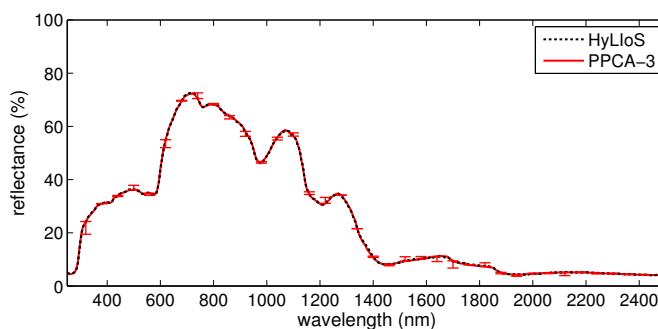


Figure D.7: Modelled (HyLloS) and reconstructed (PPCA using three components) curves for specimen N135. Error bars represent differences between the curves, magnified by a factor of 10. Resulting RMSE values for the UV-Visible, IR-A and IR-B regions are 0.0018, 0.0026 and 0.0013, respectively.

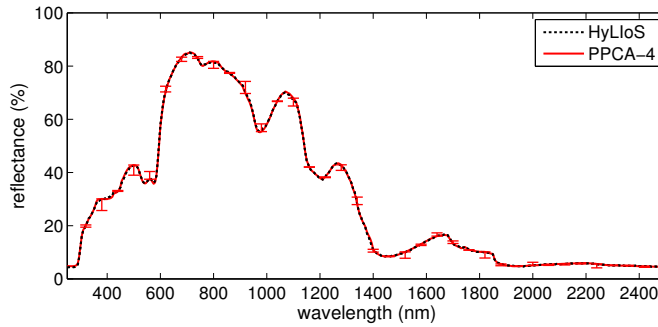


Figure D.8: Modelled (HyLloS) and reconstructed (PPCA using four components) curves for specimen N127. Error bars represent differences between the curves, magnified by a factor of 10. Resulting RMSE values for the UV-Visible, IR-A and IR-B regions were 0.0038, 0.0031 and 0.0010, respectively.



Figure D.9: Skin swatches in the UV (left), visible (centre) and IR (right) ranges obtained for specimen N127 using PCA with four components (top), PPCA with four components (middle) and the original modelled curve (bottom) provided by HyLloS.

D.3 Concluding Remarks

Our findings indicate that substantial storage savings can be obtained using a small number of PCA components in the reconstruction of skin hyperspectral reflectance curves. Moreover, the resulting low reconstruction errors can be further reduced using the same number of components by applying the proposed biophysically-based PPCA approach tailored for human skin hyperspectral reflectance databases.

E Hyperspectral Photography

During the course of our investigations described in this thesis, we employed a camera capable of acquiring images in the UV, visible and NIR spectral domains. In this appendix, we present practical insights pertaining to the use of this equipment. Note that the information provided in this appendix is meant to be used as a starting point for other researchers that intend to employ a similar equipment in their own work. As such, this appendix does not include detailed technical descriptions, but instead offers a general overview about the use and potential applications of the equipment.

E.1 Hardware Description

We employed a modified Canon EOS 700D (Figure E.1 (left)) in our investigations. By default, the camera's imaging sensor is sensitive to UV and NIR light that may contaminate the acquired visible images. To avoid this contamination, the camera comes with a built-in internal hot mirror that only allows visible light to reach the sensor by filtering out UV and NIR light. However, since we want to capture the invisible wavelengths, we had this stock hot mirror removed. We estimate the sensor to be sensitive to light from around 350 nm to 1000 nm .

We then employed transmission filters* (Figure E.1 (right)) to limit the type of light that actually reaches the camera sensor. We employed a Baader U-Filter (2" diameter), Kolari Vision hot mirror (77 mm diameter) and Kolari Vision K720 (77 mm diameter) to allow only UV, visible and NIR light, respectively to be transmitted to the sensor. Since we need to mount these filters onto the EF-S 18-55 IS STM lens that came with the camera and the lens takes 58 mm diameter filters by default, we used step rings to fit the filters onto the lens. With these three filters, we can take four types of photographs: three types corresponding to a spectral domain isolated by

*A transmission filter only allows light of selected wavelengths to pass through. For example, a UV transmission filter would only allow UV light to pass through.



Figure E.1: The equipment used to capture the hyperspectral photographs presented in this thesis. Left: the modified Canon EOS 700D camera. Right: the filters and step rings. The filters, from left to right: Baader U-Filter, Kolari Vision hot mirror and Kolari Vision K720.

each filter and a fourth fullspectral[†] type acquired without the use of any filters.

Note that the Kolari Vision hot mirror and Kolari Vision K720 are able to accept additional accessories that use 77 mm threading. Since this is a standard size for photography, it is relatively straightforward to acquire additional filters (*e.g.*, polarizing filter) to mount onto them. The Baader U-Filter accepts accessories with 48 mm threading. This size is less common and its use is limited to fields like astronomy. As a result, suitable accessories or adapters to more common sizes might be scarce. We would like to remark that additional applications involving the use of the Baader U-Filter may include forensic examinations (*e.g.*, blood detection in crime scenes) [19], analysis of historical documents for conservation purposes [138] and screening of toxic molds for health and safety [206].

E.2 Practical Considerations

When using the camera to take pictures in the invisible spectral domains, we need to be aware of the availability of light sources that emit in these spectral domains. By having sufficient illumination, it is easier to produce higher quality images, use the camera’s autofocus feature and allow the camera to present a clearer picture on its LCD display. This last point is critical since our own eyes cannot perceive UV and NIR light. Therefore, it is necessary to use the

[†]We employ the term “fullspectral” to refer to the combined UV, visible and NIR responses provided by the selected equipment.

camera’s live view feature in conjunction with the LCD display when shooting UV and NIR photographs.

One source of ample UV and NIR light is the sun. As such, it is relatively easy to capture UV and NIR photographs outdoors during a sunny day. On the other hand, in indoor or night settings, UV light is scarce. Therefore, even with sensitive camera settings (*e.g.*, long exposure time), it is difficult to acquire UV photographs in these conditions. NIR light under similar conditions is more plentiful, but it may still require higher sensitivity settings.

E.3 Images

Besides Figure 1.1, we present additional photographs (Figures E.2 to E.8) taken with the selected camera. These photographs depict the distinct appearance for ordinary objects across the different spectral domains. Photographs within each set were taken at the same time to allow for relatively consistent shooting conditions (*e.g.*, lighting and placement). These photographs were all taken outside around noon or early afternoon under good weather conditions to capitalize on the plentiful sunlight available in those environments. UV and NIR photographs were acquired by applying a colour filter to greyscale images produced by the camera sensor. The fullspectral photographs were taken by allowing the camera sensor itself to translate UV and NIR light into visible colours using the manufacture’s proprietary (undisclosed) algorithms.

Although a fullspectral photograph incorporates information from the UV, visible and NIR domains, such photograph is usually perceived as a combination of the individual photographs depicting the visible and NIR responses. For example, the fullspectral photograph of the sunglasses (Figure E.2) blends the opacity and transparency of the lenses from the respective visible and NIR photographs. The omission of noticeable contribution from the UV photograph may be due to less incident UV light or the camera sensor being less sensitive in this spectral domain. The photographed materials that have different appearances across the spectral domains tend to appear more transparent or have higher reflectance in the NIR photographs. On the other hand in the UV photographs, some of these materials appear darker, albeit depicting more noticeable highlights. Examples of this contrast include the sunscreens (Figures E.3 and E.4), Banana Boat bottle (Figure E.3) and Lego pieces (Figure E.7). Note that in Figures E.3 and E.4, SPF stands for sun protection factor, and it refers to the measure of a sunscreen’s ability to protect against erythema, with a higher value providing greater protection [164].

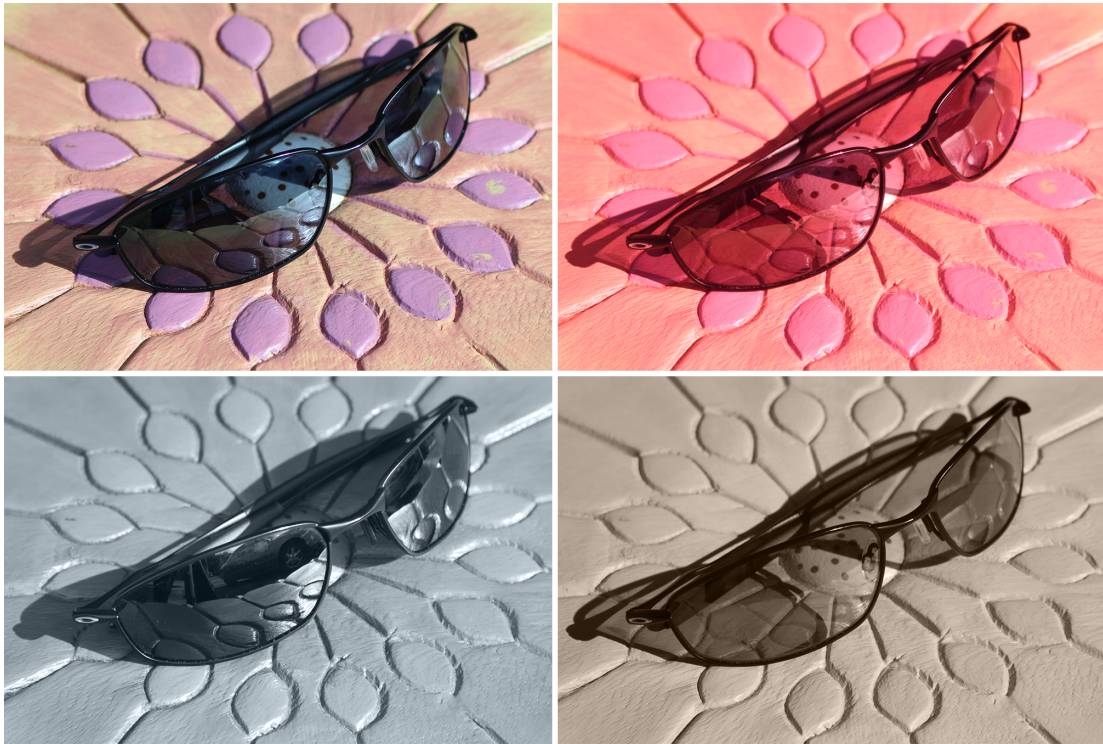


Figure E.2: Photographs of a pair of polarized sunglasses (Oakley Whisker) taken in different spectral domains. Counterclockwise, from top left: visible, UV, NIR and fullspectral. Note the opacity and reflective quality of the lenses in the visible and UV photographs in comparison to the transparency in the NIR photograph.



Figure E.3: Photographs of sunscreens taken in different spectral domains. Counterclockwise, from top left: visible, UV, NIR and fullspectral. The sunscreens, from left to right within each photograph: Banana Boat Sunscreen Oil Spray SPF 15, Coppertone Sunscreen Lotion SPF 30, Hawaiian Tropic Sheer Touch Oil-free Sunscreen SPF 45, Shiseido Hada Senka Mineral Water UV Gel SPF 50 PA+++ and Garnier Ombrelle Complete Lightweight Lotion SPF 60. In the UV photograph, the sunscreens appear very dark, primarily reflecting specular components. In the NIR photograph, the sunscreens still reflect a substantial amount of light since the water present in their composition is characterized by a strong light absorption behaviour only at longer wavelengths beyond the sensitivity of the camera sensor. The Shiseido sunscreen appears to have higher reflectance than the other sunscreens in the UV. This might be due to the Shiseido sunscreen reflecting UV, besides just absorbing, as its strategy to limit skin exposure to UV light. The “dirtiness” of the bottles in the UV domain, which is imperceptible in the other photographs, may be due to the screens’ residue from previous uses. Another interesting feature is the transparency of the Banana Boat bottle in the NIR domain.



Figure E.4: Photographs of a pair of hands taken in different spectral domains. Counterclockwise, from top left: visible, UV, NIR and fullspectral. A sunscreen (Garnier Ombrelle Complete Lightweight Lotion SPF 60) was applied to the right hand. Note the significant darkening effect of the sunscreen's absorptive properties in the UV photograph in contrast to its slightly specular appearance in the other photographs. Again, we remark that in the NIR photograph, the sunscreen is almost imperceptible since the water present in its composition is characterized by a strong light absorption behaviour only at longer wavelengths beyond the sensitivity of the camera sensor.



Figure E.5: Photographs of trees taken in different spectral domains. From top to bottom: visible, UV, NIR and fullspectral. While in the visible domain, the plant leaves' reflectance profile is characterized by higher values in the green region (500 nm to 600 nm) of the light spectrum, in the NIR domain, particularly in the range sampled by the selected equipment (700 nm to 1000 nm), their reflectance profile is characterized by consistently high values, leading to a pale appearance illustrated in the NIR photograph.



Figure E.6: Photographs of the sky taken in different spectral domains. From top to bottom: visible, UV, NIR and fullspectral. Note the light grey sky in the UV and dark sky in the NIR photographs. These appearances may respectively be caused by the plentiful and scarce scattering of light by the atmosphere in the corresponding spectral domains. Note that the position of the clouds has changed over time.

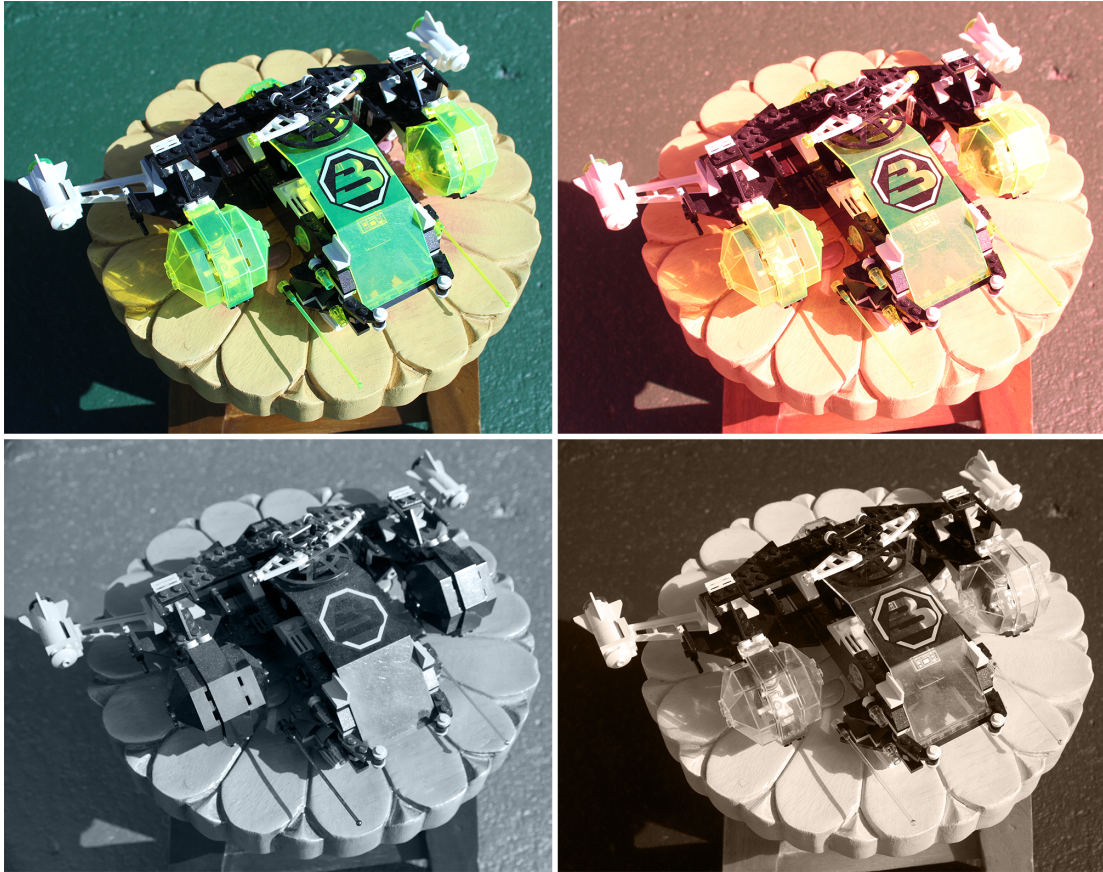


Figure E.7: Photographs of a Lego spaceship taken in different spectral domains. Counterclockwise, from top left: visible, UV, NIR and fullspectral. Note how the yellow-green pieces appear to be opaque in the UV photographs. This may be due to the presence of fluorescent materials in their composition. These materials would absorb UV light to reemit at a different wavelength in the visible domain. The opacity of these pieces in the UV photograph presents a stark contrast to their transparency in the IR photograph. Finally, the presence of dust (*e.g.*, on the model's main canopy) is also more noticeable in the UV photograph.

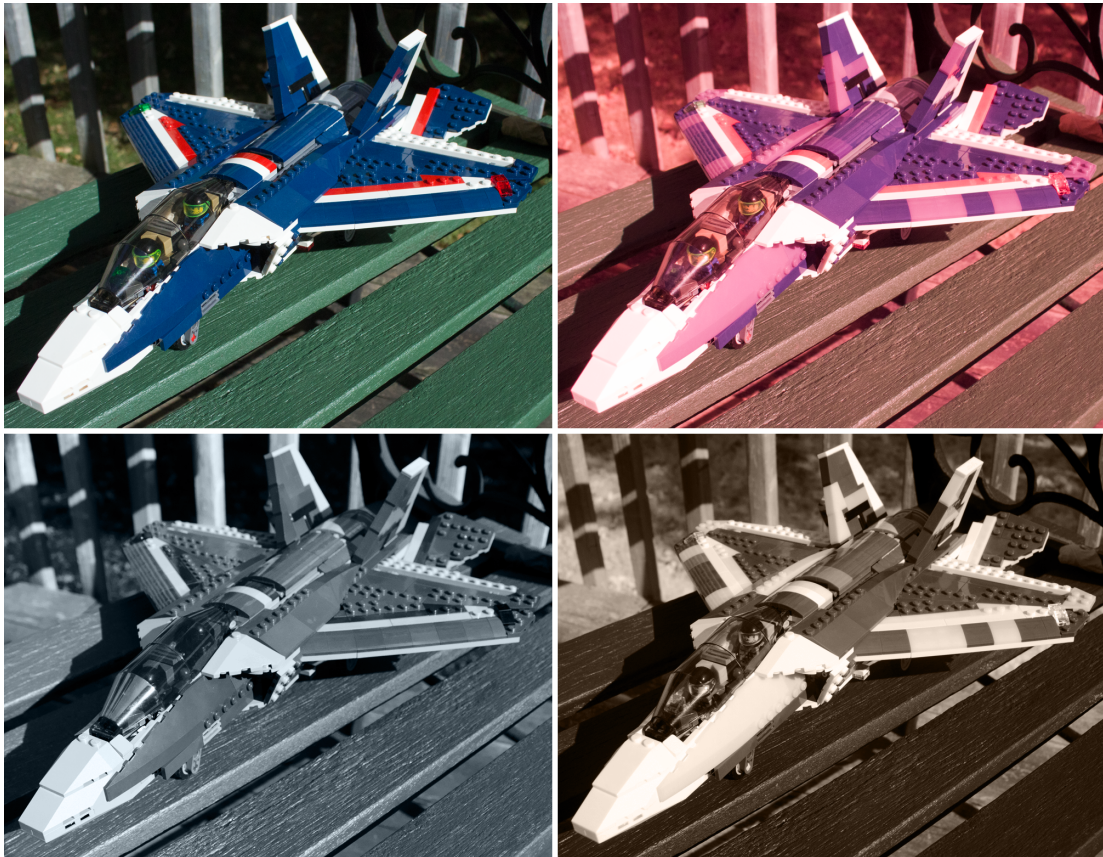


Figure E.8: Photographs of a Lego airplane taken in different spectral domains. Counterclockwise, from top left: visible, UV, NIR and fullspectral. Note the high reflectance of the red and some of the blue elements in the NIR domain. This may be caused by the presence of NIR reflecting dyes. Another detail to notice (also depicted in some of the elements in Figure E.7) is the different appearance of the yellow-green pieces (minifigures' visors) in the different spectral domains.

E.4 Concluding Remarks

In this appendix, we briefly outlined how a modified consumer camera can be used to capture the appearance of objects across the different spectral domains. Employing such a device, one can visualize the striking diversity of material appearances that would be imperceptible to the naked eye. The range of objects worth examining using hyperspectral photography in the future includes, but it is not limited to, blood, stones, crystals, insects and feathers. Among the phenomena that can be investigated using this technology, one can highlight fluorescence and polarization through the use of appropriate filters. In summary, hyperspectral photography can offer valuable insights for future material appearance investigations.

Index

- absorbance, 94
- absorber, 23, 25, 94
- absorptance, 11, 33, 94
- absorption coefficient, 25, 93, 94
 - volumetric, 25
- absorptivity, 95
- action spectrum, 21
- aesthetic applications, 4
- anemia, 6
- appearance, 10, 14
 - capture, 14, 15
 - measurement, 10
- appearance model, 14, 66
 - deterministic, 13
 - environmental factors, 14
 - nondeterministic, 13
 - skin, 13, 14, 45
- attenuation coefficient, 23, 25, 27–29
 - geometric, 27
- attenuator, 23, 25, 26

- beta-carotene, 17, 25, 94
- bidirectional reflectance distribution function,
see BRDF
- bidirectional scattering distribution function,
see BSDF
- bidirectional scattering-surface distribution
function, *see* BSSDF
- bidirectional scattering-surface reflectance
distribution function, *see* BSSRDF

- bidirectional scattering-surface transmittance
distribution function, *see* BSSTDF
- bidirectional transmittance distribution func-
tion, *see* BTDF
- bilirubin, 17, 25, 94
- BioSpec, 45
- blood, 17, 25, 43, 52–54, 57
 - variation, 14
- BRDF, 12, 22, 49–51
- BSDF, 12
- BSSDF, 12
- BSSRDF, 12, 22, 31, 40, 49, 51
- BSSTDF, 12
- BTDF, 12

- cancer, 6
- carboxyhemoglobin, 17, 25, 94
- CIE, 3, 61
- colorimetry, 14
- Commission Internationale de l'Éclairage, *see*
CIE
- comparison, 13, 60
 - qualitative, 5, 7, 45, 47, 48, 50–57, 61–64,
109, 111
 - quantitative, 5, 7, 44, 45, 47–50, 53, 55–57,
61, 63, 100–102, 108–111
- computer graphics, 2, 3, 6, 10, 14, 15, 19, 68, 69
- computer science, 1
- corneocyte, 93
- cosine distribution, 28

D65 illuminant, 45, 61, 107
 data
 characterization, 42–44, 60, 61
 measured, 5, 7, 42, 45, 47–50, 63, 94, 97
 simulated, 5, 47
 database, 6
 deoxyhemoglobin, 17, 25, 43, 94, 105
 dermis, 16, 17
 detour effect, 18, 70, 103
 differential pathlength, 103
 diffuse scattering, 18, 30, 49
 diffusion theory, 13
 diffusion theory approximation, 13
 discrete-ordinate approximation, 13
 DNA, 14, 17, 52, 54, 94, 95

 education, 1
 environment, 1
 epidermal, 35
 epidermal cell migration, 35
 epidermis, 16, 17, 20, 28, 31, 47, 99
 erythema, 19
 action spectrum, 21
 ethereal, 3, 49
 eumelanin, 103, 105
 experiment, 15
 exponential distribution, 28, 29
 exposure dose, 21, 60, 61
 schedule, 61, 63

 factor of intensification, 103
 fibril, 18
 fidelity, 13
 filter, 112
 fluorescence, 71
 freckles, 2, 4, 50
 Fresnel
 equations, 16
 test, 23, 28, 30
 fullspectral, 113, 115–121
 Gladstone and Dale law, 93
 glossiness, 10
 graphics hardware, 13, 72

 health care, 1
 health science, 4
 Hill function, 36, 39
 hot mirror, 112
 hue, 10
 hydration, 4
 HyLIOs, 5, 22, 23, 42, 69, 93, 99, 106
 hyperplasia, 5, 15, 20, 32, 37
 hyperspectral, 3–5, 16, 22, 47, 69, 105, 108–111
 see also fullspectral
 hypodermis, 18, 30

 infrared, *see* IR
 input sensitivity analysis, 42, 52
 interdisciplinary, 2, 6, 68, 70
 inversion procedures, 6, 98, 99, 103
 IR, 3, 5, 10, 13, 16, 17, 23, 42, 48–54, 57, 58, 98,
 100, 105, 107, 109, 111
 IR-A, 105, 108–111
 IR-B, 105, 108–111

 keratin, 17, 52, 54, 94, 95
 Kubelka-Munk theory, 13, 14

 $L^*a^*b^*$, 61, 63
 life science, 4
 light
 absorption, 5, 11, 13, 16–18, 22, 25, 70
 attenuation, 23, 25, 28
 hyperspectral, *see* hyperspectral
 infrared, *see* IR
 near-infrared, *see* NIR

propagation, 13, 23
 ray, 23, 27
 reflection, 11, 22, 30
 scattering, 5, 11, 16, 17, 25, 29, 47, 49, 50
 diffuse, *see* diffuse scattering
 Rayleigh, *see* Rayleigh scattering
 transmission, 11, 16, 22, 23
 ultraviolet, *see* UV
 visible, *see* visible
 lightness, 10
 lipid, 48, 54
 lipids, 14, 17, 25, 52, 54, 94, 105
 lustre, 10

 mean sensitivity index, *see* MSI
 MED, 20, 62
 melanin, 13, 17, 19, 20, 25, 35, 48, 49, 51–54, 57, 102, 103
 colloidal, 17, 19, 25, 40, 43, 102
 content, 13, 19, 31, 40, 96–100, 103
 degradation, 15, 35
 distribution, 13, 15, 20, 31, 40, 98
 see also melanosome distribution
 dust, *see* melanin colloidal
 eumelanin, 17, 25, 31, 43, 94
 particle nature, 98
 pheomelanin, 17, 25, 31, 43, 94
 melanocyte, 17, 20, 35
 melanogenesis, 20, 31–33, 35
 action spectrum, 21, 33
 melanosome, 5, 17, 19, 20, 25–28, 40, 42, 43, 45, 70, 99, 102, 103
 complex, 17, 26, 28
 degradation, 42
 distribution, 13, 45
 see also melanin distribution
 particle nature, 13
 methemoglobin, 17, 25, 94

 Mie theory, 5
 minimum erythema dose, *see* MED
 minimum melanogenesis dose, *see* MMD
 MMD, 20, 61, 62
 moles, 4, 50
 MSI, 52, 54

 near-infrared, *see* NIR
 NIR, 100–102, 105, 112, 115–121

 optical energy density, 21
 organelle, 17
 oxyhemoglobin, 17, 25, 43, 94, 105

 papillary dermis, 16, 18, 22, 25, 43
 parallel processing, 13
 PCA, 8, 72, 104, 105, 107–109
 PDF, 27, 28, 30
 pheomelanin, 103, 105
 photoaddition, 60
 photobiology, 6, 19, 21, 41, 69, 103, 104
 photograph, 3, 15, 112, 115–121
 photoprotection, 4, 71, 103
 piecewise PCA, *see* PPCA
 pigmentation, 15, 52
 amelanotic, 106, 109–111
 constitutive, 20, 35, 60–62, 102
 facultative, 20, 31, 35, 62, 71, 101
 increase, 15
 irregularities, 4, 50, 51
 regulate, 6
 pigmented
 darkly, 17, 18, 26, 42, 50, 52, 100–102
 lightly, 17, 18, 26, 42, 51–53, 55–58, 100–102
 moderately, 18, 26, 27, 50, 52, 58
 PPCA, 105, 110, 111
 prediction, 4–7, 13, 42
 principal component analysis, *see* PCA

probability distribution function, *see* PDF
 radiant exposure, 21
 random walk, 23, 24, 26
 ratio of intensification, 103
 ray optics, 23
 Rayleigh scattering, 17, 29, 30
 recursion, *see* recursion
 reflectance, 6, 11, 13, 22, 31, 40, 44, 45, 47–49, 55–57, 61, 69, 104
 reflection, 23
 refractive index, 16, 18, 22, 28, 29, 93
 remote sensing, 14
 reticular dermis, 16, 22, 43
 RMSE, 100, 107, 108
 saturation, 10
 SED, 21
 sieve effect, 18, 70, 103
 signal substance, 34
 simulation, 5–7, 14
 first principles, 13
 Monte Carlo, 13
 physiologically-based, 15
 singular value decomposition, *see* SVD
 skin, 2
 aging, 14
 appearance, 14, 40, 53
 appearance model,
 see appearance model skin
 cell, 17, 30
 cells, 38
 dermis, 49
 fibre, 17, 26, 29
 phototype, *see* SPT
 thickness, 16, 17, 20, 21, 37, 39, 40, 43, 93, 96, 97
 ultraviolet sensitivity, 15
 spectral, 2
 spheroid, 5, 17, 26–28
 SPT, 20, 62
 standard erythema dose, *see* SED
 stratum basale, 16, 17, 22, 35, 40, 43, 97, 99
 stratum corneum, 16, 17, 22, 30, 43, 93
 stratum granulosum, 16, 22, 35, 42, 43, 97, 99
 stratum lucidum, 16
 stratum spinosum, 16, 22, 35, 42, 43, 97, 99
 subsurface scattering, 12, 22, 48–51
 sulfhemoglobin, 17, 25, 94
 sun protection factor, 114
 sunburn, 19
 sunscreen, 58, 65, 66, 72, 98, 116, 117
 surface roughness, 17, 30, 43
 SVD, 105
 tanning, 2, 5, 15, 19, 20, 31, 61–63, 65–67
 framework, 5, 31, 32, 42, 60, 69
 tissue optics, 14
 translucency, 10, 12
 transmittance, 11, 13
 Trowbridge-Reitz function, 30
 ultraviolet, *see* UV
 radiation, *see* UVR
 urocanic acid, 14, 17, 94, 95
 UV, 3–5, 10, 13, 16, 17, 19, 23, 42, 47, 49–54, 56, 58, 70, 98, 101, 102, 105, 107–112, 115–121
 UVA, 71
 UVB, 71
 UVR, 2, 5, 6, 32, 60–62, 69, 71
 exposure, 5, 6, 15, 19, 20, 31, 59, 62, 63, 65, 66, 69, 71
 sensitivity, 5
 threshold, 33
 visible, 2–5, 8, 13, 14, 16, 17, 19, 23, 42, 45,

47, 48, 51–53, 55, 58, 98, 100–102, 105,
108–112, 115–121
visualization, 5, 6
 physiologically-based, 15
vitiligo, 106

water, 14, 17, 25, 48, 49, 51–54, 58, 93, 94, 98,
105
wave optics, 23, 27, 28